NOTE TO USERS

STATIC AND DYNAMIC CRITICAL PHENOMENA IN ULTRATHIN FILMS OF IRON ON W(110)

By

MICHAEL J. DUNLAVY, B.Sc. M.Sc.

A Thesis

Submitted to the School of Graduate Studies

in Partial Fulfillment of the Requirements

for the Degree of

Doctor of Philosophy

McMaster University

CRITICAL PHENOMENA IN ULTRATHIN MAGNETIC FILMS

DOCTOR OF PHILOSOPHY (2003) McMaster University
(Physics) Hamilton, Ontario

TITLE: Static and Dynamic Critical Phenomena in Ultrathin Films of Iron on W(110)

AUTHOR: Michael J. Dunlavy, B.Sc.(St. Francis Xavier University) , M.Sc.(McMaster University)

SUPERVISOR: Dr. D. Venus

NUMBER OF PAGES: xv, 144

Abstract

The critical properties of Fe/W(110) ultrathin films with thickness between 1.5 and 2.0ML have been studied using magnetic ac-susceptibility χ_m. Using a careful statistical fitting routine that allows simultaneous extraction of the critical exponent γ and the transition temperature T_c, the Fe/W(110) films were found to belong to the 2d Ising universality class. Measuring the 2d Ising γ value of $\frac{7}{4}$ from the data appears to be dependent on how close to T_c the data allows fitting. This in turn is dependent upon film thickness, likely through changes in film uniformity. For measurements of the susceptibility that show power-law scaling below a reduced temperature value of 4.75×10^{-3}, the average value of $\gamma = 1.75\pm.02$. Further analysis of the complex susceptibility allows the extraction of the critical slowing down exponent z. It has been found that bilayer films that exhibit a static critical exponent γ near 1.75 show a value of $z = 2.09\pm.06$ (95% confidence). This finding represents the first experimental measurement of the critical slowing down exponent which supports the current theoretically predicted value for a 2d Ising system. Further analysis also allows insight into various saturation processes that affect the magnetic ac-susceptibility near T_c and the effect that oxygen doping of the surface has on the saturation.

Acknowledgements

My most sincere thanks:

- To David Venus for the years of supervision and support,
- To Marek Kiela for his technical expertise and his friendship,
- To John Preston and Graeme Luke, the supervisory committee I didn't bother enough in the course of this research,
- To Peter Kruse and his group for the STM pictures
- To Martin Grant and Malcolm Collins for the useful conversations
- To my comrads in the lab, especially Steve Arnold for teaching me everything I know about surface science experiments,
- To Glen P., (Small) Mike L., Peter B., Lorna R., and Paul D. for the visits,
- To all my friends, past and present, amongst the graduate students and the faculty at McMaster,
- To my family of course,
- To Mike, Doug, Dave, Barry, Yogi, Naeem, Jamie, and Regis,
- And, of course, to Roby Anne Elizabeth Austin. This thesis is dedicated to her.

Contents

List of Figures

List of Tables

Chapter 1

Introduction

Phase transitions are a comparatively old subject in the world of physics. Ever since the discovery that ice, water, and steam are all different phases of H_2O, scientists have been working to discover the physics behind the transformation of materials from one phase to another.

The phase of a material is defined by the value of its *order parameter*. The order parameter can be any intrinsic measure of a material property that defines the different phases. For example, in the case of water, the relevant order parameter is the local density. The value for the order parameter will change for a different value of an extrinsic material property, such as temperature and pressure. When a block of ice is placed in contact with an environment of temperature higher than 273.15K, it will undergo a phase transition from its solid phase to the liquid water phase. If the temperature rises one hundred degrees higher, the water will turn into its gaseous form, namely steam. This all assumes that the pressure stays constant and at a value of one atmosphere for the numbers quoted above to be correct. Water can also turn to steam or ice if the ambient pressure environment decreases or increases respectively. At the heart of any phase transition mechanism is the notion that the value of the order parameter changes with external coercion.

Phase transitions generally fall into two categories: *discontinuous* (also called first order) and *continuous* (second order). The discontinuous transition has associated with it what is referred to as the *latent heat*, which is the amount of energy the system acquires when it orders and then releases when it disorders (or sometimes vice versa). The continuous transition occurs with no latent heat. The reason for this and the reason behind there being two types of transitions is reflected in the form of the system's *free energy*. The free energy is defined as the energy of the system that is available to do work or, more exactly, the difference between the total internal energy and the entropic energy. The reason for the nonintuitive first and second order nomenclature is from considerations of what derivative of the free energy is discontinuous at the transition.

This thesis is a study of phase transitions in magnetic thin films. For these materials and most magnetic systems in general, the magnetic properties are due to the cooperative nature of the individual *magnetic moments*, which are the local sources of magnetic fields that arise from the angular momentum of subatomic particles. A ferromagnet is a material where all of the magnetic moments in the material spontaneously order along a certain direction (called the *easy axis*). Ferromagnets will typically undergo a continuous phase transition as a function of temperature to become paramagnets. The paramagnet has all of its moments pointing in random directions. The net magnetic properties of the common iron bar magnet is entirely due to this spontaneous ordering. But, if the bar magnet was heated up past 1043K, all the paper clips and thumb-tacks attached to the end would fall due to the material undergoing a phase transition as a function of temperature to its paramagnetic form. The temperature of 1043K is where the phase transition occurs in iron. In ferromagnets, this temperature is called the *Curie temperature*, usually abbreviated

as T_c.

In a ferromagnet, the order parameter of interest is the net or average magnetization m. For $T>T_c$, where all the moments are randomly aligned in the paramagnetic state, the average value of m is zero. In a ferromagnet, the ordering of the moments causes m to have a non-zero value. The ordering is very sensitive to the amount of thermal energy in the material. Once the thermal energy of the system increases to the point where it is on par with the energy that causes the alignment of the moments (called the *exchange energy*), the moments disorder and the temperature where that happens is called the Curie temperature.

There is a lot of interest in the mechanism of how the disordering and hence the phase transition occurs. It has been found that the magnetization of a ferromagnet behaves as a power law as T_c is approached from below in temperature ($T \rightarrow T_c^-$). The exponent of the power law is called the *critical exponent* of the order parameter and it is symbolised by the Greek letter β. Figure 1.1 shows a modeled power-law for the magnetization as a function of temperature.

The value of β can tell a great deal about the phase transition. The concept of *scaling* has shown that a phase transition is not sensitive to the microscopic details of a system's Hamiltonian but to the long range symmetry of the material as well as its dimensionality and the degrees of freedom of its order parameter. These concepts lead to the conclusion that as long as a few macroscopic criteria are met, then two seemingly completely different phase transitions will have identical critical exponents! A group of materials that have the same set of critical exponents are said to belong to the same *universality* class.

As can be inferred by the previous paragraph, there are more critical exponents that just β. The other exponents describe how other properties of the material

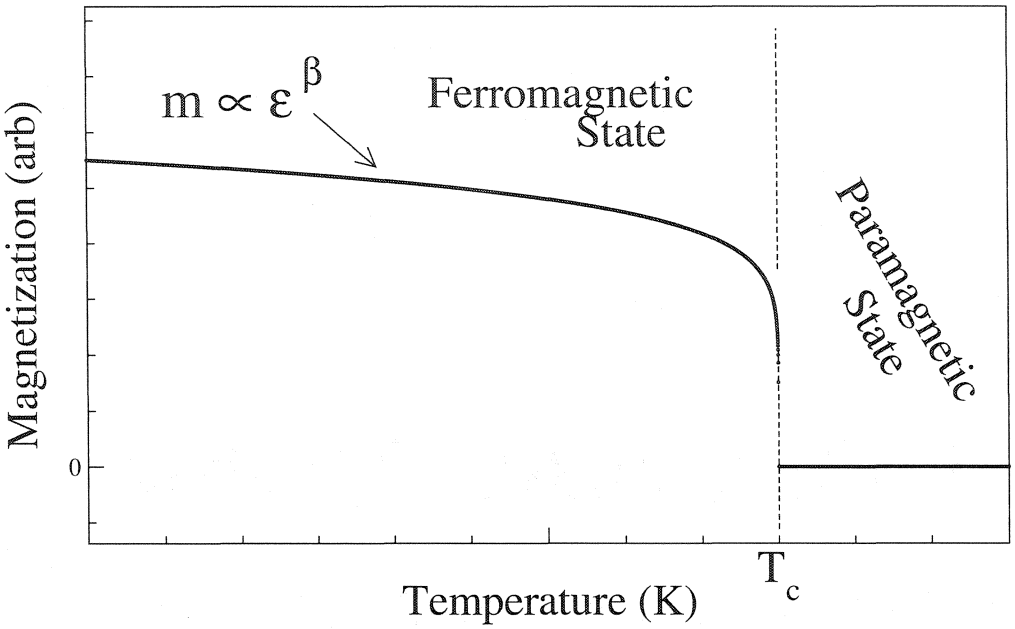

Figure 1.1: Graph showing magnetization as a function of temperature. In this idealisation of data, T_c is marked where m goes to zero and β is $\frac{1}{8}$. ϵ is the reduced temperature (1 - T/T_c).

behave at the phase transition. These include (but are not limited to):

- Specific Heat

The specific heat (usually symbolised as C) is a measure of the amount of energy required to raise the temperature of the system. The exponent of the power law that describes the temperature dependence is α.

- Correlation Length

If a moment spontaneously flips away from its equilibrium position, this sets up a fluctuation the effects of which will be felt by moments out to a certain mean distance. The average value for this distance is the correlation length and is denoted by the Greek letter ξ. At T_c, the thermal energy is equal to the energy that orders the moments and therefore only a small amount of additional energy is required to create a fluctuation and once created, the effects of it will carry farther than it would

at lower temperatures. ξ will theoretically diverge to infinity at T_c via a power-law with an exponent ν.

- Susceptibility

The susceptibility is a measure of how sensitive the order parameter is to an external field. In magnetic systems, this is usually the susceptibility of the magnetization to an externally applied magnetic field, written formally as the derivative $\frac{\partial m}{\partial h}$, where m is the average net magnetic moment and h is the externally applied magnetic field. The susceptibility is denoted by the Greek letter χ. The susceptibility, like the correlation length, diverges at T_c according to a power-law governed by the critical exponent γ.

- Relaxation Time

The relaxation time τ is a measure of the average time it takes for fluctuations of the order parameter to dampen out. For small deviations from equilibrium, the relaxation of the magnetization in a ferromagnet will behave as an exponential, with an argument of -t/τ. The value of τ will diverge with the correlation length and the exponent of its divergence as a function of temperature is the product of ν and z, where z is called the *critical slowing down* exponent.

These last two quantities, χ and τ, and their exponents are the major subjects of this thesis.

1.1 Experimental Studies of Phase Transitions in Ultrathin Films

Experimental studies on phase transitions in ultrathin magnetic films (generally defines as being between 1-10 atoms thick) face problems and advantages that make them different from the usual studies done on bulk magnetic materials. While the

nature of the sample make it an excellent real world manifestation of two-dimensional theories, the same extreme sample dimensions also rules out the use of such standard techniques as x-ray and neutron diffraction.

Almost all studies in the literature tend to focus on measuring the static critical exponents β and γ, the former being more popular than the latter. Earliest studies of β used various electron-probe techniques such as ESP (electron spin polarimetry) or SPLEED (spin-polarised low energy electron diffraction). While other techniques such as FMR (ferromagnetic resonance) and TOM (torsion oscillation magnetometry) have been successful, most studies make use of SMOKE (surface magneto-optic Kerr effect). See section 3.6 for more details about SMOKE.

The first major body of work on magnetic monolayer phase transitions began to appear in the late 1980s, early 1990s. One of the first papers to report a value for β was by Rau *et al*[3], who made measurements on V(100)/Ag(100) monolayers using ESP. They found a β value of 0.128 ± 0.01, very close to the 2d Ising (meaning a two-dimensional system with spins that can have one of two opposite orientations) value of 0.125. This was closely followed by several other papers including measurements on Ni/Cu(111) using SMOKE[4], Fe/Au(100) using SPLEED[5], Ni/Cu(111) again using SMOKE (this paper found a higher value for β than the previous paper), Co/Cu(100) using SMOKE[6], Ni(111)/W(110) using FMR[7] [the Ni(111)/W(110) system seems to be unmeasurable by standard SMOKE techniques as judged by repeated attempts to make such measurements by the author], Fe/Ag(111) using SMOKE[8], and Fe/W(110) by a combination of techniques[9]. This last paper is discussed in more detail in chapter 4.

There are two interesting studies, one on Ni(111)/W(110)[10] and one on Ni/Cu(110)[11], that find strong evidence for dimensional crossover from two to three

dimensional behaviour as a function of thickness. The Ni/W(110) system was found to go from behaving as a 2d Ising system for less than 4ML to a 3d exponent in the range of 0.35 for systems thicker than 8ML. The intervening thicknesses showed a steadily increasing value of β between the two limiting boundaries. The Ni/Cu(110) system seems to transform as a function of thickness at 7ML from three dimensional Heisenberg to a two-dimensional XY system.

A paper by Kohlhepp *et al*[12] made arguments that any measurement of β in ultrathin magnets should be made using the saturated magnetisation in the presence of a magnetic field instead of the standard remnant magnetisation. They noted the marked difference between the two quantities on a perpendicularly magnetised film of Co/Cu(111). Their treatment however ignores the fundamental problems of domains in films with perpendicular moments. The dipole energy in such a system leads to a multi-domain ground state that, especially near T_c, gives zero net magnetisation in zero field.

One of the first measurements of γ from an ultrathin film was measured on Gd(1000)/W(110)[13] using electron spin resonance. A 2d Ising exponent is reported but the important question of the determination of T_c is raised. It could be argued that finding the transition temperature in the magnetisation data is a simpler task than determining it from the susceptibility. For T_c, they used the temperature at which there is an inflection point in the high temperature tail, citing agreement with bulk phenomenon. They also report they allowed T_c to vary in a least-square fit and the resulting value of T_c agreed with the inflection point temperature to within a degree. However, they do not state which they used for T_c, the fit value or the inflection temperature. It is certain the changing T_c within the range of a degree would give a much different result for the value of γ.

Other γ papers report results for Gd(1000)/W(110) using ac-susceptibility[14], monolayer Fe/W(110) using SPLEED[15], Fe(100)/W(100) using electron spin diffraction and Mossbauer spectroscopy[16] and Fe/W(110) using SMOKE[17]. This last paper was written mainly to display a new technique that improves the signal-to-noise in SMOKE measurements, a technique used for all the susceptibility measurements in this thesis. The analysis of the critical exponent therein contains numerous faults, including the means by which the weighted least-square fits were performed.

Besides the determination of T_c, the analysis of the susceptibility to find γ is further complicated by the demagnetisation factor (see section 2.3.2). This subtle yet extremely important point is treated very inconsistently in the literature, usually either ignored completely[17] or greatly overestimated[18] for films that are magnetised within the plane. For perpendicular films, the demagnetisation factor prevents the measured magnetic susceptibility from diverging at all.

—

This thesis will focus on measurements of the critical exponent γ and the product exponent $z\nu$ in two-dimensional magnetic systems, namely ultrathin films of iron grown atop a tungsten (110) crystal. To the knowledge of the author, there has been no experimental study of critical slowing down in ultrathin ferromagnets (there has been some work done on two-dimensional bulk samples. These will be discussed in sec. 4.2). A method of fitting susceptibility data will be presented that will allow the extraction of both the value for γ and T_c. The results will show that the critical exponent γ depends on how close to T_c that data can be fit to a power-law and that this is in turn is related to film thickness. The complete complex susceptibility will then be analysed for critical slowing down and results will be presented that experimentally confirm the current theoretical value for $z\nu$ for two dimensional magnetic

systems.

Following this introduction, chapter 2 will go into some detail on the theory behind many of the subjects that have been briefly mentioned here. Chapter 3 will outline the workings of the experimental methods used to make the careful measurements, as well as a brief description of the growth and characterisation of ultrathin films. Chapter 4 will present the major findings of this research. Included in their entirety will be two papers which have recently been submitted to APS journals; the first (on measurement of the exponent γ) to Physical Review B and the second (on critical slowing down and saturation effects in critical measurements of χ) to Physical Review Letters. Following the unexpurgated text of the papers will be extra material filling in some details of the material in the papers as well as sections on the effect that doping the tungsten surface with oxygen has on the structural and magnetic properties of the iron films. Chapter 5 will present the major conclusions of the work.

Chapter 2

Theory

2.1 Introduction

This chapter will outline the theoretical background to the experimental results of this thesis. The sections will roughly follow a two part structure. In the first part, the basic phenomenon of ferromagnetism will be presented along with various other topics of importance such as magnetic anisotropy and demagnetisation. Following this will be a treatment of the statistical mechanics of phase transitions, with accompanying information on topics such as scaling and universality.

2.2 Magnetism

Classically, magnetic fields arise from the movement of electric charge. The equations of Maxwell accurately describe the creation of magnetic and electric fields due to electric currents (and vice-versa) in a classical context, even though most of the concepts they describe are relativistic in detail.

The magnetic field created by a coil of conducting material carrying an electric current I is (in cylindrical coordinates):

$$H(r,\theta) = \frac{\mu_o I A(2cos(\theta)\hat{r} - sin(\theta)\hat{\theta})}{4\pi r^3} \tag{2.1}$$

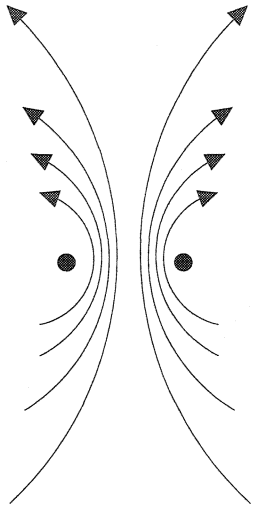

Figure 2.1: Dipole Field Lines. Solid dots represent cross-section of current-carrying wire.

where H is the magnetic field, A is the area of the loop, and the center of the loop is the origin of the coordinate system defined by $\hat{r}$ and $\hat{\theta}$. This is the classical magnetic dipole field and is illustrated in figure 2.1.

Microscopically, for a single electron, the magnetic moment is created by the angular momentum of the particle. According to quantum mechanics, the angular momentum of a particle is described by the orbital angular momentum $\mathbf{L}$ and its quantum number, $\mathbf{l}$, and the spin angular momentum $\mathbf{S}$ and its quantum number, $\mathbf{s}$. The total angular momentum is $\mathbf{J}$=$\mathbf{L}$+$\mathbf{S}$. The total moment of a single particle with angular momentum $\mathbf{J}$ is:

$$\mathbf{m} = -g\frac{\mu_o \hbar e \mathbf{j}}{2m_e} \tag{2.2}$$

where μ_o is the permeability of free space ($4\pi \times 10^{-7}\frac{H}{m}$), $\hbar$ is Planck's constant ($6.63\times10^{-34}Js$), m_e is the mass of the electron (9.1×10^{-31}kg), e is the electron charge ($1.60\times10^{-19}C$), and g is the relativistic gyromagnetic ratio. This leads to the defini-

tion of the Bohr magneton:

$$\mu_B = \frac{\mu_o e\hbar}{2m_e} \tag{2.3}$$

This of course is a constant and thus magnetic moments are often quantified in units of μ_B.

The magnetic moment is a vector whose orientation is more important in most studies of magnetic phase transitions that its size. The alignment of moments in a material defines how magnetic materials are classed. The mechanism behind the macroscopic alignment of moments will be discussed in detail in the next section. The following list sketches the important types of magnetic behaviour (see figure 2.2 for schemata of the principle three).

Ferromagnetism

In a ferromagnet, the moments all align in the same crystallographic direction for temperatures lower than a critical temperature (called the Curie temperature, T_c). The mutual alignment is due to the very short-ranged exchange interaction. This alignment is a cooperative phenomenon which decreases the overall system energy. The direction of spontaneous alignment is dependent on the *magnetic anisotropy* but the moments can also be aligned along the direction of an applied magnetic field.

Antiferromagnetism

Antiferromagnets are systems where the total system energy is decreased when neighbouring moments are aligned in opposite directions below a certain critical temperature (called the Neel temperature, T_N). In a perfectly ordered antiferromagnet, the total average moment will be zero as all contributions to the total moment will be canceled by their neighbour and as such, is not sensitive to small applied magnetic fields. Like ferromagnets, the source of this ordering is the exchange interaction. Antifer-

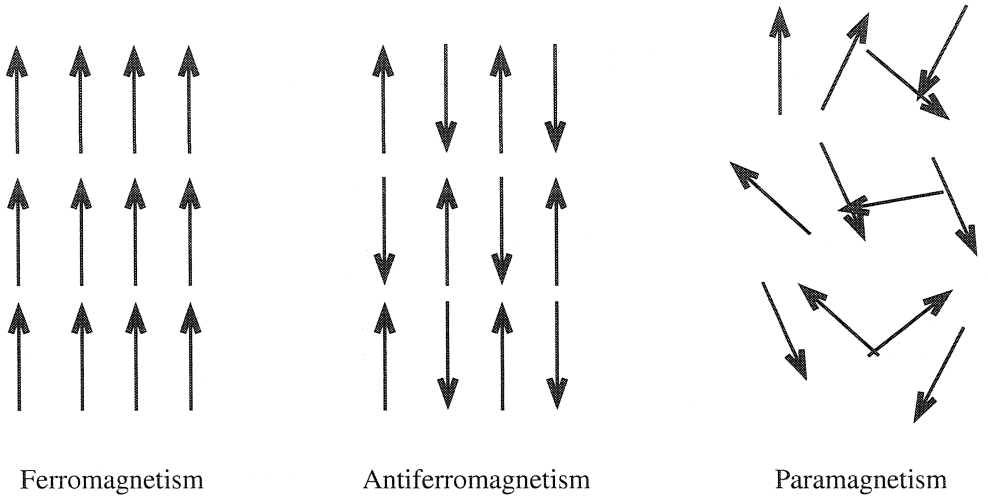

Figure 2.2: Schematic diagrams of three classes of magnetic behaviour.

romagnets have formed the basis of interesting research on triangular lattices where the system ground state is degenerate due to conflicting interactions from having an uneven number of near-neighbours.

Paramagnetism

Paramagnets are systems where the moments are arranged in random directions. This is due to either an insignificant exchange interaction or to the fact that the system is above a critical temperature where the thermal kinetic energy is larger than the energy saved by ordering. Paramagnets are susceptible to applied fields and will have a net moment that varies linearly (to a point) with the size of the field.

Diamagnetism

Diamagnets are unordered in the undisturbed state but will align in such a way as to repel external magnetic fields from the bulk of the material. The dipole fields of the moments act against the applied field. The Meissner effect in superconductors is a good example of diamagnetic behaviour.

2.2.1 The Exchange Interaction

The exchange interaction is the cause behind almost all magnetic phenomenon in metals. The effect of exchange is very localised, usually only affecting near neighbour atoms in the lattice. The origin is based in the Coulomb interaction between two like-charged particles and the quantum mechanical need for systems of fermions to have wavefunctions that are anti-symmetric under particle exchange.

As a simple illustrative example, let us look at the case of a hydrogen molecule [H_2] consisting of two electrons orbiting around two positively charged nuclei. The allowed state of a two particle system is the product of the individual one particle states. The quantum state of the electrons has a spatial and a spin component. There are four possible configurations for the spin wavefunction that give rise to two possible values for the total spin value **s**. These eigenfunctions are as follows:

$$|\uparrow\uparrow> \tag{2.4}$$

$$|\downarrow\downarrow> \tag{2.5}$$

$$\frac{1}{\sqrt{2}}(|\uparrow\downarrow> + |\downarrow\uparrow>) \tag{2.6}$$

$$\frac{1}{\sqrt{2}}(|\uparrow\downarrow> - |\downarrow\uparrow>) \tag{2.7}$$

The first three of these wavefunctions are the triplet states. They are symmetric functions under particle exchange ($s_1 s_2 \leftrightarrow s_2 s_1$) and have $\mathbf{s} = 1$. The fourth is the singlet state. It is antisymmetric and has $\mathbf{s} = 0$. The total wavefunction must also contain a spatial part, which has two basic configurations that are of the form:

$$\psi_{sym} = \phi_1(r_1)\phi_2(r_2) + \phi_1(r_2)\phi_2(r_1) \tag{2.8}$$

and

$$\psi_{asym} = \phi_1(r_1)\phi_2(r_2) - \phi_1(r_2)\phi_2(r_1) \tag{2.9}$$

where $\phi_i(r_j)$ is the spatial wavefunction of particle i at position r_j. The first of these is a symmetric function under particle exchange while the second function is antisymmetric. For the complete wavefunction with both the spatial and spin configurations represented, it is seen that to maintain proper symmetry conditions that the symmetric spatial state must be joined with the antisymmetric spin function (singlet state) and vice-versa. The difference in energy between these two states is:

$$E_s - E_t = \frac{<\psi_s|\mathcal{H}|\psi_s>}{<\psi_s|\psi_s>} - \frac{<\psi_t|\mathcal{H}|\psi_t>}{<\psi_t|\psi_t>} \tag{2.10}$$

where ψ_s and ψ_t are the total wavefunctions that include the singlet and triplet states respectively. The Hamiltonian $\mathcal{H}$ takes a form that includes the Coulomb potential between the two particles and the two nuclei as follows (in the large separation approximation):

$$\mathcal{H} = -\frac{\hbar^2}{2m}(\nabla_1^2 + \nabla_2^2) + V_c(r_1, r_2) + V_c(R_1, R_2) - V_c(r_1, R_1) - V_c(r_2, R_2) \tag{2.11}$$

where $V_c(a, b) = \frac{e^2}{|a-b|}$ is the Coulomb potential, r is the electron position, and R is the nucleus' position. The large separation approximation removes Coulomb terms between the electron of one atom and the nucleus of the other. After sufficient algebra, eq.(2.10) becomes:

$$E_s - E_t = <\phi_1(r_1)\phi_2(r_2)|\frac{e^2}{r_1 - r_2}|\phi_2(r_1)\phi_1(r_2)> \tag{2.12}$$

which is the electrostatic interaction between the two single particle electronic states. It is this interaction that helps to determine the spin state of the system. Since like-aligned spins occur in the triplet state, they lower the Coulomb potential energy of the system and are therefore preferred.

This is the simplest example to show the origin of the exchange interaction. Most real systems are much more complicated as they involve many electron systems

where Slater determinants and other many-body techniques must be employed. Many systems will deal with itinerant electron bands as opposed to localised electrons on well-defined sites. However, the basic electrostatic nature of the interaction remains the same.

In summary, for the total two-electron wavefunction, there is a difference in the total energy of a system of spin 1/2 particles depending on whether the system is in the singlet or the triplet state. This is due the fact that the system with the symmetric spin function must have an antisymmetric spatial function and vice versa. The different spatial functions will give rise to changes in the spatially dependent Coulomb energy and as such will act to prefer the spin state of the system.

2.2.2 Itinerant and Local Magnetic Models

In many real materials and especially in metals, the magnetic moments are not always localised at atomic sites in the system. The moments that are classically associated with the electrons are in the valence band of the material. For the traditional 3d ferromagnets (Fe, Ni, and Co), the magnetic system is referred to as *itinerant*. This means that the magnetic interaction isn't between the localised electrons but is between the electrons in the delocalised band states. This band theory of ferromagnetism was first proposed by Stoner[19] and contains much of the physics of basic magnetism.

For 3d transition metals, there exists the possibility of having electron band energies very near the Fermi surface. The 3d bands undergo some amount of overlap and there is also sharing of electrons with the 4s band. The presence of the crystal field (an electric field that exists due to the charged particles in the lattice) gives rise to a "quenching" of the orbital angular momentum of the bands, so $\mathbf{L}$ is often ignored and only $\mathbf{S}$ is used. Figure 2.3 shows the effect of exchange on the valence electron bands. On the left of the diagram, there is equal occupation between the up

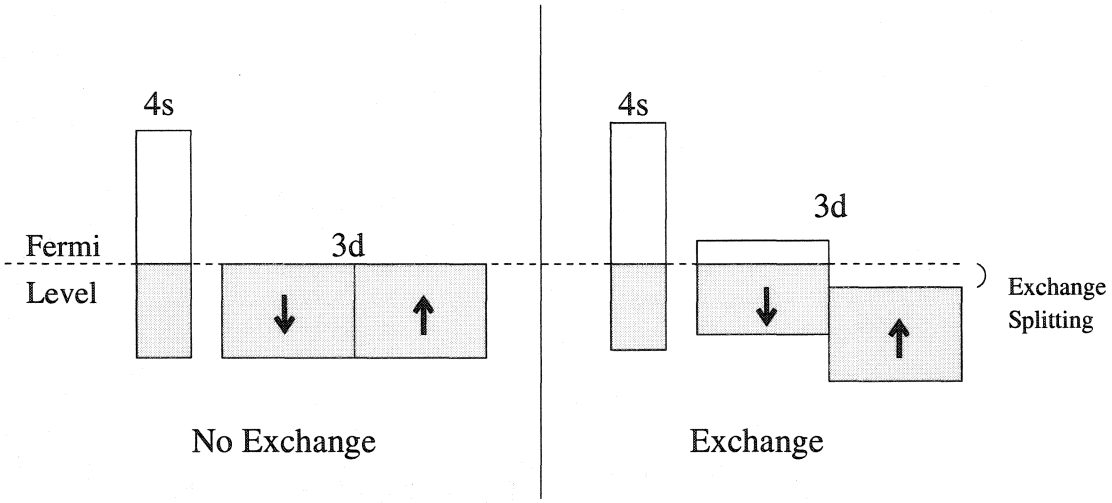

Figure 2.3: Exchange level splitting. Figure modeled on similar figure in Kittel[1]

and down spin states with some sharing with the 4s state. The presence of exchange (shown on the right) lowers the spin-up state and raises the spin-down and leads to a net, non-zero magnetic moment.

The local moment theory of magnetism is a very phenomenological approach proposed by Heisenberg and also contains many important insights into magnetic behaviour and is the usual first step in many statistical theories of magnetism. The basic Heisenberg Hamiltonian takes the form:

$$\mathcal{H} = -J \sum_{i,j}^{NN} \sigma_i \cdot \sigma_j \tag{2.13}$$

where J is an energy term associated with the exchange integral that sets the strength of the interaction, σ represents localised vector spins and NN signifies the sum is performed over all near-neighbours. This simple equation is very powerful and is the basis of many theoretical examinations of the magnetic phenomenon. The sign of J sets whether the interaction is ferromagnetic ($+J$) or antiferromagnetic ($-J$).

2.3 Magnetic Anisotropy

The discussion on magnetism so far has been about how the spins spontaneously align. There has been no mention of whether or not there are preferred directions for the spins to point within the lattice. Such a direction, if it exists, is chosen by the magnetic anisotropy. The anisotropy is defined as the energy dependence on the direction of the magnetisation. It has its source in several different effects, the principle two of which will be discussed here as they are the most important in magnetic ultrathin films. They are crystalline anisotropy and the shape (or dipole) anisotropy.

2.3.1 Crystalline Anisotropy

The origin of the crystalline anisotropy is in the spin-orbit coupling term of the Hamiltonian and how it affects the itinerant electron bands that have degeneracies (either by symmetry or by accident) near the Fermi energy. The degeneracy is lifted by the inclusion of a spin-orbit term in the Hamiltonian, which is usually formally written as:

$$\mathcal{H}^{SO} = \xi(r)\mathbf{L}\cdot\mathbf{S} \tag{2.14}$$

where:

$$\xi(r) = \frac{1}{2m^2}\frac{1}{r}\frac{\partial V}{\partial r} \tag{2.15}$$

where V could be the center potential due to the atomic nucleus.

Degeneracies can generally occur at any energy in $\mathbf{k}$-space, but most often one finds them at high symmetry points in the lattice. At these points, the degeneracy is removed as the spin-up bands and the spin-down bands are split in energy. At the point on k-space where the degeneracy would occur, the spin-up and spin-down band states combine to form a linear combination of both states (the combination

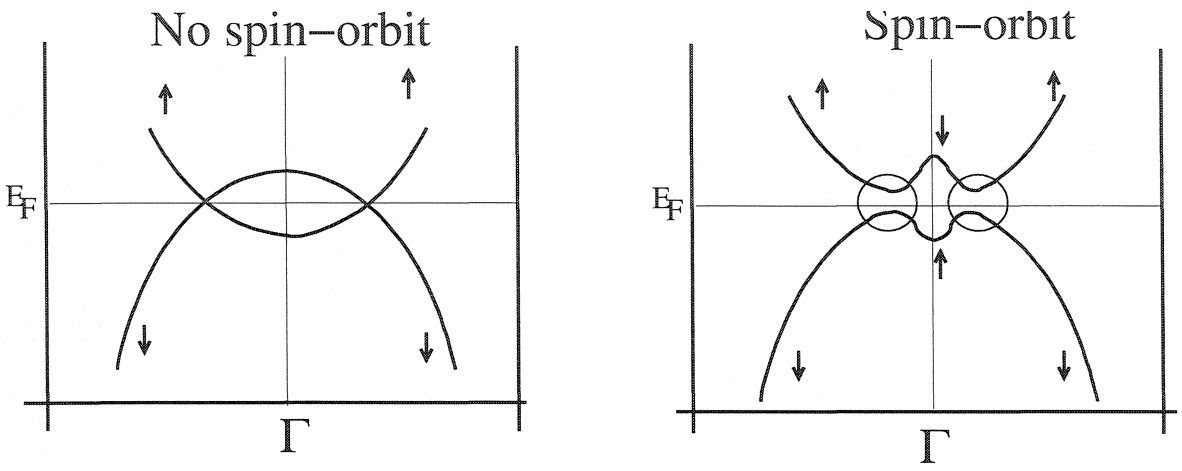

Figure 2.4: Modeled energy bands plotted through a small area of k-space around the symmetry point Γ. Ovals show the area where spin-up and spin-down bands overlap and mixing of state occurs. SO removes the degeneracy and lowers the energy of the spin-up band at the symmetry point.

is complicated and dependent on the value of **k**). Figure 2.4 shows two electron bands with degeneracies near the symmetry point Γ. The figure on the left shows the degeneracies near the Fermi energy (E_F) that exist when spin-orbit coupling is neglected, while the right shows how the energy of the occupied band is reduced at Γ. For the 3d metal ferromagnets, the 3d bands are all tightly located near the Fermi surface, making the overlap more common that in other metals.

The extent to which the energy is reduced is also dependent on the direction of the spin, as seen by eq.(2.14). The orbital angular momentum has a directional component that is affected by the crystal field and therefore tends to take on the symmetry of the lattice itself. The coupling of the spin angular momentum to the orbital means that the spin direction would also prefer to take on this symmetry.

The anisotropy energy is usually treated in a much more phenomenological fashion than exact treatments of the spin-orbit coupling. The usual way to write the

anisotropy energy is of the form:

$$E_A = K_1 F_1(\theta, \phi) + K_2 F_2(\theta, \phi) + \mathcal{O}(3) \tag{2.16}$$

where K_i are constants and F_i are angular functions that describe the dependence of the energy on the angular orientation of the magnetisation (the i subscript merely refers to the order of the term). The first term is almost always the dominant term and it is usually sufficient to include only the first two terms.

Ultrathin film magnetism also must include effects of the anisotropy that arise from the presence of surfaces and interfaces. Neel[20] first proposed that any magnetic system that was less than $100\mathring{A}$ must take interface effects into account. He proposed a phenomenological approach to calculating the anisotropy energy for planes where translational symmetry is broken. He wrote a pair-model lattice sum equation given by:

$$K_i = \sum_{j}^{NN} \eta L_{i,j} (\hat{r_{i,j}} \cdot \hat{M})^2 \tag{2.17}$$

where $L_{i,j}$ is a coupling constant between atoms i and j, $\hat{r}$ is the unit vector between the atoms, $\hat{M}$ is the unit vector pointing in the direction of the magnetisation, and η is a factor that equals 1/2 if both atoms are magnetic and equals 1 if only one is magnetic. The sum is performed only over near neighbours (NN) as would be expected near surfaces.

2.3.2 Shape Anisotropy

Shape anisotropy is an important effect especially in surface magnetism where local crystal symmetry breaking is much more important than for most bulk magnets. The origin resides in the dipole field created by individual moments. These fields give rise to the *demagnetisation factor*, which acts to restrict the magnetic moment to align

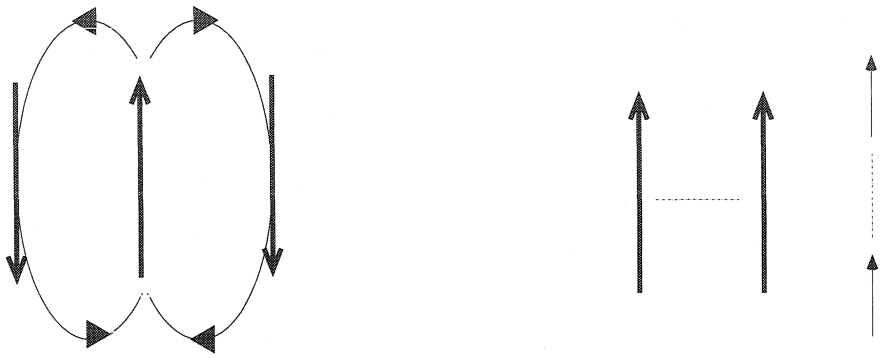

Figure 2.5: Dipole Diagram

itself in such a fashion as to limit the amount of stray fields that exist outside the sample. The dipole energy Ω of a lattice of spins can be written as:

$$\Omega = \frac{\Omega_o}{2}\left(\sum_{i,j}^{N}\frac{S_i \cdot S_j}{r_{ij}^3} - 3\sum_{i,j}^{N}\frac{(S_i \cdot \hat{r_{ij}})(S_j \cdot \hat{r_{ji}})}{r_{i,j}^3}\right) \tag{2.18}$$

where Ω_o is a constant and $\hat{r}_{ij}$ is a unit vector between spins i and j. The first term tells us that the energy of the spin system is reduced if the moments are anti-parallel (figure 2.5) and thus this term acts against ordering in a ferromagnet (the exchange interaction is usually more than an order of magnitude stronger). The second term says that the dipole energy is reduced more significantly if the moments are aligned, in a sense, tip-to-tail as seen in the right diagram in figure 2.5. This significantly increases the energy if there are moments that exist at the system boundary with the direction of the moments oriented perpendicular to the system boundary. The long range $1/r^3$ nature of the interaction is truncated at the boundaries of the system and is therefore dependent upon the shape of the sample (hence the name). The shape anisotropy is responsible for the creation of "capping" domains in bulk materials and is the reason why the long axis of an iron bar magnet is always the easy axis of the magnetisation.

The dipole field is sometimes called the demagnetising field because it acts

Table 2.1: Table of N values for various geometries.

Geometry	N_x	N_y	N_z
Sphere (x=y=z)	$\frac{1}{3}$	$\frac{1}{3}$	$\frac{1}{3}$
flat plate (x=y=∞ ,z=0)	0	0	1
long cylinder (x=y, z=∞)	$\frac{1}{2}$	$\frac{1}{2}$	0

against ferromagnetic ordering. A geometric argument has been formulated to calculate the demagnetising field based on the factor N, called the *demagnetisation factor*. The demagnetising field for a uniformly magnetised ellipsoid is written as:

$$H_d = -NM \tag{2.19}$$

where N is calculated based on the macroscopic geometry of the system and the direction of the magnetisation. There is an N factor for each principle direction in the magnet (N_x, N_y, N_z) and the sum of them must equal 1. Values of N for various geometries are given in table 2.1.

An ultrathin film with the moment oriented in-plane is approximated by a flat-plate geometry. A more general treatment of systems where the two lateral directions are much greater than the third axis ($a > b >> c$) is [21]:

$$N_a = \frac{\pi}{4}\frac{c}{a}\left(1 - \frac{a-b}{4a} - \frac{3(a-b)^2}{16a^2}\right) \tag{2.20}$$

and

$$N_b = \frac{\pi}{4}\frac{c}{a}\left(1 + \frac{5(a-b)}{4a} + \frac{21(a-b)^2}{16a^2}\right) \tag{2.21}$$

and by definition, $N_c = 1-(N_a+N_b)$. If we assume that the lateral a and b dimensions are equal in an ultrathin system, then the demagnetisation factor for an in-plane film is proportional to the thickness c divided by the width a. The extreme aspect ratio of ultrathin films means that the N factor can usually be ignored for films magnetised

in-plane but it is extremely important in films that are magnetised perpendicular to the surface.

2.4 Ultrathin Film Magnetism

Thin film magnetic research generally falls into two main categories. There is the basic research and the applied field of data storage and device manufacture. The engineering of magnetic materials with microscopic domain "bits" has been one of the most important drivers of modern information technology. As well as acting as a storage medium, magnetic thin films are also the main component of hard drive read heads. Applications that are the subject of much current research involve topics such as MRAM and spintronic systems, both of which seek to revolutionise computer technology.

The basic research side has approached many different questions that arise from the effect of the extreme dimensionality on magnetic properties. While the theory of Mermin and Wagner[22] forbids magnetic ordering in a two-dimensional system at any non-zero temperature due to the presence of a logarithmic divergence in the density of states leading to long-wavelength spin-wave modes, it has been found that only a small amount of anisotropy is required to remove this restriction [23, 24]. Most traditional studies on two dimensional magnetic systems have used multilayer bulk samples (for example, see [25]), where magnetic layers are separated by non-magnetic spacers. These studies often quote the ratio between interlayer to intra-layer coupling. These ratios, while low, never reach zero and arguably are not true two dimensional materials. However, true two dimensional behaviour will occur in a thin film when the magnetic interactions can be treated as uniform across the thickness of the sample. The two interfaces of the film are against vacuum on one

side and a magnetically inert substrate on the other, thus giving important magnetic properties such as fluctuations and domain wall motion only one "route" to follow through the medium. This makes such systems ideal for examining two-dimensional magnetic behaviour in the laboratory.

The effect of the interface can also lead to a heightening of the magnetic anisotropy energy of the system. Broken symmetry at the surface for cubic systems lead to significant second order terms in the anisotropy energy in the phenomenological formulation [see eq.(2.16, 2.17)] instead of the fourth order as it does in bulk cubic materials. The anisotropy will most often be expressed as an energy per unit volume and this leads to expressions where bulk and surface anisotropy are treated separately as [26]:

$$E_a = K_B + \frac{K_S}{t} \tag{2.22}$$

where E_a is the total anisotropy energy per unit volume, K_B is the bulk anisotropy energy per unit volume, and K_S is the surface energy per unit *of the surface*. Dimensional analysis accounts for the fact that K_S must be divided by the film thickness t. It is straightforward to see that once t becomes large enough, the bulk term will dominate the total energy. Convention states that a positive anisotropy energy value means that the moment of the film prefers to lie in-plane and a negative value for a preferred perpendicular moment [27]. Bulk anisotropy and shape anisotropy will usually prefer an in-plane moment and it can be seen that if K_S is negative and large enough to make E_a negative for thin enough films, a thickness will be realised where the moment will reorient itself from the perpendicular direction to lie in-plane. This is the origin behind the *spin-reorientation transition* [28, 29].

Perpendicular films are themselves interesting for several reasons. As a consequence of the magnetic dipole interaction, they cannot support a single domain state.

It has been found that perpendicular films will break up into alternating domains of up and down spins, the population of which will increase exponentially as a function of temperature [30]. This domain explosion makes the transition temperature extremely difficult to determine experimentally, as the film seems to disorder through domain randomisation as opposed to more usual mechanisms. Perpendicular domain structures are currently under heavy study for the data storage industry as they can be made more compact than in-plane domains, leading to higher density data storage.

Other topics that have been the subject of recent work is the relationship between film stress and magnetic properties [31], looking at the dynamics of spins [32], and the phenomenon of exchange bias [33]. Some work has been done restricting lateral dimensions of the system either by growing the films on specially designed substrates and vicinal surfaces [34] or by using involved lithography techniques [35].

2.5 Phase Transitions

A phase transition occurs whenever a system changes from one phase to another. The definition of 'phase' is somewhat arbitrary, as it only serves to define the status of a material property as it pertains to the value of a defined order parameter. An order parameter is an intrinsic property of the material, meaning that its value is not dependent (at least to first order) upon system size, although there are exceptions to this. Some examples of common order parameters are density, chemical potential, entropy, and magnetic order.

The changing value of an order parameter is usually accomplished by the application of external fields or *extrinsic variables* such as pressure and temperature. Each phase of a material is defined by a certain range of values of its order parameter.

We will use Figure 2.6, which shows the well-known phase diagram for H_2O,

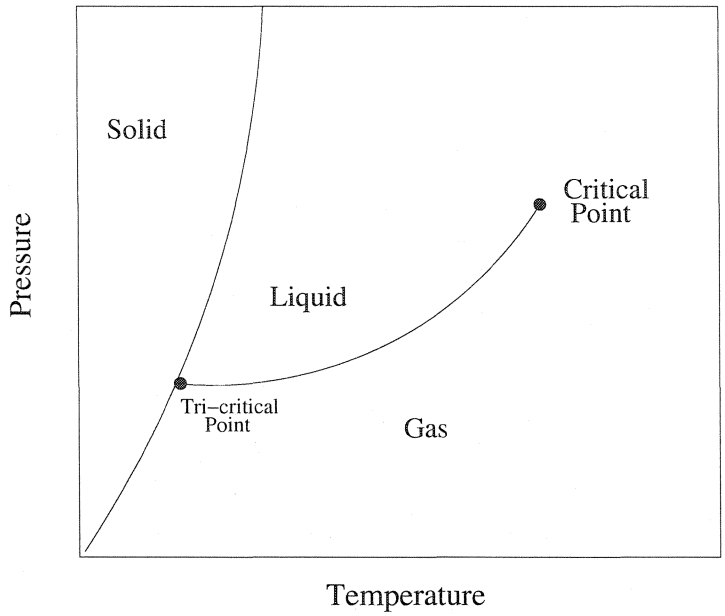

Figure 2.6: Phase diagram of water. Liquid-gas coexistence curve ends at critical point.

as an example to illustrate many concepts of phase transitions. The solid lines of the diagram show phases boundaries where the two phases may coexist. If the pressure or temperature are changed such as to move the phase across a boundary, then a phase transition will occur. In the case of this diagram, the transitions involved are of first order.

The liquid-gas phase boundary ends abruptly with increasing temperature and pressure at a point called the *critical point.* As can be seen, it is possible to change phases of water from liquid to gas by navigating around the critical point in phase space. The solid-liquid-gas curve all intersect at the *tricritical point*, a unique place where all phases can coexist.

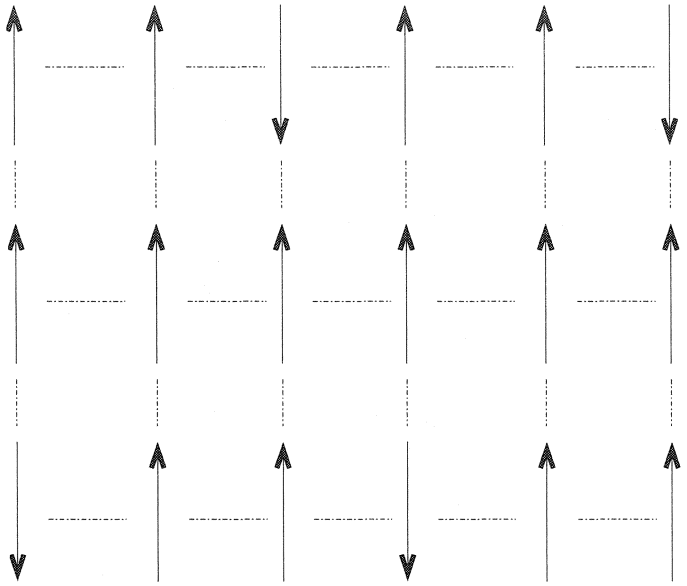

Figure 2.7: Simple schematic of magnetic moments on a lattice.

2.5.1 Mean Field Theory

One of the first successful theories of phase transitions in magnetic systems was *mean field theory*. It makes several assumptions about real systems which are not completely valid for most ferromagnets but provides a good first step in the understanding of the Curie transition.

The first of these assumptions is that magnetic moments are localised on a well-defined lattice, usually the atomic lattice. The second assumption is that, in its most basic form, it deals with only the average magnetisation and as such, neglects the importance of fluctuations in the average system behaviour near T_c. Since these fluctuations, as we shall see later, are extremely important at T_c, it is difficult if not impossible to make accurate predictions of real systems close to the transition using mean field theory.

The following is a typical mean field calculation for a simple magnetic system

of Ising moments[36, 37] (they can have a normalised value of either +1 or -1) going through a phase transition at the Curie temperature. Figure 2.7 shows a square lattice of magnetic moments. The exchange interaction is extremely short range on the order of most inter-atomic interactions, only affecting near-neighbour moments. The first step is to define the Hamiltonian of the system:

$$\mathcal{H} = -J \sum_{i,j}^{NN} (\sigma_i \cdot \sigma_j) - h \sum_i \sigma_i \tag{2.23}$$

where the first term is just the Heisenberg Hamiltonian (J is positive, favouring the ferromagnetic state) and the second term is added to allow for an external magnetic field, h (the field is normalised to correctly give proper energy units), along which the moments will prefer to orient themselves. We now choose an arbitrary center spin (σ_o) from the infinite lattice and rewrite $\mathcal{H}$ for the individual spin as:

$$\mathcal{H}_\sigma = -\sigma_o (J \sum \sigma_i + h). \tag{2.24}$$

$\sum \sigma_i$ is the average total value of the magnetisation in the vicinity of the center spin and is equivalent to mq, where m is the average value of the individual near-neighbour magnetic moments and q is the number of near neighbours (there are four near neighbours in the lattice shown in figure 2.7). Rewriting the Hamiltonian again gives us:

$$\mathcal{H}_\sigma = -\sigma_o (Jmq + h) \tag{2.25}$$

which allows us to define the effective mean field acting upon the center spin as (Jmq + h). We can now write the partition function $\mathcal{Z}$ of the system as the trace of the exponentials of all possible values of the Hamiltonian:

$$\mathcal{Z} = Tr(\exp(-\beta \mathcal{H}_\sigma)) = Tr(\exp(-\beta \sigma_o (Jmq + h))) \tag{2.26}$$

where β is the reciprocal of the Boltzmann constant (k_B) multiplied by the temperature, T. σ_o can only have values of ± 1, so $\mathcal{Z}$ can be written as:

$$\mathcal{Z} = exp(\beta(Jmq + h)) + exp(-\beta(Jmq + h)) = 2\cosh(\beta(Jmq + h)) \tag{2.27}$$

Using well defined statistical mechanics relations, having the partition function allows us to define the free energy of the system as:

$$\mathcal{F} = -k_B T ln(\mathcal{Z}) = -k_B T ln(2\cosh(\beta(Jmq + h))) \tag{2.28}$$

and then the average magnetisation is:

$$m = -\frac{\partial \mathcal{F}}{\partial h} = \tanh(\beta(Jmq + h)) \tag{2.29}$$

This equation is obviously recursive and it is impossible to algebraically isolate m. If we take the case where the external field is zero, there is an obvious solution at m=0 and a second solution that is easiest to see graphically, as in figure 2.8. The existence of a non-zero solution for the magnetisation is dependent upon the value of the argument of the tanh function. For any qJ/k_BT value greater than one, there is a second solution to eq.(2.29) as seen by the intersection of the red and the dotted line in the figure. It is at $qJ/k_BT < 1$ that the second solution is lost. Thus, we find the phase transition occurs at $qJ/k_BT = 1$ and that we can now define the transition temperature T_c as having a value of qJ/k_B.

In a fairly straightforward way, this solution makes sense. The ratio of qJ/k_BT is a relationship between the total energy of the magnetic exchange energy qJ (assuming all moments are aligned as they should be below T_c) and the thermal energy k_BT. What the mean field solution says is that once the thermal energy is greater than the exchange energy, the moments are no longer able to maintain order due to the thermal energy which acts to randomize the moments.

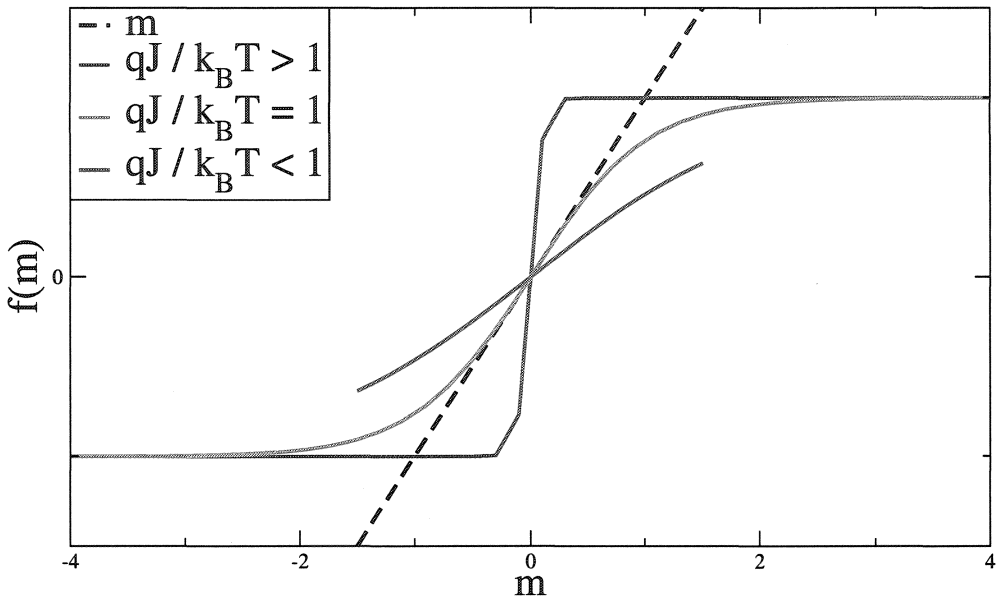

Figure 2.8: Graph showing recursive relationship of m. Red line, showing a stable non T=0 solution indicates T < T_c. Blue line with only T=0 solution is T > T_c and green line represents the point of crossover between the two regimes.

We can take mean field theory a step further and define the susceptibility of the magnetisation above T_c. For temperatures much greater than T_c, we can write the tanh function of the magnetisation as the leading term of an expanding series(though it should be remembered that we are losing some amount of accuracy by doing this), giving:

$$m \approx \frac{Jqm + h}{k_B T} \tag{2.30}$$

and therefore

$$\chi = \frac{\partial m}{\partial h} = \frac{1}{k_B T \left(1 - \frac{qJ}{k_B T}\right)} \tag{2.31}$$

Since we know that qJ/k_B is T_c, what we have left is a susceptibility that diverges to infinity at T_c as a power law with an effective exponent of -1. This relationship is known as the Curie Law and holds true for temperatures well above T_c.

To extract a power-law relationship for the magnetisation as a function of

temperature, we set h=0 and expand the tanh function to higher order. If we write:

$$m = \frac{qJm}{k_B T} - \frac{1}{3}\left(\frac{qJm}{k_B T}\right)^3 \tag{2.32}$$

then we have:

$$m = \frac{T}{T_c}\sqrt{3\left(1 - \frac{T}{T_c}\right)} \tag{2.33}$$

which gives a power-law equation with an effective exponent of 1/2.

By expanding eq.(2.29) to find temperature relationships for the susceptibility and the magnetisation, we make the assumption that the temperature is much greater than and much less than T_c respectively. This assumption illuminates the inherent limitation of mean field theory. It tells us how the system behaves only at temperatures (in this example, though other effective fields for different systems would show the same effect) far away from the transition. As will be seen, it is precisely the effects close to T_c that define the true nature of the transition. The mean field theory presented here also ignores such important phenomenon as easy axis anisotropy and the dimensionality of the system.

2.5.2 Mean Field and Ginzburg-Landau Theory

Ginzburg-Landau (G-L) theory in the simplest form is another formulation of mean-field theory. However, it is much more powerful in extended forms and is a helpful way to examine the nature of phase transition and to show just what system properties are important to the transition.

G-L assumes that the free energy can be written as a polynomial of the order parameter. For an arbitrary system with order parameter m, we can write the Landau free energy $\mathcal{L}$ as:

$$\mathcal{L} = am + bm^2 + cm^3 + ... \tag{2.34}$$

The form of the Landau energy function should reflect the properties and symmetries of the system being modeled. The coefficients $(a, b,...)$ are also dependent on the various coupling constants such as J and also conjugate fields such as temperature and external magnetic fields. For a Ising magnetic system, the free energy must be an even function $[\mathcal{L}(m) = \mathcal{L}(-m)]$ as the sign of the moment is immaterial to the energy of the system. So, right away, we can set all coefficients of odd powers of m to zero. We shall now see that with this form of $\mathcal{L}$, we can easily get the results from section(2.5.1). If we write out $\mathcal{L}$ to $\mathcal{O}(4)$ and make the coefficient of a directly dependent on how close the system temperature is to T_c, we get:

$$\mathcal{L} = a(T - T_c)m^2 + bm^4 \tag{2.35}$$

To determine the magnetisation, we minimize by differentiating $\mathcal{L}$ with respect to m, to get:

$$\frac{\partial \mathcal{L}}{\partial m} = 2a(T - T_c)m + 4bm^3 = 0 \tag{2.36}$$

Solving for m, this becomes:

$$m = \sqrt{\frac{-a(T - T_c)}{2b}} \tag{2.37}$$

This result gives us two pieces of information. One is that either of the coefficients a or b must be negative and the second is that the the power-law exponent of the magnetisation $(\frac{1}{2})$ is the same as the exponent discovered in section(2.5.1).

We can also look at the result for the susceptibility. If we add in a small external field h, $\mathcal{L}$ becomes:

$$\mathcal{L} = a(T - T_c)m^2 + bm^4 + hm \tag{2.38}$$

where, since the field breaks the Ising symmetry, the field must be associated with an odd exponent of m. Since the field is small, we only include the first odd power

and we will neglect the m^4 term as well. Differentiating as before and then taking the derivative with respect to h gives:

$$\chi = \frac{\partial m}{\partial h} = \frac{1}{2a(T - T_c)} \tag{2.39}$$

which again retrieves the mean field result for the power-law exponent for the susceptibility -1.

2.6 Power Laws and Critical Exponents

It was seen as statistical mechanic theory became advanced beyond mean field theory that many systems that undergo a phase transition as a function of some external variable did so as a power-law of that variable. Temperature, density, and pressure are the most common (though in no way the only) extrinsic variables that appear. These expressions that arise from the free energy are often expressed as a function of the proximity of the value of the extrinsic variable to the critical value where the phase transition occurs. For systems where a transition can occur as a function of two or more variables, you can have, as seen in figure 2.6, a critical point where the two effects intersect in the relevant phase space.

Critical exponents calculated via mean field theory have little significance in real-world systems as they are found in a model that ignores the very important effect of fluctuations at the critical point. While it is obvious that no expression of a power-law function will be analytical at the divergent point, it is possible to construct theories that take these fluctuations into account and make predictions about critical exponents possible. The basis of almost all of this type of work is the powerful technique referred to as *renormalization group theory.* The depth of this theory is profound and will not be delved into too deeply in this chapter, except to outline its basic precepts and to briefly derive some simple results that arise from them.

2.6.1 Scaling and Scaling Laws

Fluctuations in the order parameter have associated with them a *correlation length* that diverges at a phase transition. In simplest terms, the correlation length is the extent that a fluctuation affects the system's inherent order. If the system has a correlation length of $100\mathring{A}$ then all local values of the order parameter within that length will exhibit some effect due to that fluctuation. The fact that the correlation length (symbolised by the Greek letter ξ) diverges to infinity at the transition forms the basic foundation of the renormalised group.

Kadanoff[38] (and later, more rigourously, Wilson[39]) proposed the idea that since ξ gets so large at the transition, the microscopic details of the system are no longer as important as the global, macroscopic behaviour. If the system can be redefined on a longer length scale than individual lattice sites with local values of the order parameter, the newly defined basic block of the averaged order parameter will then ignore all fluctuations that are smaller than the basic block of spins. But (and this is the clever bit) if it is only the long-scale correlated fluctuations that matter at the transition (remember that $\xi \rightarrow \infty$ as $T \rightarrow T_c$), then this new renormalised system should have the same critical exponents as the unnormalised system. The chief argument of scaling theory is that the free energy does not change with the renormalisation of the length scale.

Scaling laws are relationships between critical exponents that arise from this idea. If we use the common definition of the specific heat ($C(t) = C_o\epsilon^{-\alpha}$ where ϵ is the reduced temperature ($T\text{-}T_c$)) and we rescale the temperature by λ, we get:

$$C(\lambda\epsilon) = KC[\epsilon] \tag{2.40}$$

where K is a scalar that rescales the specific heat for the newly renormalised system.

We can now find the analytical form for K by writing:

$$C(\lambda\epsilon) = C_o[\lambda\epsilon]^{-\alpha} \tag{2.41}$$

which then gives us:

$$C(\lambda\epsilon) = \lambda^{-\alpha}C[\epsilon] \tag{2.42}$$

Comparing eqs.(2.40) and (2.42) tells us that K is equal to $\lambda^{-\alpha}$ and we now have an expression for the critical exponent:

$$\alpha = \frac{-ln(K)}{ln(\lambda)} \tag{2.43}$$

This rescaling argument is true and therefore universal for all systems as long as the specific heat behaves as a power law near the transition.

Rushbrooke Scaling Law

One of the most well-known of the scaling laws is the Rushbrooke scaling law[40]. It states that:

$$\alpha + 2\beta + \gamma = 2 \tag{2.44}$$

where, to repeat, α, β, and γ are the critical exponents associated with the specific heat, the order parameter, and the susceptibility respectively. This law is universal for all systems that undergo a phase transition. As such, its derivation is of the most general sort and is based almost solely on scaling arguments. To begin outlining this derivation (following the formalism from Stanley[41] and Collins[2]), we write the rescaled free energy as:

$$\mathcal{F}(\lambda^{y_t}\epsilon, \lambda^{y_h}h) = \lambda^d\mathcal{F}(\epsilon, h) \tag{2.45}$$

where y_t and y_h are exponents related to the dimensionless reduced temperature ϵ and to the conjugate dimensionless field h ($h = \frac{\mu g H}{k_b T}$) respectively and d is the

system dimension. Scaling theory makes the assumption that the free energy is a homogeneous function[41] with a solution of the form:

$$\mathcal{F}(\epsilon, h) = |\epsilon|^x g\left(\frac{h}{|\epsilon|^{\frac{y_h}{y_t}}}\right) \tag{2.46}$$

where g is an arbitrary function. Now we can write::

$$\mathcal{F}(\lambda^{y_t}\epsilon, \lambda^{y_h}h) = (\lambda^{y_t}|\epsilon|)^x g\left(\frac{h}{|\epsilon|^{\frac{y_h}{y_t}}}\right) = \lambda^{xy_t}\mathcal{F}(\epsilon, h) \tag{2.47}$$

From this and eq.(2.45), we get a solution for x:

$$x = \frac{d}{y_t} \tag{2.48}$$

With an expression for the free energy, we can now go on to derive the important statistical quantities. First, the specific heat in zero field:

$$C = -T\frac{\partial^2 \mathcal{F}(\epsilon, 0)}{\partial \epsilon^2} = (x-1)x|\epsilon|^{-(2-x)}g(0) \tag{2.49}$$

This means that in this formulation, $2 - x = \alpha$ and therefore we can now relate the dimensionality of the system d to the specific heat exponent by using eq.(2.48) to get:

$$2 - \alpha = \frac{d}{y_t} \tag{2.50}$$

The magnetisation of the system can be written as (using eq.(2.50)):

$$m = \frac{\partial \mathcal{F}}{\partial h} = |\epsilon|^{2-\alpha} g'(0)\frac{1}{|\epsilon|^{\Delta}} = g'(0)|\epsilon|^{2-\alpha-\Delta} \tag{2.51}$$

where Δ is inserted for $\frac{y_h}{y_t}$ and $g'(0)$ is the first derivative of the arbitrary function g with respect to the field and then evaluated at h=0. Since the exponent for the magnetisation is defined as β, this gives us an expression for Δ in terms of the established exponents:

$$\Delta = 2 - \alpha - \beta \tag{2.52}$$

For the last step in this derivation, we calculate the susceptibility in zero field as follows:

$$\chi = \frac{\partial m}{\partial h} = \frac{\partial^2 \mathcal{F}}{\partial h^2} = |\epsilon|^{2-\alpha-2\Delta} g''(0) \tag{2.53}$$

where g'' is the second derivative of g with respect to h. The critical exponent for the susceptibility is defined as γ, so we can now finally write:

$$\gamma = 2\Delta + \alpha - 2 \tag{2.54}$$

and then substituting eq.(2.52), we have at last:

$$\alpha + 2\beta + \gamma = 2 \tag{2.55}$$

in agreement with eq.(2.44).

This derivation was made without regard for the exact nature of the free energy, only that it obey scaling and basic dimensional analysis. Thus, the Rushbrooke Law will apply across all universality classes. It also tells us that once we have two of the exponents then no further calculation is necessary to find the third, making for a truly powerful relationship.

Other Scaling Laws

There are other scaling laws that will be listed here. They are:

$$\beta\delta = \beta + \gamma \tag{2.56}$$

where δ is the exponent associated with the critical field ($h^{\frac{1}{\delta}}$ as $t \to 0$). Also, there is Fisher's Law:

$$\gamma = \nu(2 - \eta) \tag{2.57}$$

where ν is the exponent associated with the correlation length ξ and η is an exponent that is by definition expressed in terms of the correlation function $\mathcal{C}$ at the critical

point as:

$$\mathcal{C}(r) = r^{2-d-\eta} \tag{2.58}$$

We can test these laws quickly using the mean field exponents (α=0, β=1/2, γ=1, δ=3, ν=1/2, η=0) to find:

$$\alpha + 2\beta + \gamma = 0 + 2\left(\frac{1}{2}\right) + 1 = 2 \tag{2.59}$$

Confirming the others is left as a mental exercise for the reader.

2.6.2 Universality Classes

It was soon confirmed that the critical exponents of a system undergoing a phase transition were dependent not upon the microscopic details of the Hamiltonian but on more macroscopic properties. Systems that classically have seemingly very little similarity exhibited the same behaviour as it approached the transition. For the case of static phase transitions, the important properties were the dimensionality of the system d and the degrees of freedom of the order parameter D. Systems that shared these properties are grouped together into their universality classes and each class has its own set of exponents.

Table (2.2) shows a few examples of different classes and their exponents. The mean field model is now known to the reader. Ising systems are models where the local order parameter can have one of two possible values at each individual site in the lattice. 2d and 3d refers to the dimensionality of the lattice. X-Y is a system where the order parameter is a vector that is constrained to values within the x-y plane. Heisenberg systems are one where the order parameter is free to move in three principle quadrature directions and spherical means the vector moment is free to take on any value within the full 4π degrees of freedom.

Table 2.2: Various universality classes and their associated exponents. Values quoted taken from Collins([2]). Values given without decimal or as fractions are exact, all others are estimates from both theory and experiment.

Model	Mean Field	2d Ising	3d Ising	X-Y	Heisenberg	Spherical
D	all	1	1	2	3	∞
d	all	2	3	3	3	3
ν	0	1	0.6312	.669	0.707	1
α	-	0	0.106	-0.01	-0.121	-1
β	1/2	1/8	.326	0.345	0.367	1/2
γ	1	7/4	1.2378	1.316	1.388	1
δ	3	15	4.78	4.81	4.78	5
η	0	1/4	0.039	0.03	0.037	0

Some classes have exact solutions such as the 2d Ising system that was solved analytically by Lars Onsager in what is often called a mathematical *tour de force*[42]. Most other models have no exact solution. The inexact numbers from the table reflect the best estimate from theory and experiment.

This thesis deals with experiments performed on a magnetic system that will be shown to be a 2d Ising system. However, the 2d Ising class includes non-magnetic systems as well. The Ising class can almost be thought of as a binary system, where the local order parameter can have only one of two values. A system of spins that are either up or down can easily be mapped onto an on/off, true/false system. Indeed, this is the basis of the entire magnetic data storage industry and will be for many years to come. Lattice gas absorption can be modeled as a 2d Ising system, where a lattice point can either be occupied or not. The average vacancy state of the system is the order parameter.

2.7 Dynamic Properties and Critical Slowing Down

The properties of phase transitions that have been discussed up to now are what are referred to as static properties. All the arguments made thus far have assumed that all processes occur infinitesimally slowly on an infinite time scale. In actual fact, there is time dependence involved in the equilibration of the system at a given temperature. This is the subject of *dynamic scaling.* The time for the order parameter to return to equilibrium after a fluctuation scales with the correlation length ξ as:

$$\tau(T) \propto \xi(T)^z \tag{2.60}$$

and therefore the temperature dependence of the relaxation rate goes as:

$$\tau(T) = \tau_o \epsilon^{-z\nu} \tag{2.61}$$

where z is the *critical slowing down exponent.* Dynamic scaling universality classes depend on the same system properties as the static classes with the extra condition regarding conservation laws of the order parameter with respect to the system Hamiltonian.

To see in more detail how dynamic scaling comes about, we follow the formulation given by Goldenfeld [36] and Hohenberg [43] and use time dependent Ginzburg-Landau theory with the Markoffian equations of motion where:

$$\frac{\partial m}{\partial t} = -\Gamma \frac{\delta \mathcal{L}}{\delta m} \tag{2.62}$$

where Γ is a damping coefficient that does not diverge at the critical point, m is the order parameter, t is time, and $\mathcal{L}$ is the Landau free energy which to low order is given as:

$$\mathcal{L} = \frac{1}{2}\gamma(\nabla m)^2 + a\epsilon m^2 \tag{2.63}$$

where the first term is the standard spatially varying term added to introduce fluctuations and ϵ is again the reduced temperature $\frac{|T-T_c|}{T_c}$.

In the linear approximation for small deviations, the time rate of relaxation is defined as:

$$\frac{\partial m}{\partial t} = -\frac{\delta m}{\tau} \tag{2.64}$$

Equating the right-hand side of eqs.(2.62) and (2.64) and differentiating $\mathcal{L}$, we get:

$$\frac{\delta m}{\tau} = \Gamma\left(\gamma\nabla^2 + 2a\epsilon\right)\delta m \tag{2.65}$$

where we set m to a value of δm. To get a clearer understanding of the spatial fluctuations, it is advantageous to take the Fourier transform to get:

$$\frac{\delta m_k}{\tau} = \Gamma\left(\gamma k^2 + 2a\epsilon\right)\delta m_k \tag{2.66}$$

Eq.(2.66) gives us an expression with two terms for the relaxation time τ. The first:

$$\frac{1}{\tau_u} = 2\Gamma a\epsilon \tag{2.67}$$

is uniform and will diverge at T_c. In fact, we can rewrite this term in terms of the mean-field susceptibility from eq.(2.39) as:

$$\frac{1}{\tau_u} = \frac{\chi}{\Gamma} \tag{2.68}$$

The second term contributing to τ is non-uniform and is given by:

$$\frac{1}{\tau_k} = \Gamma\gamma k^z \tag{2.69}$$

where z is the exponent of $\mathbf{k}$ that has, as we've seen in eq.(2.66), a value of 2 in this mean-field treatment. We change the value of 2 to a generic exponent to make for a more general approach.

Both equations 2.67 and 2.69 are the limits of the relaxation time for **k** going to zero and for when T=T_c respectively. A single scaling function to satisfy both of these conditions is given as:

$$\tau(\epsilon) = \epsilon^{-y} g(k\xi) \tag{2.70}$$

where $g(k\xi)$ is an arbitrary function of the wave-vector **k** and the correlation length ξ. g must be a function of k and ξ and is assumed to be a function of the product of those terms to satisfy dimensionality. This equation is the *dynamic scaling assumption* [43] and has its origin in classical theories of relaxation[44].

The scaling function consists of a reduced temperature component that diverges with a generic critical exponent y. According to the scaling assumption, the g function does not diverge as $\epsilon \to 0$ and as such, the diverging nature of ξ must be addressed ($\xi \propto \epsilon^{-\nu}$ as T $\to$ T_c). To remove the divergence, g(kξ) is set to $(k\xi)^{\frac{-y}{\nu}}$. This cancels out both the divergence in ξ and the prefactor ϵ^{-y}. Since eq.(2.69) states that at T=T_c, τ must go as k^{-z}, this gives the scaling relation:

$$z = \frac{y}{\nu} \tag{2.71}$$

Substituting this back into equ.(2.70) gives:

$$\tau(\epsilon) = \epsilon^{-z\nu} g(k\xi) \tag{2.72}$$

which gives the same reduced temperature dependence as the result quoted in eq.(2.61). It is seen that the arbitrary exponent z is now (perhaps not so surprising to the far-sighted reader) formally identified as the critical slowing down exponent.

Chapter 3

Experiment

3.1 Introduction

This chapter will describe the details of the experiments performed in this thesis. The format of the following presentation will be in the form of a step-by-step process, from the preparation of the vacuum environment to the final susceptibility measurement, used to make magnetic measurements from ultrathin films. While the main conclusions of this thesis rely on measurements of the magnetic susceptibility, various other measurements and techniques (some unique to surface science) are important to the final results. By the end of the chapter, the reader will know in some detail how the susceptibility data in figure 3.1 was measured.

Sections will include information on the basics of ultra-high vacuum (UHV). The necessity and the realization of UHV environments will be discussed in detail. The process of *molecular beam epitaxy* that is used to grow the films will be outlined with a brief section on the choice and preparation of the substrate upon which the films are grown. Film growth, thickness, and quality is tested using *Auger electron spectroscopy (AES)* and *low energy electron diffraction (LEED)*. Magnetic properties are measured using *surface magneto-optic Kerr effect (SMOKE)*, which is used to make measurements of both magnetic hysteresis and magnetic susceptibility.

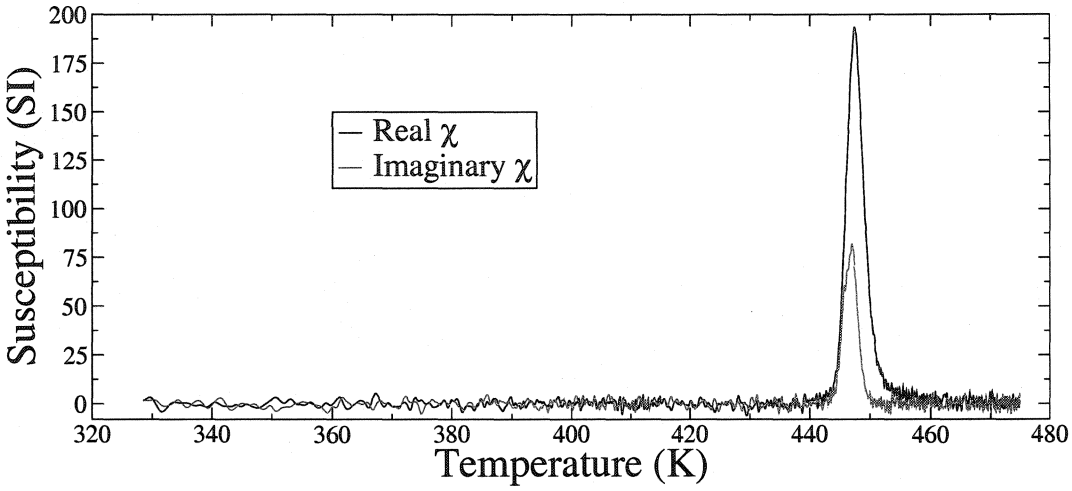

Figure 3.1: Typical measurement of the magnetic susceptibility from an ultrathin film of Fe/W(110). Both the real and the imaginary part of the complex susceptibility are shown.

3.2 Ultra-high Vacuum Environment

The ultrathin limit in film growth usually means a thickness of between one and ten atomic layers or monolayers (ML). Such an extreme aspect ratio means that the samples are extremely sensitive to contamination and thus experiments require excellent vacuum conditions for both ensuring proper film growth and for providing a sufficient time window for the subsequent studies to be performed *in situ*. The minimum base vacuum required for such work is in the range of 10^{-10} torr (which corresponds roughly to about one ten-trillionth ($\frac{1}{10,000,000,000,000}$) of a standard atmosphere). Pressure at this extremely low level allows for several hours of experiment time before contamination sets in and possibly changes the film properties.

This section will detail the procedure of how a vacuum chamber is prepared so as to achieve UHV pressures. Qualitatively, this information will apply to all general UHV systems but it should be understood that all numbers and times quoted are appropriate to a chamber of similar dimension to the one used in the research of this

thesis.

Basic UHV chambers (refer to diagram in figure 3.2) are equipped with several pumps that are designed to act most efficiently over various different ranges of the pressure. In the process of pumping a chamber down from atmosphere, the first step is to use a mechanical rotary pump. After sufficient time, this will reduce the pressure down to approximately 10^{-4} torr, or even lower with the use of a cold trap. A cold trap is a complicated u-tube on the pump fore-line before the chamber that is cooled in a liquid-nitrogen bath. This allows molecules in the flow to become "trapped" on the walls of the trap and not diffuse back into the chamber. This also serves the task of preventing oil molecules from the rotary pump from diffusing forward and disastrously contaminating the chamber. Prolonged use of a cold trap (about an hour or so) allows for a base pressure using only the mechanical pump to reach a low enough pressure to allow the pump line to be valved off and to allow the opening of a gate valve into a secondary chamber containing an already operating ion pump, which quickly reduces the pressure of the entire system down to a pressure in the range of 10^{-6} torr.

The ion pump works by ionising individual particles in a plasma localised in a strong magnetic field. A strong electric field is then used to accelerate the ions into a titanium plate that is several millimeters thick. The gas particles will become embedded in the plate with an extremely low probability of ever becoming disassociated from the target. The efficiency of an ion pump varies depending on the particles being removed from the chamber, but works very well on usual atmospheric gases like nitrogen and oxygen.

The ion pump operates continuously from this point on, maintaining low pressure. It acts as the primary pump during the "bake-out" process, which is when

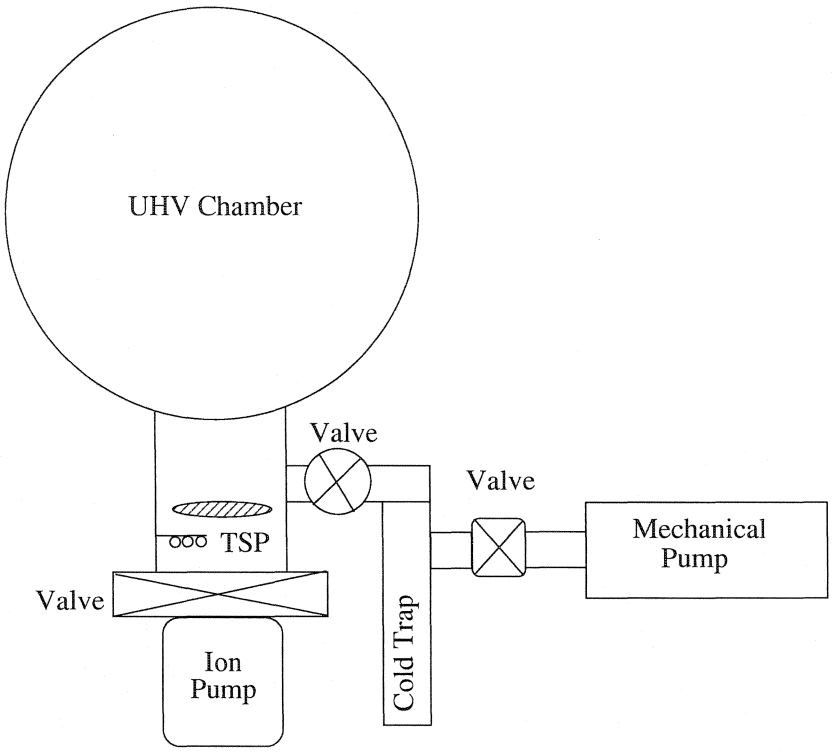

Figure 3.2: Diagram of UHV chamber with associated pumps.

the chamber is heated as evenly as possible typically to about 150°C. This will remove water vapour and as much of the adsorbed gas off of surfaces as possible. The bake-out will usually operate for about 12-24 hours, the length of time depending on several factors such as how long the chamber has been exposed to atmosphere, whether new equipment has been installed within the chamber, and environmental concerns such as ambient humidity levels in the lab. After bake-out and once the chamber has cooled back to room temperature, the pressure will be in the low-10^{-9}torr range.

At this stage, the titanium sublimation pump (TSP) is used to reduce the pressure to the final base level of low-10^{-10} torr. The TSP consists of thick ($\approx$ 2cm) filaments of titanium that are heated to high temperature by the application of high current (45A). In the time span of about 1 minute or less, the filament sublimates and deposits a layer of titanium on the sides of the chamber (the area of the chamber where

this occurs usually has a plate or some other kind of barrier to prevent deposition of titanium on the more sensitive experimental apparatus). Titanium has what is referred to as good "getting" qualities. This means that any atoms that interact with it tend to strongly adsorb (a property that is exploited in the ion pump as well). Many gas atoms such as nitrogen are very reactive with titanium and will form stable compounds with it. These compounds are then either firmly fixed to the side of the chamber or are efficiently pumped away by the ion pump.

Once various instruments in the chamber have undergone a "degas" (heated up or actuated so as to remove any remnant surface contamination), the chamber is now ready for surface science. This entire process takes between 24-48 hours.

3.3 Considerations for Film Growth

To successfully fabricate quality magnetic ultrathin films, there are several considerations that need to be addressed. Not all materials will deposit in a controlled fashion on all surfaces. This section will briefly outline the important points involved.

Substrate

A good substrate for use in a magnetic ultrathin film study should possess several qualities.

(1) It should be non-magnetic. It is probably too obvious to point out that any net magnetic moment present in the substrate will overwhelm any measurement of film properties.

(2) It usually should be composed of a material from which large single crystals can be produced. This ensures that the film structure will be uniform across a measurable area. Also, it should be polishable to a high-degree so as to present a very regular surface and have as few atomic steps as possible, assuming of course that

one does not wish to study the effects of such steps.

(3) The lattice constant between atoms at the surface should ideally match well with the bulk lattice constants of the film material. Films of thickness of less than about three monolayers will sometimes grow pseudomorphically, which means they will use the atomic structure of the surface as a template for its own growth. Even if the film takes on its own structure from the start of growth, it is usually best that the strain at the interface be as small as possible. This is best accomplished by lattice matching.

(4) If the film is to 'wet' the surface (grow in flat, two dimensional layers, not in three dimensional blobs), then the surface energy per unit area of the substrate should be higher than the equivalent surface energy presented by the film. This high surface energy also prevents the formation of surface alloys at the interface. It is worth mentioning that if one wishes to do experiments on three dimensional blobs with interface alloying, then the opposite properties are what is sought.

(5) An added plus to any substrate choice is that it should be easy to clean. The maxim that 'cleanliness is next to godliness' is not more true anywhere else than in surface science.

Film

The film must consist of material that can be deposited on the surface in a controlled way. While there are several different methods of deposition, most are not suitable for the careful fabrication process required for films in the ultrathin limit.

For the study of magnetic films, it is usual to use materials that are magnetic in their bulk form. The 3d ferromagnets (iron, nickel, cobalt) have been studied extensively on many different substrates, looking at the effects of strain and structure on magnetic properties.

3.3.1 Molecular Beam Epitaxy

Molecular beam epitaxy refers to the process where a flux of atoms, usually evaporated from a high purity bulk source, is directed at the substrate where they will adsorb to the surface.

The evaporator used in this thesis contains a very high purity (+99.99%) wire of evaporant material held at a voltage of 1750V. The tip of the wire is held about a centimeter behind a ground-potential semi-circular coiled tungsten wire filament that has a current of 4-5A running through it. The heated filament thermionically emits electrons that bombard the tip of the wire and evaporate the material. The end of the evaporator contains two apertures that are aligned towards the center of the substrate where one wishes the deposition to occur. The first aperture is grounded but the second is floating at +23V and is connected to a high-precision electrometer. The electrometer measures a current of ions hitting the second aperture (on the order of nanoamperes) and it is this current, which is quite stable and directly proportional to the flux of atoms leaving the evaporator, that is used to control the amount of material being deposited. Typical second aperture current measured during deposition with an iron source is 1-2nA, which will correspond with sufficient flux of material to deposit a single monolayer in approximately five minutes.

The position of the deposition on the surface is very sensitive to how well centered the source wire is behind the aperture. The profile of the deposition through the second aperture is roughly Gaussian on the surface. In our apparatus, the evaporators are usually oriented to deposit the material at an angle of 30^o from the surface normal, thus allowing for a more even distribution of material along one lateral direction of the surface.

The center of deposition and the spread of material is monitored using Auger

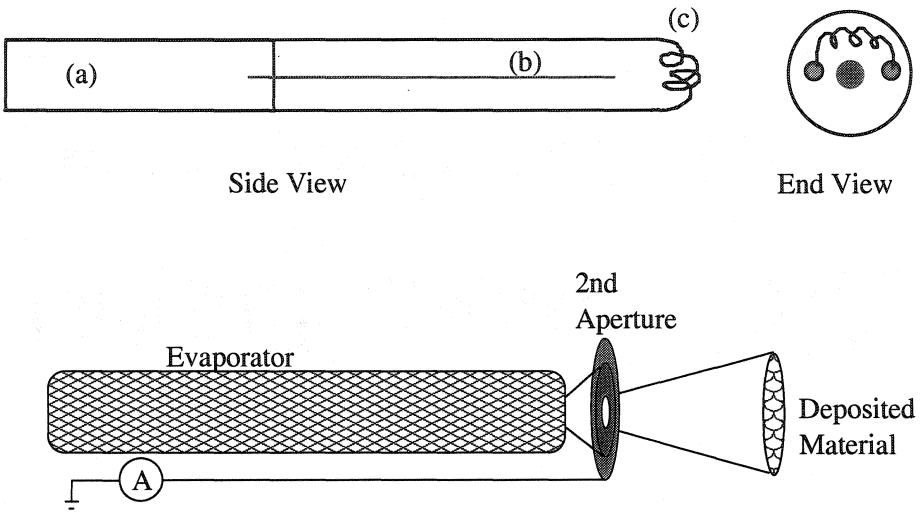

Figure 3.3: A diagram of a molecular beam evaporator of the type used for the experiments in this thesis. (a) is the high voltage post which holds the wire. (b) is the high purity wire source. (c) is the heated filament.

electron spectroscopy which is also the chief method used for measuring film thickness. This technique is the subject of the following section.

3.4 Thickness Calibration using Auger Electron Spectroscopy (AES)

Auger electron spectroscopy is a vital tool in surface science. It is a highly sensitive probe that is chemically sensitive to different species of elements and as such it is extremely useful in making measurements of contamination and film composition. Measured spectra taken both before and after film deposition can be compared and the change in signal can be calibrated to quantify film thickness. Most elements have significant Auger electron energies less than 200eV, thus making it an ideal surface probe.

3.4.1 Basic Physics of Auger Electrons

An Auger electron is produced via a self-ionization process. When an inner-core electron is removed from the atom, the exclusion principle leads to a cascade of higher shell electrons that fall to fill the vacancy. Basic quantum mechanics says that each de-excitation is associated with a quantity of energy related to the spacing of the energy levels. This energy is carried off by a variety of means including photons and the release of an Auger electron.

Auger electrons are produced for the purpose of measurement in the laboratory by bombarding the surface with high-energy (2kV) electrons. The cross-section for an Auger event is quite small in comparison to other effects (such as elastic scattering) but a detectable number of Auger events can be produced with just microamperes of bombardment current from the electron source.

Auger events are commonly labelled according to the energy levels involved in the transitions. An event labelled KLL means than a K-shell electron was ejected from the atom, an L-shell electron fell to fill the now vacant K-shell and a second L electron was ejected to carry away the energy. Figure 3.4 shows a simple schematic of this process.

Auger electrons have an energy typically in the range of 30-600eV. These low energies mean that, according to the *universal curve*, the electrons have an inelastic mean-free path of only three or four lattice lengths. The universal curve[45] is a plot from a series of experiments made in the late 1970s that found that to first order the mean free path of electrons in metals is based on the energy of the electrons themselves and not on the metal they are in. This means only atoms near the surface will emit Auger electrons that will be detectable in the vacuum.

The number of Auger events is quite small in relation to the background

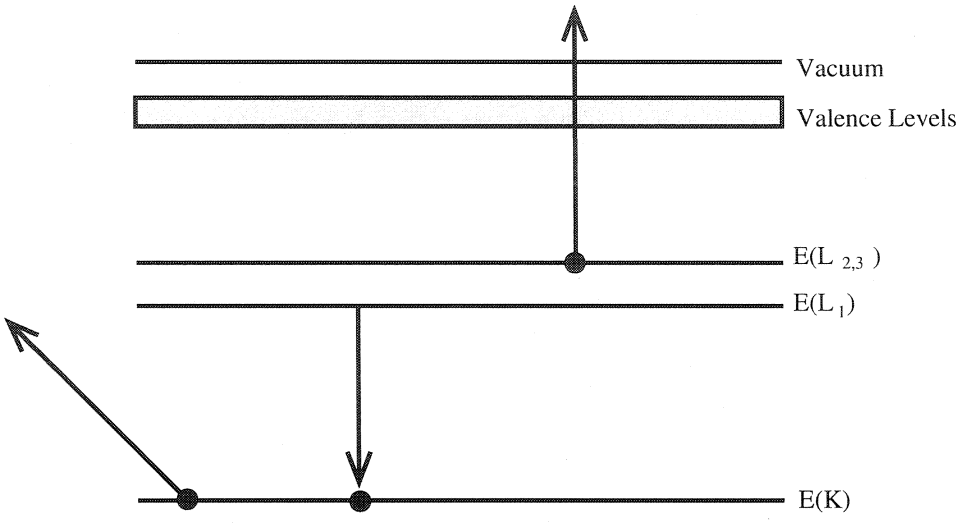

Figure 3.4: Schematic of a typical Auger event. K-shell electron is ejected, L-shell electron De-excites to K-shell and a second L-shell electron (the Auger electron) is emitted. This sequence would be labelled a KLL transition.

events occurring when the surface is being bombarded with the incident, high-energy electron beam. As such, measurement of a high quality spectrum requires a sophisticated technique which will now be described in some detail.

3.4.2 Basic Measurement Technique

The Auger spectrometer used in this thesis is a retarding grid design. It consists primarily of an electron gun capable of providing a small, steady current of high-energy electrons for bombardment, a multi-grid screen for both electron collection and low energy electron retardation, a lock-in amplifier, and a computer for data collection and process control.

To make a simple measurement of an Auger spectrum as a function of kinetic energy E_k, the surface is placed perpendicularly near the electron gun, which protrudes from the center of the collector grid. The retarding voltage on the collector grid (made of a highly conductive, fine gold mesh) is kept at a value to reject any

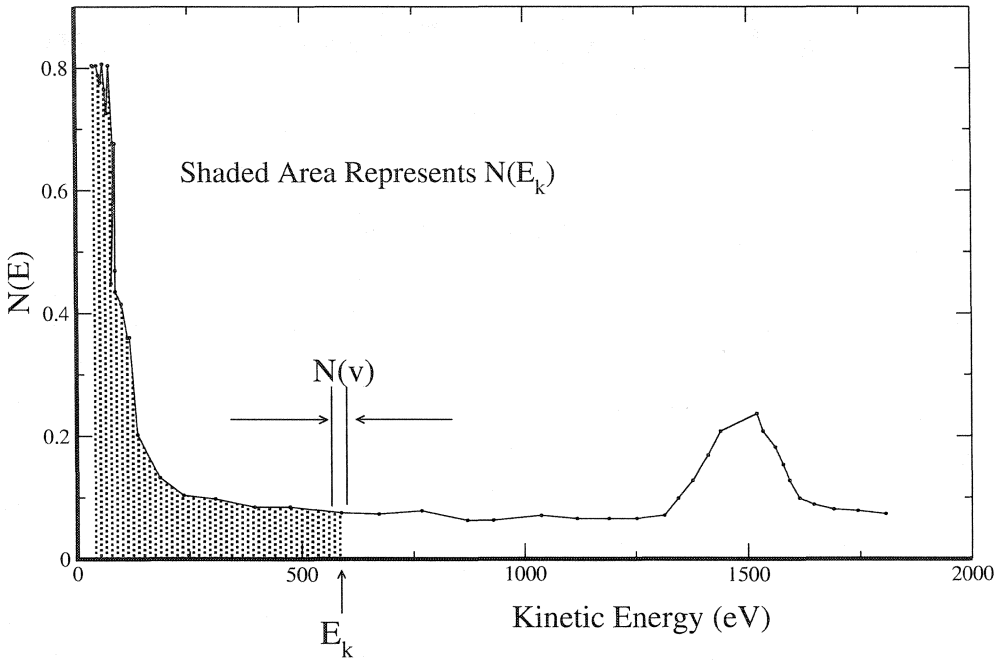

Figure 3.5: Modeled data of Auger electron collection. Shaded area represents all electrons that are collected by the spectrometer. Small interval at E_k represents the electrons that are sensitive to the ac-voltage applied at the collection grid.

electrons with a kinetic energy lower than E_k so that the collected current consists of all electrons with a kinetic energy larger that E_k. The retardation voltage on the grid has a small ac-voltage (v) at a frequency ν of 4.8kHz. By using a lock-in amplifier to measure the component of the current at a frequency ν, one can obtain only the current collected at E_k (see figure 3.5)

As has already been mentioned, Auger electrons form only a small part of the total current measured. Auger events appear in the spectra of N(E) as a small, sharp feature on a slowly varying background. Instead of the number of electrons ($N(E) = \frac{\partial I}{\partial E}$), it is better to measure the differential of the number $\frac{\partial^2(I(E))}{\partial(E)^2}$. This can be accomplished by measuring the current not at the frequency ν but at the second

harmonic, 2ν. This fact can be easiest seen by performing a Taylor expansion on the current as a function of energy. Expanding around the cutoff energy E_k, we get:

$$I(E_k + v\sin(\nu t)) = I(E_k) + v\sin(\nu t)\frac{dI}{dE} + \frac{[v\sin(\nu t)]^2}{2!}\frac{d^2I}{dE^2} \tag{3.1}$$

The second term which is proportional to the modulation frequency ν is also proportional to the number of total electron measured including all backscattered as well as Auger electrons. The third term goes as 2ν $[sin^2(\theta) \propto cos(2\theta)]$, and is proportional to the first derivative of N, dN/dV. Measuring this signal will remove most of the background and leave only Auger peaks which have a much higher first derivative.

3.4.3 Surface Contamination Detection and Substrate Cleaning

Before the film can be deposited, the substrate must be cleaned and checked for any evidence of surface contamination.

All of the experiments in this thesis use a tungsten single crystal substrate that has been cut and polished to expose the (110) crystallographic direction. Tungsten is an excellent substrate for iron films in that it has a very high surface energy and good lattice matching criteria for iron. It also has a very high melting point (3695K), which allows one to use thermal desorption to clean the surface.

Most materials (with the significant exception of carbon) on the surface of tungsten will thermally desorb from the surface upon annealing to 2600K. Thus, before film deposition, the crystal is heated to 2600K for about 10 seconds in a process known colloquially as "flashing". After cooling, the crystal is checked for the presence of any carbon atoms using AES. Carbon is a natural contaminant in bulk tungsten and can come to the surface upon heating.

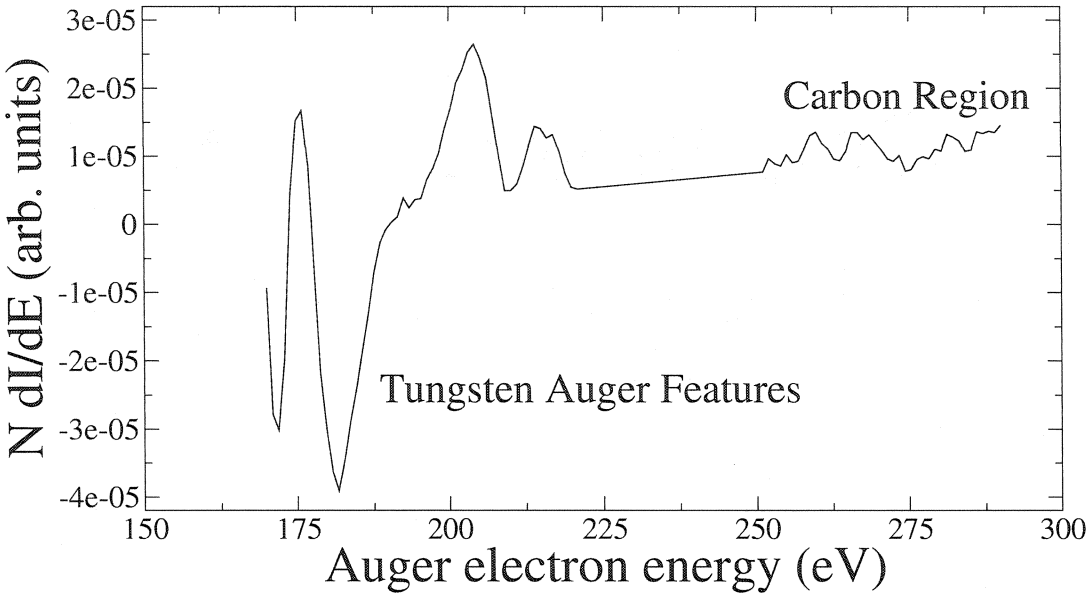

Figure 3.6: Auger spectrum showing tungsten and carbon Auger features.

Figure 3.6 shows an Auger spectrum taken to show the tungsten Auger peaks (170-220eV) and to to compare their amplitude against the carbon peak at 274eV. The figure shows that there is a small carbon peak just above the level of noise in the spectrum.

To clean the carbon from the surface, the crystal is annealed in the presence of oxygen for one minute. An oxygen partial pressure of between 10^{-7} and 10^{-6}torr is used, depending on the amount of carbon detected. Heating the surface with oxygen causes the carbon to form carbon monoxide, which easily desorbs from the surface on flashing. This process is repeated until no evidence of carbon is detectable. The residual oxygen (itself relatively stable on tungsten) is removed by a standard flash into vacuum.

The size of the Auger peak in the differential spectrum can tell us how much material is present and to some extent whether the material on the surface is wetting the surface. The following section will detail how these calibrations are done and how

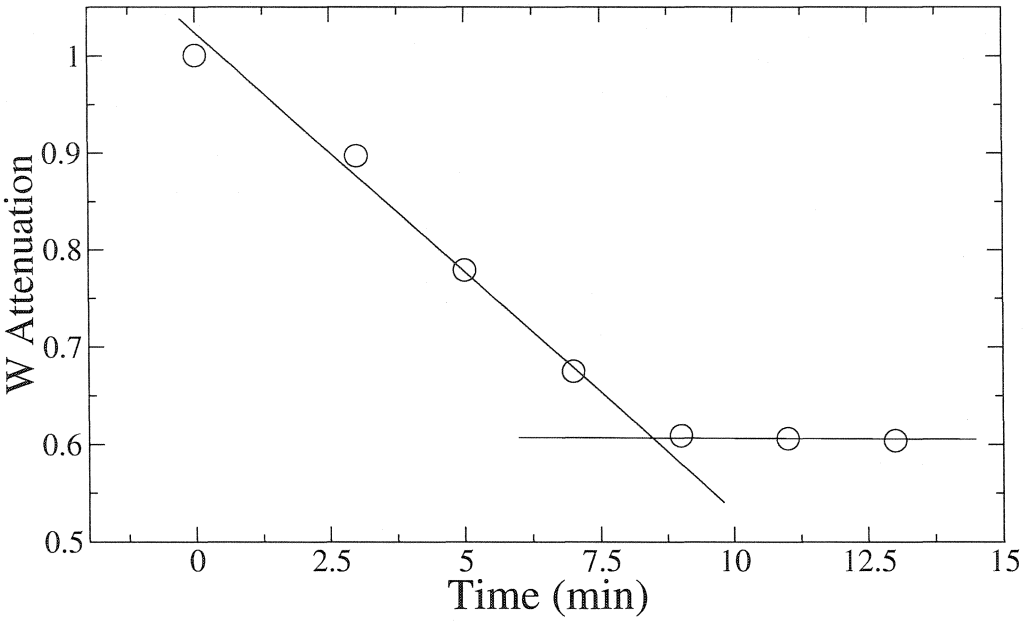

Figure 3.7: Attenuation of clean W auger signal as a function of deposition time of iron material. Clear breakpoint is shown at approximately 8.5min.

wetting can be inferred from the data.

3.4.4 Thickness Calibration

For a film that grows layer by layer, thickness calibration is possible using AES. As long as the material being deposited goes down a layer at a time, the increase in the size of the Auger signal for the film material (or the attenuation of the Auger signal from the substrate) will change linearly with coverage. Linear behaviour will continue past the completion of the first monolayer but at a different slope. Looking at where the slope changes tells you when the first monolayer is completed. If the material was being deposited in a less-regular fashion, the Auger signal would act more as an exponential as a function of time. It is by looking at the linearity of the signal versus exponential behaviour that allows some conclusions to be drawn about the film growth mode. The Auger signal for layer-by-layer growth (also called Franck-Van der

Merwe or simply FV growth) changes as a function of coverage as:

$$S(x) = \sum_i S_i(1 - x_i) + S_{i+1}(x_{i+1}) \tag{3.2}$$

where S_i is the Auger signal from areas of the substrate that have been covered with i layers of film material and x_i is the occupancy of the atoms in the ith layer. The S factors include the exponential factor due to the shielding effect they have on the probability of electrons being emitted from the surface.

It is easy to see that a change in slope will occur as a function of x once the second layer starts to fill in. This is shown clearly in figure 3.7 where the Auger signal from the tungsten substrate is plotted as a function of the deposition time of iron. The rate of iron deposition was held constant by use of the flux monitor on the evaporator. The depositions in this case were annealed to high temperature after each step so as to accentuate the change in slope, as the second monolayer is not thermally stable at temperatures above 600K.

The methods outlined here only describe the uses of Auger spectroscopy used in this thesis. There are several other ways in which Auger events can be used in surface science. AES can be employed to perform research on film structure by employing an angle-resolved technique. This experiment relies upon the fact that there is some preferred direction for Auger electrons that are emitted from atoms below the first layer. The directionality is due to a mild "focusing" effect of the electrons as they pass by the positively charged nuclei. There is also the technique of scanning Auger microscopy (SAM). This uses a small Auger electron detector that travels across the surface of a sample and maps the chemical composition as a function of position.

3.5 Structure Measurements using Low Energy Electron Spectroscopy

Low energy electron diffraction (LEED) is a powerful technique used for studies of surface crystallography. Elastically backscattered electrons at low energy (~50-500eV) show a reciprocal space picture of the atoms at the surface, allowing the interested researcher to get information on lattice spacing, surface strain, and the degree to which the surface atoms are ordered. Used mainly as a qualitative tool in the research of this thesis, it can be used to extract quantitative data as well.

The basics of LEED are the same as for most diffraction techniques used in condensed matter physics. An incident probe of electrons that have a deBroglie wavelength on the order of the lattice spacing (Angstroms) will diffract in the lattice of atoms. An electron with a kinetic energy of 150eV has a wavelength of about $1\mathring{A}$. This energy also corresponds to the minimum in the mean free path of electrons in metals as shown by the universal curve. According to the curve, a 150eV electron has a mean free path of about $6\mathring{A}$. This makes the low energy electron an ideal surface probe as only electrons that diffract within $6\mathring{A}$ of the surface will be detected.

In the LEED system used for this thesis, the geometry of the set-up is in the back-scattering mode. This means that all incident electrons have a momentum $\mathbf{k}_i$ perpendicular to the surface. Surface diffraction requires the scattered electrons to have a component of the momentum in the plane parallel to the surface. To conserve the momentum, this means that the parallel component of the momentum of the diffracted electron must be the negative of the reciprocal lattice vector of the surface $\mathbf{G}$. The conservation of momentum equations will go as:

$$k_i = G + k_f \tag{3.3}$$

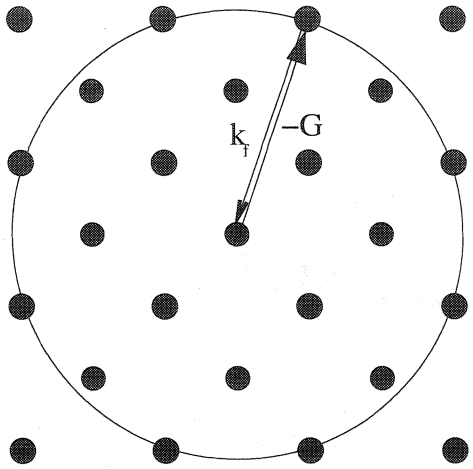

Figure 3.8: This figure represents a recipocal lattice. All points within the circle represent possible scattering centers. $\mathbf{k}_f$ is the parallel component of the the scattered electron and $\mathbf{G}$ is a reciprocal lattice vector.

where $\mathbf{G}$ is of course is entirely parallel to the surface and $\mathbf{k}_f$ has both parallel and perpendicular components. The diffraction condition is shown in fig. 3.8. The possible range of diffraction centers is contained within a circle that is defined by the energy of the incident electron. Any reciprocal lattice point within the circle will satisfy the diffraction condition as long as $-\mathbf{k}_{f,}=\mathbf{G}$.

3.5.1 Measurement Technique

A LEED diffraction pattern in usually measured in a back-scattering geometry. The surface to be examined is positioned normal to a high-efficiency electron gun. The electrons that scatter from the surface atoms then travel through two retarding grids that only allow elastically scattered electrons to pass. These electrons are then accelerated into a phosphor screen that can be observed through a window in the UHV system, allowing real-time observation of the diffraction pattern.

With the use of a CCD device, the intensity and the profile of the LEED spots can be recorded. For the LEED pictures used in this thesis, a new 640x480

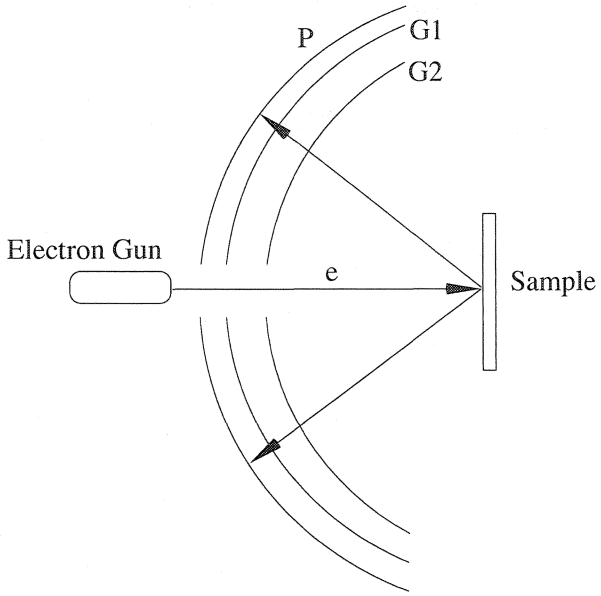

Figure 3.9: Simple schematic of LEED experiment. P is the phosphor screen. G1 and G2 are the retarding grids.

CCD digital camera was used. The camera was capable of recording black and white images with 10-bit resolution (1048 levels). The resulting image is passed into a computer with a high-quality image acquisition board. The data is stored as an 640x480 array of intensity values.

As LEED spots will sometime be quite faint against the background light noise, very good signal-to-noise is required when recording the images. It was discovered soon after the camera system and software was implemented that there was a horizontal noise pattern in the recorded images. The horizontal regions of noise were seen to travel from the bottom to the top of the image while observing the screen in video mode.

A very simple yet powerful filtering algorithm (sometimes used in astronomy for image filtering[46]) was implemented to reduce and eliminate this horizontal noise. The LEED screen is framed to the right of the viewable rectangle of the camera image.

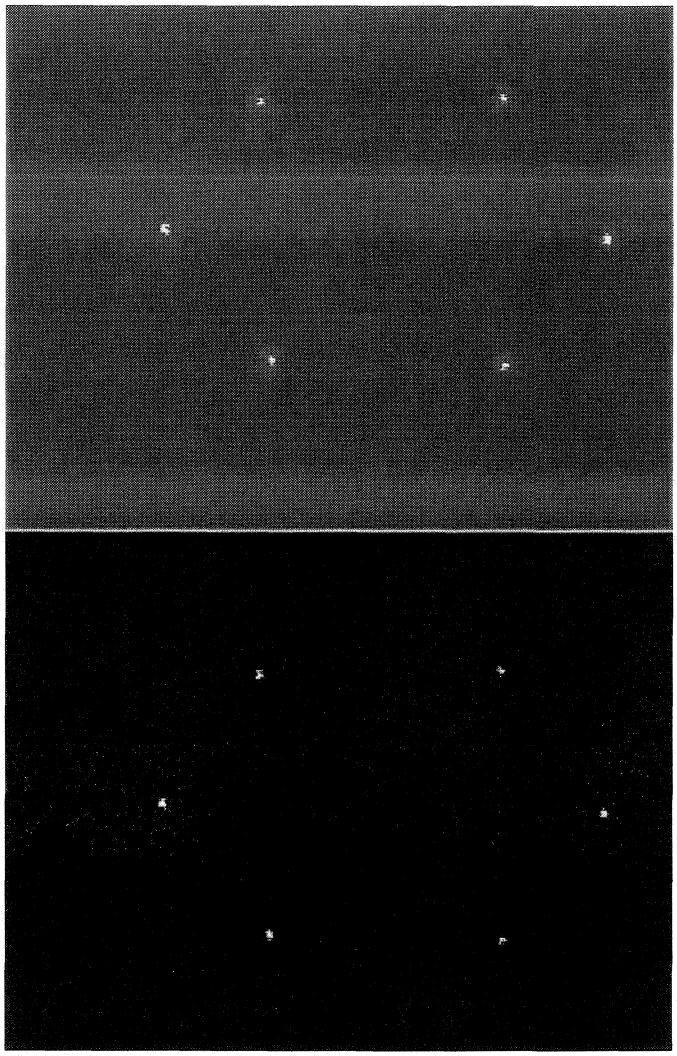

Figure 3.10: LEED picture of clean W(110) surface taken at 120eV. The top image in the unfiltered data while the bottom is the same photo processed with a filter-width of ten pixels.

To the left of the frame, a darkened area was formed with black electrical tape. All ambient light sources (including the ion gauge which measures the pressure inside the chamber) were extinguished and the camera and the observing window were covered by an opaque black shroud. The image was then recorded and stored to computer. For each row of pixels in the image, the filter averages the intensity to a specified

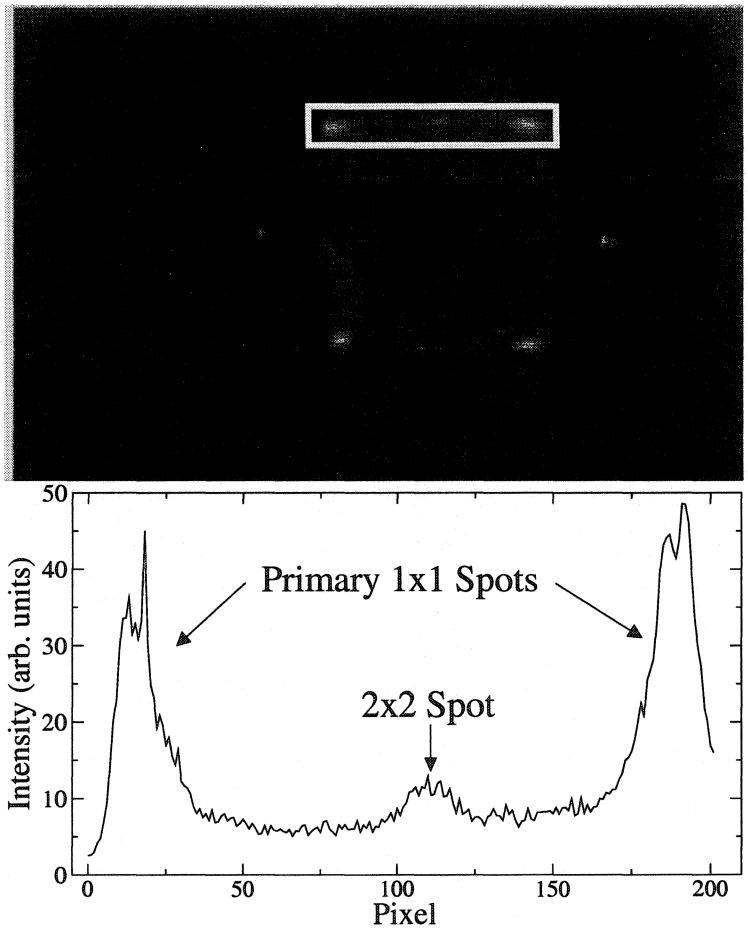

Figure 3.11: LEED image from a poorly grown iron film. The box in the top section shows the region of the image that comprises the intensity data shown below.

width starting at the left edge of the image for each row of pixels. The filter then subtracts that average from the entire span of the image. It was seen that only a small width needed to be averaged over to achieve the desired results. Figure 3.10 shows before and after pictures of a LEED pattern measured from a clean W(110) surface. The filtered image used an averaging width of only 10 pixels.

The recorded images can also be used to measure the diffracted spot intensity and half-width of the peaks. This can be especially useful when trying to find faint spots in the image. Figure 3.11 shows a LEED image from a poorly grown iron film.

Oxygen contamination of the film will cause faint extra diffraction spots to appear in the LEED image. These types of features are often faint and can be difficult to discern with the eye but they will show up clearly in the intensity profile.

3.5.2 Interpretation of Diffraction Images

A LEED diffraction experiment measured by the method described provides a real-time image of the reciprocal lattice. One of its main uses in surface science is to determine the coordination of the film atoms with respect to the underlying lattice. While interpretation can become quite difficult when glide planes and rotations need inclusion, this thesis only deals with systems with centered structures and as such will be the sole topic here.

A film which grows pseudomorphically on the substrate lattice will have a LEED pattern unchanged from the pattern seen on the clean surface. This is because the atoms of the film have arranged themselves so as to not change the diffraction conditions at the surface. This reasoning ignores factors associated with how well certain atoms will act as scattering centers, but such a consideration should only affect the intensity of the diffraction point and not the geometry.

A common nomenclature used for labelling film symmetries uses the length of the film's unit cell in units of the primitive unit cell of the substrate. So, a film that has a unit cell that is two times the size of the unit cell of the substrate is said to have a 2x2 pattern (this assumes a cubic symmetry). For instance, oxygen will form a 2x2 pattern on W(110) once the oxygen coverage on the film exceeds about two-thirds of the surface[47]. Nickel monolayers on W(110) forms a highly strained 7x1 pattern[48]. This means that along one direction of the film, the unit cell of the film is only commensurate with the substrate on the order of seven unit cells of the substrate, but is fully commensurate along the other direction. Examples of both of

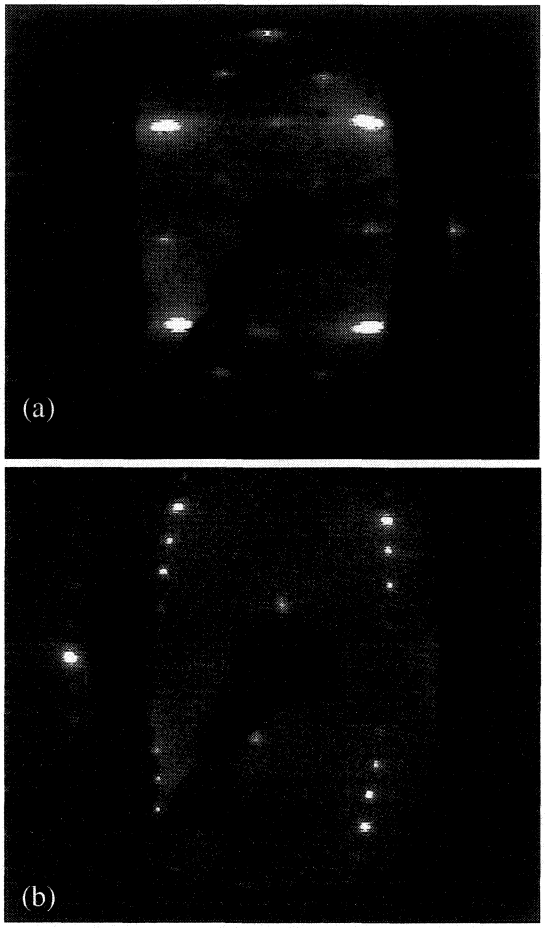

Figure 3.12: Diffraction images of (a) 2x2 oxygen and (b) a 7x1 nickel monolayer on W(110) surface. (Nickel image courtesy of Q. Li.)

these diffraction patterns are shown in figure 3.12.

3.6 Magnetic Measurements using Surface Magneto-optic Kerr Effect

Magnetic measurements that use the *surface Magneto-optic Kerr Effect* (SMOKE) are perhaps the most commonly used in surface magnetometry. Using experimental methods from ellipsometry and taking advantage of the fact that cheap, high-quality HeNe lasers have a wavelength on the order of the typical energy spacing of the 3d

electron bands, SMOKE is capable to measuring robust magnetic signals from the smallest samples.

The following subsections will attempt to highlight that concepts behind SMOKE from the point of view of optics and quantum mechanics. More technical details on how the measurements are made in the laboratory will follow.

3.6.1 SMOKE via Optics

The Kerr effect is related to its much better known cousin, the Faraday effect. The Faraday effect is the rotation of the polarisation of the incident light as it is transmitted through a magnetic medium. The Kerr effect is simply this same effect but as it applies to reflected light.

A simple optical explanation behind the Kerr effects is as follows. Linearly s or p (s and p designations refer to the orientation of the polarisation axis to the scattering plane) polarised laser light will reflect from a metal surface with the same polarisation it possessed on incidence. This assumes that the metal surface is isotropic or in more technical terms, that the reflection matrix in Jones notation has only diagonal components as follows:

$$\begin{pmatrix} r_{ss} & r_{sp} \\ r_{ps} & r_{pp} \end{pmatrix} = \begin{pmatrix} r_{ss} & 0 \\ 0 & r_{pp} \end{pmatrix} \tag{3.4}$$

The off-diagonal components take on non-zero values when the symmetry of the metal is reduced, as it is in magnetic materials. The elements of the reflection matrix can be calculated using the dielectric tensor of the material. A diagonal dielectric tensor will give rise to a diagonal reflection matrix. For a magnetic metal, the dielectric tensor can be written as:

$$\epsilon_d = \epsilon_d \begin{pmatrix} 1 & iQ & 0 \\ -iQ & 1 & 0 \\ 0 & 0 & 1 \end{pmatrix} \tag{3.5}$$

where ϵ_d is the dielectric constant (the subscript d is used here only to differentiate this constant from the reduced temperature which is also symbolised by ϵ) and Q is the magneto-optic Voigt parameter, which introduces the change in the polarisation. The size of Q depends on the size of the average magnetic moment of the surface and sets the degree to which the polarisation axis is rotated and how much ellipticity is introduced.

This dielectric tensor will lead to eigenvectors of the reflected light with different values based on whether the incident light is left or right circularly polarised. As such, a small rotation of the polarisation is introduced in the reflected light (linearly polarised on incidence), the size of which is dependent on the size of the magnetic moment at the surface. This measurement technique is sensitive to all magnetic moments within the skin-depth of the light (on the order of the laser wavelength).

The macroscopic formulae for the Kerr effect rotation in ultrathin films are dependent upon Q, the layer thickness d, N (the refractive index of the material), the incident angle of the light θ, and λ (the wavelength of the incident light). These formulae apply as long as the ultrathin condition is satisfied[49] as follows:

$$\frac{2\pi}{\lambda}|N|d \ll 1 \tag{3.6}$$

The Kerr rotation for longitudinal (in-plane) and polar (out-of-plane) moments is then given as follows[49]:

$$\phi^{POL} = -cos(\theta)\left(\frac{4\pi}{\lambda}\right)\left(\frac{N^2}{1-N_{sub}^2}\right)Qd \tag{3.7}$$

$$\phi^{LON} = sin(\theta)\left(\frac{4\pi}{\lambda}\right)\left(\frac{N_{sub}}{1-N_{sub}^2}\right)Qd \tag{3.8}$$

where the angular dependence arises from the requirement that there must be some component of the magnetisation vector coincident with the propagating vector of the

incident light. At 45^o incidence, the only difference between the two effects is in the difference between the square of the refractive index of the film N and the unsquared index of the substrate N_{sub}. For typical values of N, this means that the polar effect is a more sensitive measurement than the longitudinal.

3.6.2 SMOKE via Quantum Mechanics

SMOKE is inherently a quantum mechanical effect. As long as the wavelength of the laser light used as a probe is on par with the relevant energy spacing between the bands of the itinerant electrons, the Kerr effect should be observable.

The effect in 3d transition metals can be understood at a fundamental level by looking at transitions induced by the incident light of electrons from the 3d band to the 4s (see diagram in Figure 3.13). The 3d electron bands are spin degenerate in the absence of a magnetic field. Dipole selection rules state that electrons can only transit between two states if the change in the orbital angular momentum number (l) is ± 1 and the change in m_l is +1 for right polarised photons and -1 for left polarised photons.

In the presence of a magnetic field due to the inherent magnetic moments, there will be a lifting of the 3d electron degeneracy due to the Zeeman effect. The Zeeman effect will decrease the spin-up 3d level and vice-versa. This will give rise to a different transition probability for left and right circularly polarised photons. It is this difference that will give rise to small changes in the polarisation of the reflected light.

3.6.3 Measurement Techniques

The Kerr effect is most commonly exploited in two ways for the purpose of magnetometry. A dc technique can be used to measure magnetic hysteresis while an ac

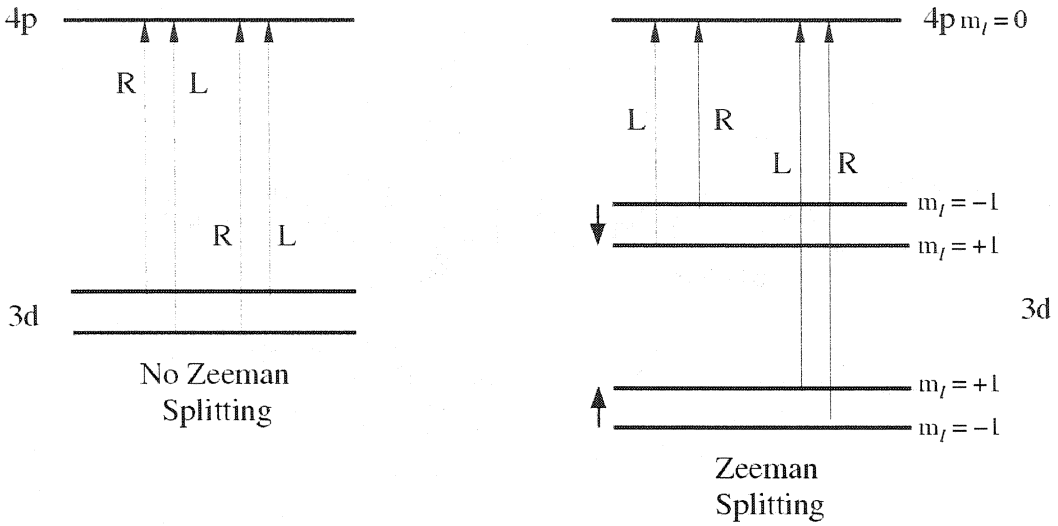

Figure 3.13: Level splitting leads to a broken symmetry between the transition probability for left and right polarised photons.

technique can be used to explore the magnetic susceptibility. This subsection will detail how each of these are used in the McMaster laboratory.

-

SMOKE TECHNIQUE 1 - *dc Measurement of Magnetic Hysteresis*

Once the a magnetic surface has been prepared, laser light is made incident upon the magnetic surface at an angle of 45^o. This is not an ideal angle for in-plane measurements as SMOKE is sensitive to only the magnetic moments that have a component that is parallel to the incident light (Kerr $\propto$ k·M). The 45^o was chosen for two main reasons. One is simply a question of chamber geometry which makes other angles difficult. The other reason is that the apparatus is routinely used for the study of both in-plane and perpendicularly magnetised films.

The light is sent through a lens and mirror system that first expands the beam out of the laser and then redirects and focuses it onto the film. The expansion

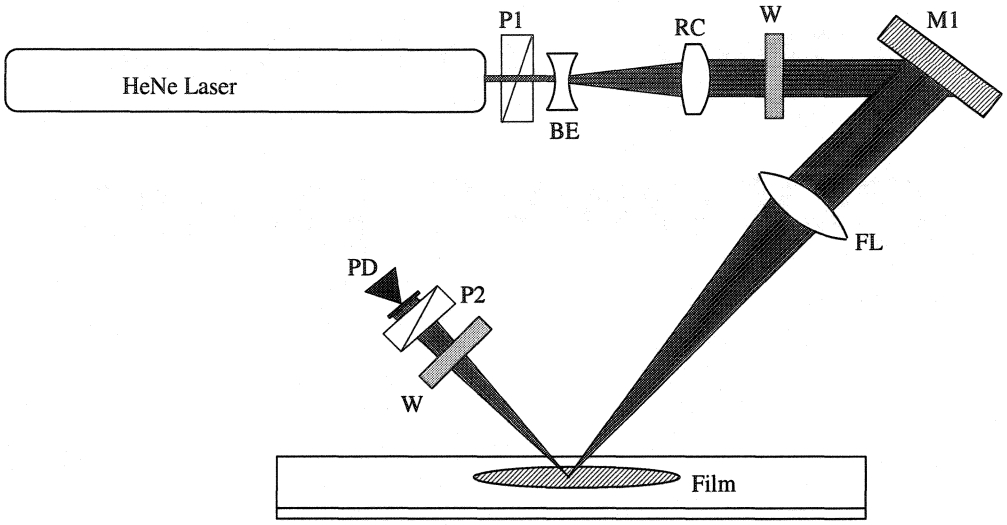

Figure 3.14: Level splitting leads to a broken symmetry between the transition probability for left and right polarised photons. Labelled components are as follows: P1 - initial polariser, BE - beam expander, RC - recollimator, M1 - mirror, FL - focusing lens, P2 - analysing polariser, PD - photodiode, W - window.

allows for a slight reduction in the size of the beam spot on the film. Figure 3.14 shows an outline of the optics used. The minimum beam spot obtained was 0.75mm diameter.

The incident light is linearly polarised using a commercial Glan-Thomson polariser which is mounted on a rotational stage. The reflected light passes through a second GT polariser that is set to almost right-angle to the initial polariser. The light then passes into a photo-diode where the intensity of the light is measured. The light intensity is related to the rotation of the polarisation by:

$$I(\theta) = I_{mx}[sin^2(\theta) + \epsilon_r] \tag{3.9}$$

where θ is the angle between the crossed polarisers (zeroed at $\pi/2$), I_{mx} is the maximum intensity, and ϵ_r is the *extinction ratio* of the polarisers. The extinction ratio is a measure of the intensity of light that will pass through two polarisers that are crossed at exactly ninety degrees and is an indicator of the quality of the polarisers.

The GT polarisers used in this measurement typically give a value of ϵ_r on the order of 10^{-7}.

To achieve this good a value for ϵ_r, it is necessary to account for unwanted contributions to changes in the polarisation due to the effects of the light being transmitted through UHV windows. These windows are generally composed of quartz which will become birefringent (meaning that the material has a different index of refraction depending on the polarisation of the light) when put under stress. Since the quartz is held in a stainless steel ring which is bolted tightly to the main UHV chamber, such stresses will unavoidably be introduced. As well, further strains will occur during the repeated bake-out procedure described earlier to achieve low vacuum conditions. It was found[50] that the ellipticity introduced by the windows could in fact be exploited to improve the signal-to-noise of the measurements and removes the need for a quarter-wave plate that is often used in ellipsometry measurements.

Before any SMOKE measurements can be made, the intensity of the s-polarised laser light transmitted through the second polariser is minimized by rotating the polariser until it is 90^o to the initial polarisation. This intensity is not the minimum achievable, however, due to the ellipticity introduced at the windows and the reflecting surface. It's been found that by rotating the initial polariser such that the incoming polarisation is slightly away from s-polarisation, the ellipticities can be negated, leaving only rotations in the polarisations as a function of applied magnetic field to be measured.

Once the polarisers are arranged to negate the window contributions to the polarisation, the angle between the polarisers needs to be set to maximise the contrast of the dc signal. We can write the contrast, C, as:

$$C = \frac{\delta I}{I} = \frac{2\theta\Delta\theta}{\theta^2 + \epsilon_r} \tag{3.10}$$

A simple differentiation shows that this is maximized at $\theta = \sqrt{\epsilon_r}$. It is easy to see from eq.(3.9) that when the rotation angle of the polariser is set to ϵ_r, this will double the extinction intensity of the light to the detector. So for maximum contrast, the second polariser is rotated so as to double the intensity of light that is recorded as extinction.

The intensity is measured as a function of the applied magnetic field. The field in our apparatus can be applied either perpendicular to the plane of the film or in-plane along one direction by passing current through Helmholtz coils attached to the sample holder. The size of the field is limited to the amount of current that can pass through the coils without heating the wire enough to cause the insulating varnish on the wire to melt and contaminate the entire chamber.

Figure 3.15 shows a typical hysteresis measurement taken from a 1.4ML Fe/W(110) film at a temperature of approximately 270K. The field was ramped slowly between -60 and 60 Oe multiple times and the value of M for each branch of the loop is averaged from the multiple field cycling.

-

SMOKE TECHNIQUE 2 - *ac-SUSCEPTIBILITY*

The susceptibility measurement uses the same optical setup as the hysteresis measurement. The magnetic susceptibility (χ_m) is measured by applying a sinusoidally varying magnetic field to the film. The intensity at the photo-diode is measured now by a lock-in amplifier, which measured the intensity only at the frequency of the applied field. The digital lock-in used is capable of measuring two phases of the oscillatory response of the magnetism, allowing for simultaneous measurement of both the real and the imaginary components of the complex susceptibility.

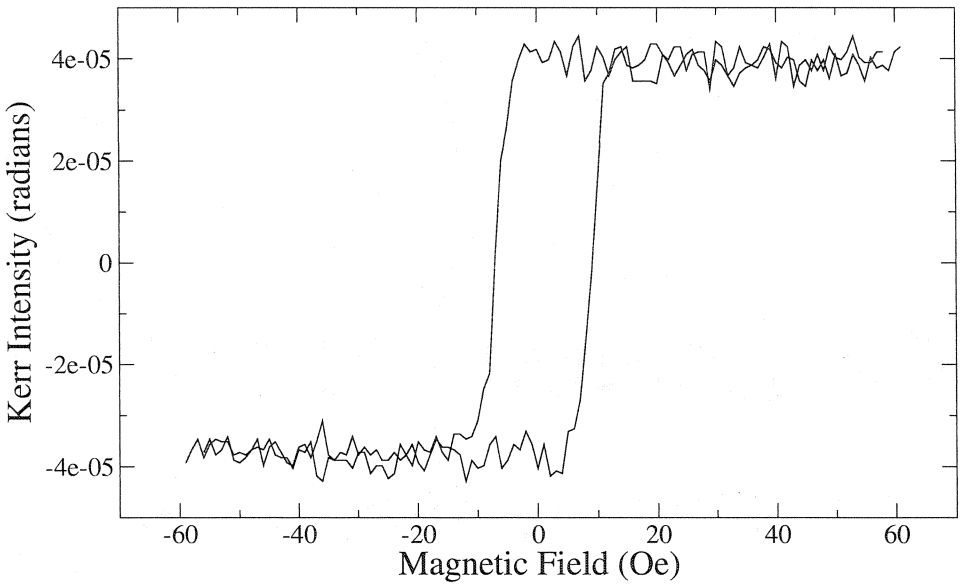

Figure 3.15: Magnetic hysteresis loop measured using the surface magneto-optic Kerr effect from a 1.45ML Fe film at 270K. Magnetisation is plotted in units of radians of Kerr rotation.

The angle of the analyzing polariser is set to a different value in the ac measurement than in the dc hysteresis. This is due to more complicated frequency-dependent signal-to-noise issues that arise in the ac technique. A complete treatment of the S/N as a function of set angle for a susceptibility measurement is given in reference[17]. It was found in that study that a set angle of 10 arc-minutes for our equipment maximized the signal-to-noise.

The signal is calibrated from small photo-diode voltages to radians using the first derivative of eq.(3.9):

$$\Delta\theta = \frac{\Delta I}{2\theta I_{mx}} \tag{3.11}$$

where ΔI is the ac voltage measured from the photodiode and $\Delta\theta$ is the rotation angle of the polarisation. This is approximately converted to SI units of susceptibility by the following equation:

$$\chi = \left(\frac{4\pi}{1000}\right) \frac{\Delta\theta M_{Fe}}{H_{app}\Theta_{Kerr}t} \tag{3.12}$$

where M_{Fe} is the saturated moment value for bulk iron in cgs units, H_{app} is the applied field in Oersteds, Θ_{Kerr} is the Kerr rotation that results from a single monolayer of magnetic material of unit moment, and t is the thickness in monolayers. Θ_{Kerr} has a value of 250×10^{-6} for iron. The prefactor of $\frac{4\pi}{1000}$ is to convert between cgs and SI units.

The final parameter for the calibration of the susceptibility is the set phase angle of the dual-phase lock-in amplifier used to record the complex signal. There are phase lags between the output oscillator of the lock-in and the final detection of quadrature components x and y. It is important for the phase angle to be correct to properly rotate x and y into the real (in-phase) and imaginary ($\frac{\pi}{2}$ out-of-phase) signals. The phase angle ρ enters the calibration via a simple rotation matrix:

$$\begin{pmatrix} \cos(\rho) & -\sin(\rho) \\ \sin(\rho) & \cos(\rho) \end{pmatrix} \begin{pmatrix} x \\ y \end{pmatrix} = \begin{pmatrix} Re(\chi) \\ Im(\chi) \end{pmatrix} \tag{3.13}$$

ρ is dependent on all of the experimental apparatus used. There are phase differences to be considered in the power amplifier that amplifies the oscillator signal from the lock-in into current used to drive the magnetic field in the Helmholtz coils. This phase difference is frequency dependent and was measured carefully by examining the input and output waveforms on an oscilloscope. The trend as a function of frequency is then extracted from the plotted phase differences. The coils themselves have a natural resistance (R = 5.2Ω) and inductance (L = 5.7μH), creating another frequency phase difference of $\omega L/R$. The final contribution to the phase angle comes from the amplifier in the amplifier of the photodiode detector. It has a natural time lag due to RC nature of the inverting amplifier used (R= 100MΩ, C= 1.7pF for the 10^8 gain scale used in all the susceptibility measurements in this thesis). Each of these effects has been painstakingly quantized to account for phase differences for a given value of the frequency. For this thesis, almost all data was

taken at either 150 or 400Hz although there were some at other frequencies, all less than a kiloHertz. For these values of the frequency, the phase angle ρ is 220.75 and 77.80 degrees respectively.

Chapter 4

Results

4.1 Measurement of the Static Critical Exponent of the Magnetic Susceptibility γ

The following section contains a paper that was recently submitted to the journal Physical Review B. The authors list is M.J. Dunlavy and D. Venus. To maintain consistency with the text of the complete thesis, references and labelling of citations, figures, equation, and tables have been modified from the original draft. Otherwise, no changes have been made from the submitted manuscript. The seven figures associated with the paper are located at the end of the section.

As of this writing, the manuscript has been resubmitted to the editors to address a small concern of the referee. It is expected to be accepted soon.

Critical Susceptibility Exponent Measured from Fe/W(110) Bilayers

M.J. Dunlavy, D. Venus

Dept. of Physics and Astronomy, McMaster University, 1280 Main St. West,

Hamilton Ontario, Canada

Abstract

The critical phase transition in ferromagnetic ultrathin Fe/W(110) films has been studied using the magnetic ac susceptibility. A statistically objective, unconstrained fitting of the susceptibility is used to extract values for the critical exponent γ, the critical temperature T_c, the critical amplitude χ_o and the range of temperature that exhibits power-law behaviour from individual experimental measurements of $\chi(T)$. This avoids systematic errors and generates objective fitting results. An ensemble of 25 measurements on many different films are analyzed. Those which permit a fitting range in reduced temperature extending lower than approximately 4.75×10^{-3} give an average value γ=1.76 $\pm$0.01. Bilayer films give a weighted average value of $\gamma = 1.75 \pm 0.02$. These results are in agreement with the 2-dimensional Ising exponent $\gamma = \frac{7}{4}$. Measurements that do not exhibit power-law scaling as close to T_c (especially films of thickness 1.75ML) show a value of γ higher than the Ising value. Several possibilities are considered to account for this behaviour.

Introduction

Experiments that seek to measure critical phase transitions are very important to physics at a fundamental level. Careful experiments can be used to test the theoretical models of universality and scaling. The true nature of the order parameter of a system, both in terms of dimensionality and degrees of freedom, is revealed at the transition and important physical insight is gained in the looking.

An ultrathin magnetic film closely approaches the physical realization of a truly two dimensional magnetic system, and offers a better system for studying critical phase transitions in two dimensions than more traditional layered bulk materials such as Rb_2CoF_4 [25], where interlayer interactions will always be present, even if only to a small degree. Bander and Mills [23] have shown that when ferromagnetic thin films have uniaxial anisotropy, the critical regime near the Curie temperature is described by the 2 dimensional Ising model. For this reason, a great number of measurements of the static critical exponents of ultrathin ferromagnetic films have been reported. Almost all of this experimental work concentrates on the critical exponent of the magnetization, β [15, 10, 9, 4, 11, 7, 16, 12]. To our knowledge, there are only a handful of reports in which the critical exponent of the magnetic susceptibility, γ, is investigated experimentally for an ultrathin magnetic film [51, 15, 16, 17, 18, 14]. Unfortunately, almost all of these susceptibility studies have at least one of a number of deficiencies which call the results into question.

A common difficulty in the determination of critical exponents is the determination of T_c. Small variations in the assumed value of T_c have a profound effect on the fitted value of the critical exponent, and introduce confidence limits that are usually much larger than those derived from a simple two parameter fit for the critical exponent and amplitude. The extreme sensitivity of the results to T_c implies that the same data must be used to determine both T_c and the critical parameters. This is particularly true for metastable ultrathin films, since very small shifts in the critical temperature are often introduced by temperature cycling and annealing, or by residual vacuum contamination. A second difficulty is determining the temperature range where scaling is observed. Since real, finite systems do not show infinite divergences, the order parameter departs from power law behaviour close to T_c because of finite

size effects, dynamical effects (in ac measurements), a finite demagnetization factor, and so on. To fit the data properly, an objective, four parameter power-law fit of the data is required. In addition to T_c and γ, the fit should find values for the critical amplitude χ_o and the cutoff for power-law behaviour near T_c. Finally, in order to demonstrate true systematic behaviour, it is clear that the analysis of many films and measurements is necessary.

It is perhaps surprising that after two decades of investigating the critical properties of ultrathin ferromagnetic films, that no published measurements of γ meet these criteria. An impressive study by Back et al. [9] on Fe/W(110) ultrathin films determines β and the exponent of the critical isotherm δ using the dc magnetization, and then derives γ using the scaling relations between different exponents. The value of T_c is not fit, but rather taken to lie at the peak of the dc susceptibility for a particular experiment. The results agree with the predictions of the 2d Ising model. This represents a check of the internal consistency of the data and scaling relations, but is not an independent measurement of γ. Elmers et al. [15] report dc susceptibility results for a series of submonolayer films of Fe/W(110) and find $\gamma = 2.8 \pm 0.2$, significantly different than the 2d Ising value of 1.75 [42]. It is not clear to what extent this finding is a result of using an incomplete film layer or if, as they suggest, the material is exhibiting the behaviour of an anisotropic Heisenberg system. Other studies report results only for a single measurement from a single film [17]. Still others use questionable criteria for determining T_c, such as the disappearance of the imaginary component of the susceptibility in an ac measurement [18], the peak of the real ac susceptibility [14, 52], or the presence of a "shoulder" above the peak of the susceptibility [51] under special circumstances.

This paper presents the results of a collection of 25 measurements of the

ac magnetic susceptibility of Fe films between 1.5 and 2.0ML grown epitaxially on W(110), and the values of γ derived from them using an objective minimization of the statistical variance between the data and a power law fit using four parameters: T_c, γ, the amplitude χ_0, and the low reduced-temperature cutoff t_x for fitting. Error estimates on T_c and γ are provided by 1σ variations in the statistical χ^2. The results fall into two distinct classes. Measurements exhibiting power law behaviour over a long range of reduced temperature extending down to a cutoff $t_x < 4.75 \times 10^{-3}$ give an average critical exponent $\gamma = 1.76 \pm 0.01$. Measurements which exhibit power law behaviour down to larger values of t_x show a systematic trend to higher values of γ which depends rather linearly on $\ln(t_x)$. The possibility that films which give a high value of γ have a distribution of transition temperatures will be addressed to explain this unexpected result.

Theory

According to scaling theory, the real component of the intrinsic magnetic susceptibility ($\chi_{int} = \partial M/\partial H$) above the Curie temperature of a critical phase transition is described by the power-law equation:

$$\chi'_{int}(t) = \chi_o t^{-\gamma} \tag{4.1}$$

where χ_o is the critical amplitude, γ is the static critical exponent for the susceptibility of the order parameter and t is the reduced temperature above T_c, given as:

$$t = (\frac{T - T_c}{T_c}). \tag{4.2}$$

For experimental measurements of the magnetic ac susceptibility, additional terms need to be added to account for both demagnetization and dynamical effects.

The demagnetizing factor N is folded into the expression for the intrinsic susceptibility by augmenting the magnetic field by:

$$H_{eff} = H - NM \tag{4.3}$$

where H_{eff} is the effective field acting on the ferromagnet. This gives rise to an effective susceptibility of:

$$\chi'_{eff}(T) = \frac{\chi'_{int}(T)}{1 + N\chi'_{int}(T)}. \tag{4.4}$$

It is easy to see that for a non-zero value of N, the susceptibility cannot diverge at T_c. N will "dampen" any experimental measurement of χ as long as the value of the product $N\chi_{int}$ is comparable to or greater than one.

To accurately describe results from ac susceptibility, it is necessary to add the effect of the relaxation time of the magnetization to the effective susceptibility. In the linear response approximation, for systems with an exponential relaxation time (τ) [$M(\mathcal{T}) \propto \exp(-\mathcal{T}/\tau)$] where $\mathcal{T}$ is time. Under the influence of an externally applied sinusoidal field, the real dynamic susceptibility (χ') can be written as:

$$\chi'(T) = \frac{\chi'_{eff}(T)}{1 + (\omega\tau(T))^2} \tag{4.5}$$

where ω is the driving frequency of the magnetic field [1]. This final form of the magnetic susceptibility limits the ability of experiments to probe critical behaviour very close to the transition. To observe any critical scaling in the experimental data, two requirements must be met: we must have N sufficiently small and we must have $(\omega\tau)^2 << 1.0$.

The extreme aspect ratio of ultrathin films leads to very small values of N. For systems that have their moments oriented in-plane, N is proportional to first

[1] In these equations, the relaxation time of the magnetization is used, where $\frac{dM}{dt} = -\frac{1}{\tau}(M - M_\infty)$. Dissipation can also be expressed in terms of the relaxation of the effective field using the Landau-Liftshitz equation and the damping parameter λ. The two terms are related by $\tau = \frac{\chi_{eff}}{\lambda}$.

order to the thickness divided by the effective lateral dimension of the film [21]. For films that are one or two atomic layers thick and many thousands of lattice spacings wide, N will be extremely small. This is another reason why ultrathin films are ideal for studies of critical phenomenon in two dimensions. Previous studies of the susceptibility on ultrathin films have attempted to estimate N (and include the estimation in the power-law fits) by using the maximum value of the real susceptibility [18]. The argument proceeds by rearranging eq.(4.4) as follows:

$$\frac{1}{\chi_{eff}(T)} = \frac{1}{\chi_{int}(T)} + N \tag{4.6}$$

This leads one to the conclusion that at T_c, when χ_{int} is infinite, $N = 1/\chi_{max}$. This simple treatment has several problems even for dc susceptibility measurements (where $\omega = 0$) in that it ignores other effects (finite field, saturated correlation length, etc.) that will saturate the susceptibility and will give a value for N that is artificially too high and is at best an upper limit [53]. If this limit of N is then used in the power-law analysis, the resulting quoted values for γ should be called into question.

Dynamic effects are only significant near T_c where critical slowing down will lead to a large relaxation time for the equilibration of the order parameter[43]. This can be less of a problem in dc measurements, but the increased signal-to-noise that is achieved in ac measurements make it worthwhile to deal with the dynamics problem. In fact, critical slowing effects should disappear once the temperature is increased more than a degree or two above T_c. Dynamic effects will change the temperature at which the susceptibility exhibits a maximum (depending on the measurement frequency used), making the evaluation of T_c by that method difficult if not impossible.

Experiment

Fe/W(110) ultrathin films with high quality epitaxial layers can be grown at

least up to 2 ML [54]. Previous studies of Fe/W(110) have shown that the magnetic properties of the films depend sensitively on the film thickness [55]. Some studies of films less than 1.5ML show an interesting perpendicular magnetisation due to the film structure which results from step-flow growth [56, 57]. Pietzsch *et al* [58] find perpendicular domains for narrow bilayer stripes on a Fe monolayer at low temperatures (about 16K) grown on a miscut surface. For this study, we concentrate on the thickness range from 1.5 to 2.0 ML, where many studies have confirmed a large in-plane anisotropy for this system.

The experiments were performed in an UHV environment with a base pressure of $1x10^{-10}$torr. The films were grown by molecular beam epitaxy (MBE) from a 99.995% pure iron wire. The substrate was a tungsten single crystal that had been cut and polished to expose the [110] face. The cut is accurate to within 0.4°. The first Fe layer was deposited at room temperature and then annealed for one minute to 500K. This slight annealing produces increased sharpness of the resulting pseudomorphic LEED pattern. Further depositions were performed at room temperature with no annealing. The film growth, thickness and quality were monitored by Auger electron spectroscopy (AES) and LEED.

The ac-χ_m measurements were made via the surface magneto-optic Kerr effect (SMOKE) using a focussed He-Ne laser spot with a diameter of approximately 0.75mm. Small coils near the surface produced a sinusoidally oscillating magnetic field, H, which influences the moments in the paramagnetic film above T_c. The field was applied along the film's easy axis $[1\bar{1}0]$. The surface magneto-optic Kerr effect produces a rotation of the polarization of the laser light reflected off of the magnetic surface. After the reflected light passes through a polarizer almost crossed with the incident polarization, the signal manifests itself in changes in the light intensity at

the photo-diode detector. The 1f signal is read by a dual-phase lock-in amplifier that can simultaneously record both the in-phase (or real) susceptibility ($\chi^{'}$(T)) and the out-of-phase (or imaginary) susceptibility ($\chi^{''}$(T)). The raw signal is calibrated to SI units and the entire signal can be represented as

$$\chi(T) = \chi^{'}(T) + i\chi^{''}(T). \tag{4.7}$$

Fig.(4.1) shows a typical measurement of the complex susceptibility measured from a 1.8ML iron film. The measurement was made with an applied field amplitude of 0.7 Oersteds at a frequency of 400Hz.

It would be best to use an infinitesimally small field, but of course this is not possible experimentally. A study of magnetic susceptibility peak shape as a function of field was conducted to see what value of the field would give the best compromise between signal and finite field effects. Fig.(4.2a) and (4.2b) show the maximum value and full-width, half-maximum (FWHM) for the susceptibility peaks respectively as a function of the amplitude of the applied field. The trend below 1.0 Oe in both graphs is independent of field size, (except at extremely low fields where the signal itself disappears) but deviates for higher fields. Resulting measurements of a susceptibility peak measured in these small fields give a FWHM typically between two and three and a half degrees. In these measurements, smaller field amplitudes were accessible but this generally lead to a degradation of the signal-to-noise ratio.

Sample heating was accomplished by running ac current (no more than 1A rms) through a small tungsten wire filament located behind the tungsten crystal. AC-current at 60Hz was used to reduce the effects of stray offset fields at the surface. It had been found in the past that a dc-current introduced a 0.1 Oe offset field at the surface. The 0.1 Oe field caused by the heating filament is much less than the applied field used in the measurement (typically 0.7 Oe) and is much less than the field which

increases the FWHM of the susceptibility peak (Fig.4.2). Any questions about the effect of the heating current were answered by comparing data taken while increasing and decreasing the film temperature respectively. The value of current used in the two methods differed by a factor of three, and there was absolutely no difference in the final data. The temperature of the film was measured using a W/WRh thermocouple embedded in the tungsten crystal and the rate of temperature increase/decrease was in most cases limited to 0.2deg/min. This low rate more than adequately compensates for thermal variations in the crystal and permits even heating of the film over the entire surface (app. $1cm^2$).

In a few cases, the susceptibility was also measured in the two directions orthogonal to the assumed easy axis: [001] (in-plane) and [110] (perpendicular) in order to check that no perpendicular magnetization was present. These measurements showed zero signal, indicating no moments along those directions. This result does not necessarily contradict the findings of Pietzsch *et al*[58] since the temperature and substrate step density are very different in the two experiments.

Data Analysis

To fit the susceptibility data to eq.(4.1), an objective, many-parameter fit was used to determine the best values for the Curie temperature, T_c, the critical exponent γ, the critical amplitude, χ_o, and t_x which is the smallest value of the reduced temperature to show power law scaling.

The fit is performed in double logarithm space [ln(χ) vs ln(t)], the slope of which will correspond to the critical exponent. Taking the logarithm of the susceptibility necessitated the removal of data points where χ(T) goes to zero. Since these points are weighted the least, this "weeding" out of points does not adversely affect

the final fit. A small range of temperatures close to the peak was chosen for possible values of T_c used in the reduced temperature. For each considered value of T_c, a weighted least-squares fit was performed on the data in the new ln-ln data space from $\ln(t_{max})$ (which always corresponds to the data point measured at the highest temperature) to a cutoff value $\ln(t_x)$.

t_x was itself varied over a range from just below t_{max} to a value of t where the power-law scaling was obviously no longer valid. The variance of the fit was minimized for the best value of T_c and the cut-off, t_x. The variance is the best test for a fit made in a many-parameter space [59] where the number of points does not remain constant. It is given by:

$$s^2 = \sum_{i_{tmax}}^{i_{tx}} \frac{(ln(\chi_i) - F(t_i))^2}{\sigma_i^2} / \sum_{i_{tmax}}^{i_{tx}} \frac{1}{\sigma_i^2} \tag{4.8}$$

where χ_i is the i^{th} data point, $F(t_i)$=$\ln(\chi_o) + \gamma ln(t_i)$ is the fitted function, and σ_i is the error associated with the logarithm of each data point. Fig.(4.3) shows data for which a contour plot of s^2 as a function of T_c and $\ln(t_x)$ is presented in Fig.(4.4) . There is a global minimum at T_c = 455.84K and $\ln(t_x)$ = -5.355 (corresponding to a temperature of 457.99K). There are local minima exhibited in the graphs that have higher values for t_x than the global minimum. The fact that the global minimum fits the data closer to T_c increases its significance.

To get an error estimation on T_c, the fits were recalculated while keeping the optimum value of $\ln(t_x)$=-5.36 to allow for a careful statistical χ^2 analysis for a consistent number of data points. According to statistics for a multi-variable fit [59], the 65% confidence range for a parameter is given by the parameter values that increase the unreduced χ^2 by one. Fig.(4.5) shows χ^2 versus T_c for the data in fig.(4.3). Due to the good signal-to-noise of the data and the large number of points in the limited temperature range, the error for T_c is very small. The number

of points in the fit used for Fig.4.5 is 1905, which gives a reduced χ^2 for the fit of 1.8, signifying a very good fit to the data. The T_c value from this analysis is 455.84±0.03. While this range of T_c creates an uncertainty in γ on the order of the error from the least-square analysis, the two effects should compound to increase the confidence limit on γ slightly. The value for the critical exponent from the particular data set in fig.(4.3a) is $\gamma = 1.75 \pm 0.02$. The fitted critical amplitude χ_o is $7.3 \pm 0.3 \times 10^{-3}$.

It now becomes necessary to check for both dynamic and demagnetization effects in the data. It has already been remarked that a demagnetization factor equal to $1/\chi_{max}$ provides an upper limit on the value of N. This assumption would lead to a value of N for the data in fig.(4.3a) to be about 1/150 or 6.67x10^{-3}. Numerical simulations show that once the value of the product $N\chi$ approaches 0.05, the observed power law behaviour of the intrinsic susceptibility is lost (see eq.(4.4)). For this data set, this would occur at a temperature of 464.2 K, giving a value of $\ln(t_x)$ approximately equal to -4.0. In other words, if we believe the above estimate for N, then no linear segment in double-log space would extend closer to T_c than this. The results in fig.(4.3b) clearly show the linear segment extending much lower than -4.0. The value of N must therefore be much smaller. The power-law behaviour in fact deviates at a temperature of approximately 458.0K. If we take the '5% rule' a step further, the maximum value of N then becomes approximately 1/1632 or 6.1x10^{-4}, a full order of magnitude lower than the previous estimate. This lower value is more in keeping with the value of N expected from geometric arguments and provides a new upper limit on N.

Checking the saturation from dynamic effects requires a more definite knowledge of the time response of the moments as a function of temperature than these measurements currently allow. However, a simple calculation can be made on a the-

oretical basis. Near T_c, the relaxation time of the magnetization will undergo critical slowing down which, by theory, follows the formula:

$$\tau(T) = \tau_o t^{-z\nu} \tag{4.9}$$

where ν is the critical exponent associated with the correlation length and z is the critical slowing down exponent. While there are very few experiments that measure the critical slowing down of the relaxation time, τ, on ferromagnetic systems, theoretical simulations [60, 61] suggests that the value of z should be approximately 2.2 for the 2d Ising system. The value for τ_o should be very small, on the order of inverse-GHz to agree with FMR resonance frequencies.

To see no dynamic effect in χ_{int} as per eqn.(4.5) requires $(\omega\tau)^2 < 0.05$. Using $z\nu = 2.2$, $\tau_o = 1\text{x}10^{-9}$s and $\omega=(2\pi)150.0$Hz, we find that $\ln(t_x)$ will be -5.6. This is close to the fit value for $\ln(t_x)$ and may be the reason for the saturation of the susceptibility. Better estimates of τ_o and $z\nu$ are required to pursue this question further.

Results from Many Films

Critical power-law fitting was performed on a sample of 25 different measurements from many films grown between 1.5 and 2.0 ML. Fig.(4.6) shows a plot of γ as a function of $\ln(t_x)$ for all 25 measurements. For films with a small $\ln(t_x)$, γ is consistently close to the 2d Ising value. For films with larger $\ln(t_x)$, γ grows systematically larger. It is also apparent that the value of γ is correlated to the film thickness.

The following weighted and unweighted average results for γ can be given: (1) For bilayer films, the weighted average value of γ is 1.75±0.015 with an unweighted average of 1.74±0.023 (2) For sesqilayer films, the weighted average is 1.63±0.01. (This weighted average is suspect as there are only 3 data points with small individual

error which do not overlap). The unweighted average is 1.68±0.13. (3) The weighted average value of γ for films with $\ln(t_x)$ less than -5.35 is 1.76±.01. The unweighted average is 1.76±0.04. Most of the films with values of t_x in this last range are either 2.0 or 1.5ML, but there is also one measurement at 1.75ML and another just below 1.5ML.

Films with a thickness of 2.0ML and 1.5ML consistently have the lowest values of $\ln(t_x)$ and these are the films that give (on average) the 2d Ising result. If these data are re-analysed by artificially increasing $\ln(t_x)$, the value of γ does not increase significantly. Fig.(4.7) shows data for a 1.75 ML film which gives a non-Ising value of γ. It is clearly not meaningful to decrease $\ln(t_x)$ for this data. It is thought that the higher values of t_x are an indicator of an as-yet not understood process that affects the power law scaling when the film thickness is just below 1.5 ML or between 1.5 and 2.0ML. It is possible that this process is also responsible for the high value of γ reported for films of 0.8ML thickness [15].

We have examined several possible explanations for this behaviour. The first involved using corrections to scaling arguments [36, 62] that should be taken into account for fitting data far away from T_c. If this is the case, then the effective value of the exponent, γ_{eff} is approximated by

$$\gamma_{eff} = \gamma - a\Delta|\bar{t}|^{\Delta}, \tag{4.10}$$

where a is a constant, $\bar{t}$ is some "average temperature" representing the fitting range, and the exponent Δ is close to 0.5 for Ising systems [36] regardless of the dimensionality of the system. If t_x is chosen as $\bar{t}$, the data in fig.(4.6) can be reasonably described by eq.(4.10) with $\Delta \approx 3$. The large discrepancy between the fitted and theoretical value of Δ suggests that corrections to scaling are not the important factor here.

Another possibility for the rising value of γ is dimensional crossover from

an Ising system to an anisotropic Heisenberg system as a function of temperature [63]. It is well known that true two-dimensional Heisenberg systems cannot support long range magnetic order above T=0 [22], but only a small amount of anisotropy is required to lift this restriction [23]. It is possible that the films that exhibit high values of $\ln(t_x)$ are showing higher values of γ because they have a smaller anisotropy and the exponent is measured in a temperature range where it is still crossing over from one universality class to another. This explanation was also offered by Elmers et.al. [15] for their 0.8ML results, and it is interesting to note that the value of $\ln(t_x)$ in their result would be -5.3, which is consistent with the onset of high γ values in this study. However, there are several arguments against this idea. First, none of the data with an Ising exponent show a crossover to larger γ when t_x is artificially increased. Second, none of the data used in this work, including those data sets that fit with a $\ln(t_x)$ value less than -6, shows anything resembling a 'break point' in the double-log slope indicating different critical power laws over different temperature ranges. Therefore, there is no clear indication that dimensional crossover is occurring. Finally, a reduced anisotropy should result in a change in the trend of the transition temperature as a function of thickness [24], an effect which we do not observe.

The third possibility is that the films in the sensitive thickness range have a wider distribution of transition temperatures. It is easy to understand how this would effect the fitted slope. If some fractional area of the film undergoes a phase transition at a temperature slightly above the average "mean" value of T_c used to reduce the temperature for the logarithmic plot, then those areas will register as an artificially high slope in the fit. While the exact nature of the distribution is unknown, it is certain that any distribution with values above the T_c used in the fitting routine will increase the fitted exponent. To gauge the effect quantitatively, a

series of data sets were modeled using a normalized Gaussian distribution of T_c and an intrinsic value of γ of 1.75. No significant increase is found to occur as long as the half-width is less than 0.25K. A half-width of just over 0.5K to cause a 1% increase in γ, and a half-width of 1K gives a fit exponent of 1.81, a 3.5% increase. To achieve a fitted value for γ of 3 (near the maximum fit value in the 25 measurements), requires a half-width of 2.5K. The high values are the result that with this distribution of transition temperatures, a simple power-law fit is no longer valid. It may be that the films less than 1.5ML and between 1.5 and 2.0ML are more sensitive to small structural inhomogeneities that give rise to a wider distribution of T_c. Films with a complete second monolayer will be more homogeneous than films that are slightly thinner. We speculate that the distribution of transition temperatures may be related to the distribution of atoms that are located at step edges between the first and the incomplete second monolayer. For the complete 2ML, the films should be very homogeneous and a narrow distribution may be expected. The 1.5ML films have equal areas that are 1ML and 2ML thick respectively and as such present a uniform configuration of steps which have been shown [57] to give a correlated magnetic state. The 1.75 films are on the threshold of the percolation limit of the second monolayer and it is possible that slight structural deviations are more likely to cause a wider distribution of transition temperatures. This suggestion may also explain the high value of γ reported for 0.8 ML films[15].

Conclusion

We report the results of fitting measurements of the magnetic ac-susceptibility for critical power law exponents. We find that the critical exponent for bilayer Fe/W(110) films to be 1.75±0.02 and for films in general with a value of t_x below $4.75\text{x}10^{-3}$, $\gamma = 1.76 \pm 0.01$. This result confidently place this system in the

2d Ising universality class. The fitting routine allows the simultaneous extraction of the critical exponent and the critical temperature from a single measurement of the susceptibility. There is evidence of another process which affects fitting of the susceptibility for certain thicknesses. This may be due to these films having a larger distribution of critical temperatures.

The authors wish to acknowledge the many technical contributions made by Marek Kiela. This work was supported by the National Science and Engineering Research Council of Canada.

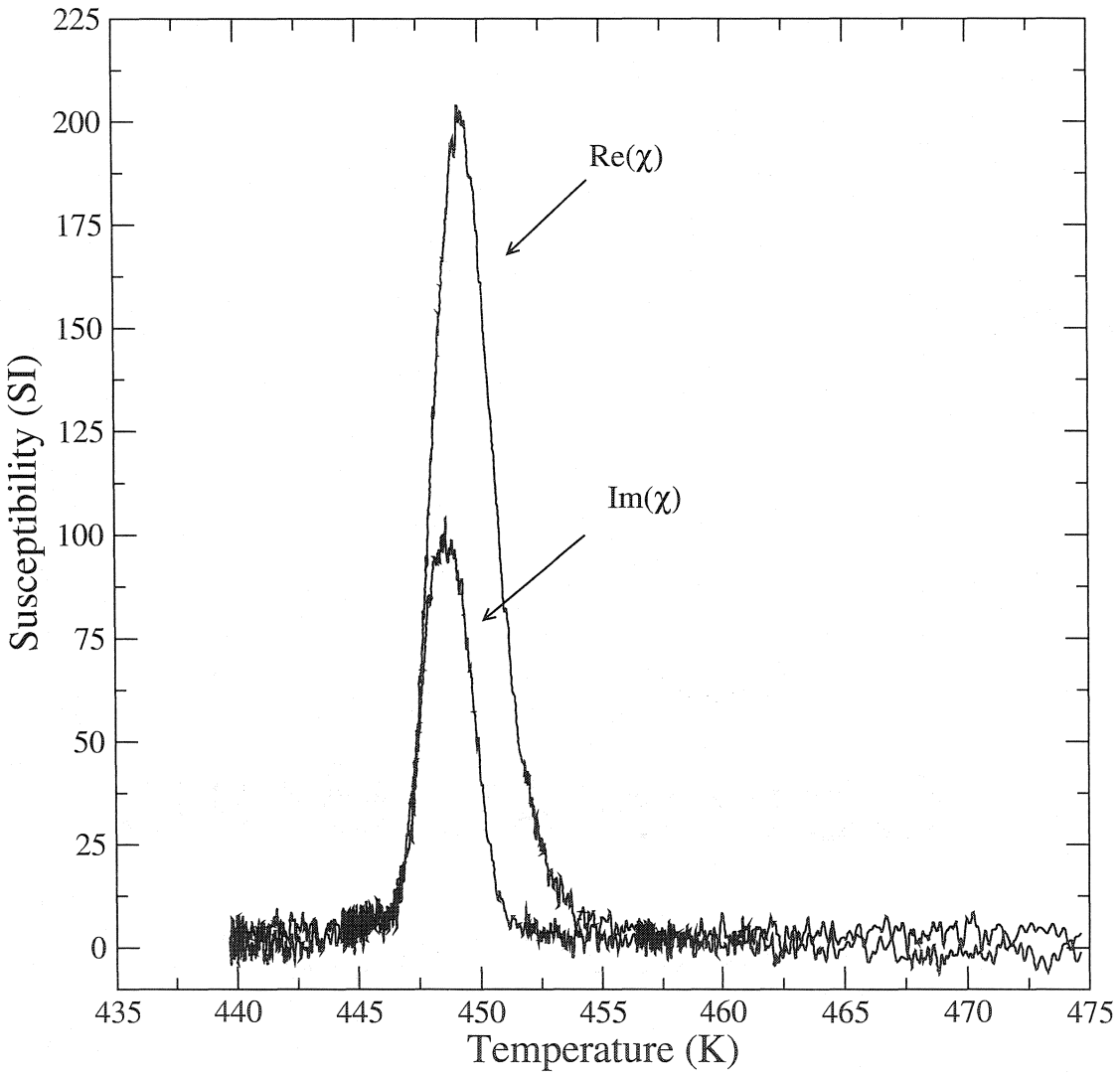

Figure 4.1: Magnetic ac-susceptibility measured from a 1.8ML film of iron grown upon W(110). The real and imaginary components of the susceptibility were measured simultaneously.

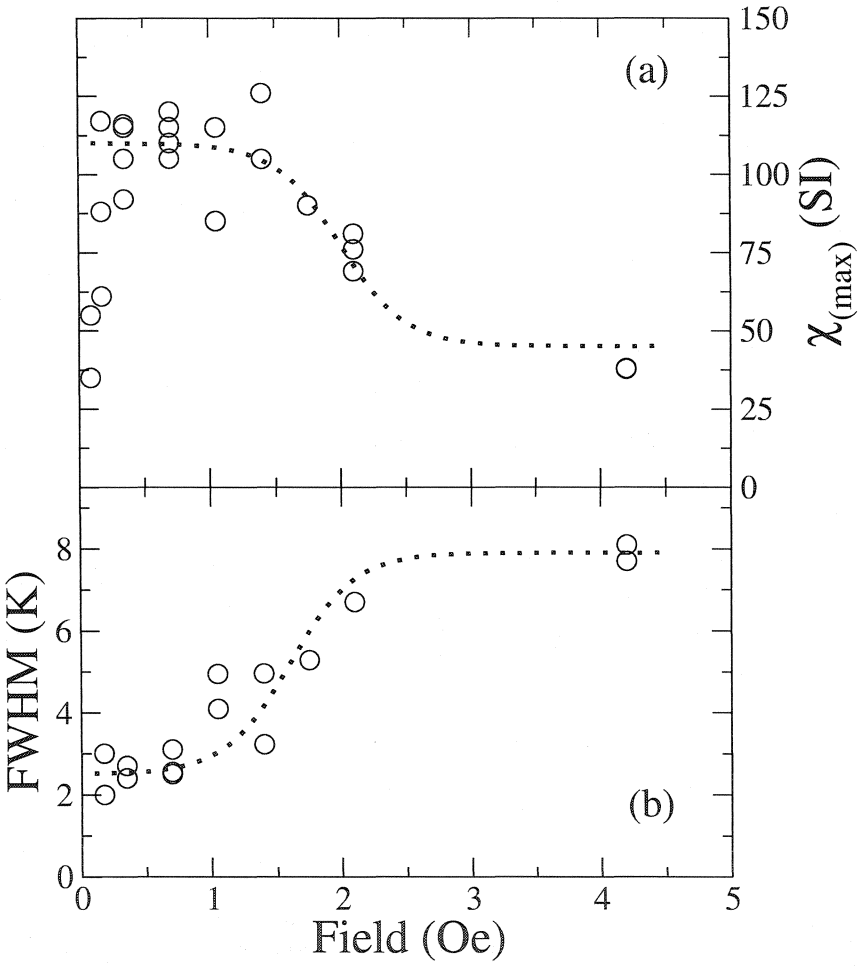

Figure 4.2: (a) The maximum value of the magnetic susceptibility as a function of applied magnetic field. (b) FWHM of the real susceptibility peak plotted as a function of applied field amplitude. The minimum half-width is achieved for fields less than 1 Oersted.

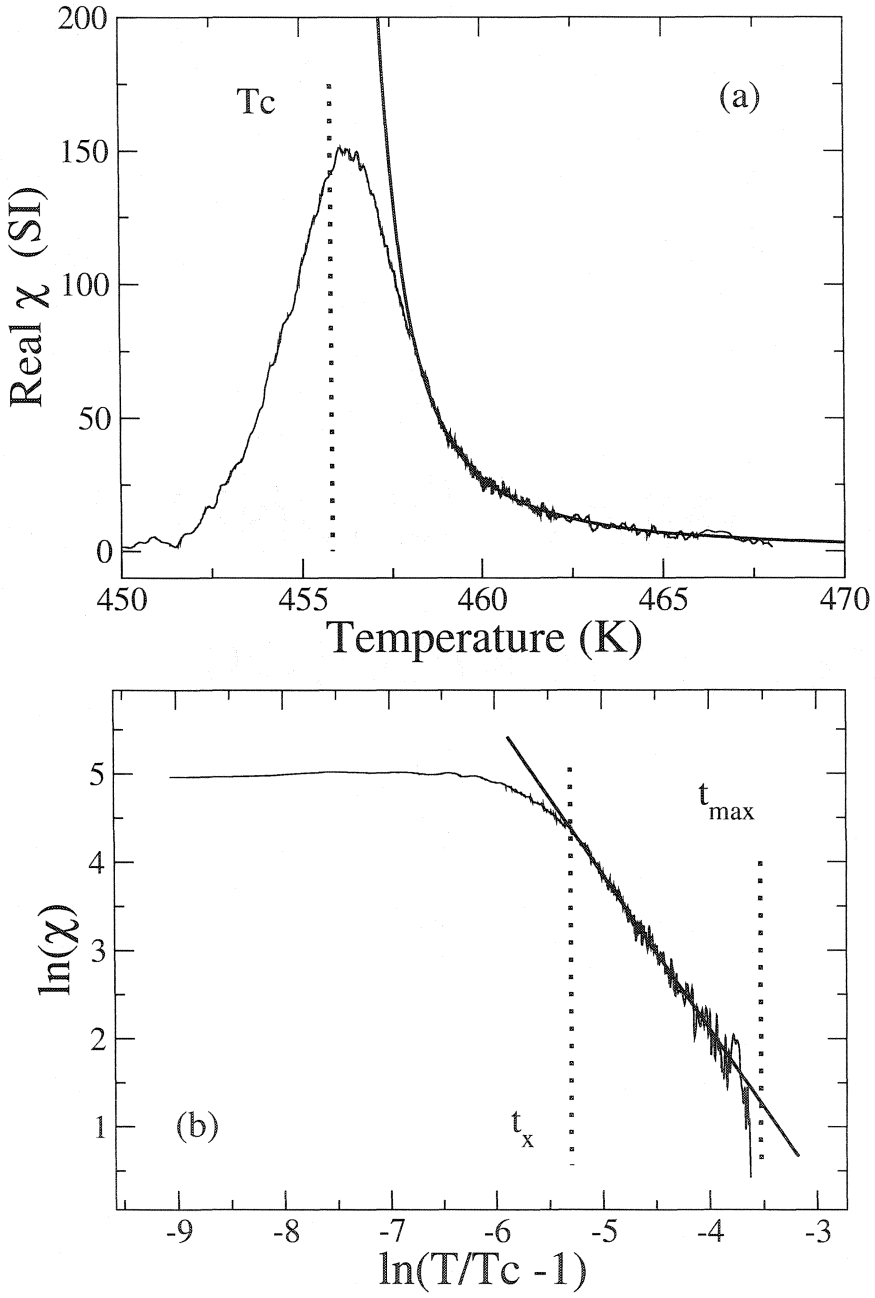

Figure 4.3: Power law fit for a typical susceptibility measurement. (a) χ versus temperature. Solid line shows the fit in linear space and dotted line shows position of T_c. (b) Fit in log-log space, with dotted lines showing position of t_{max} and t_x. t_{max} always corresponds to the maximum temperature which was measured. The solid line represents the linear function fit in the double-log space.

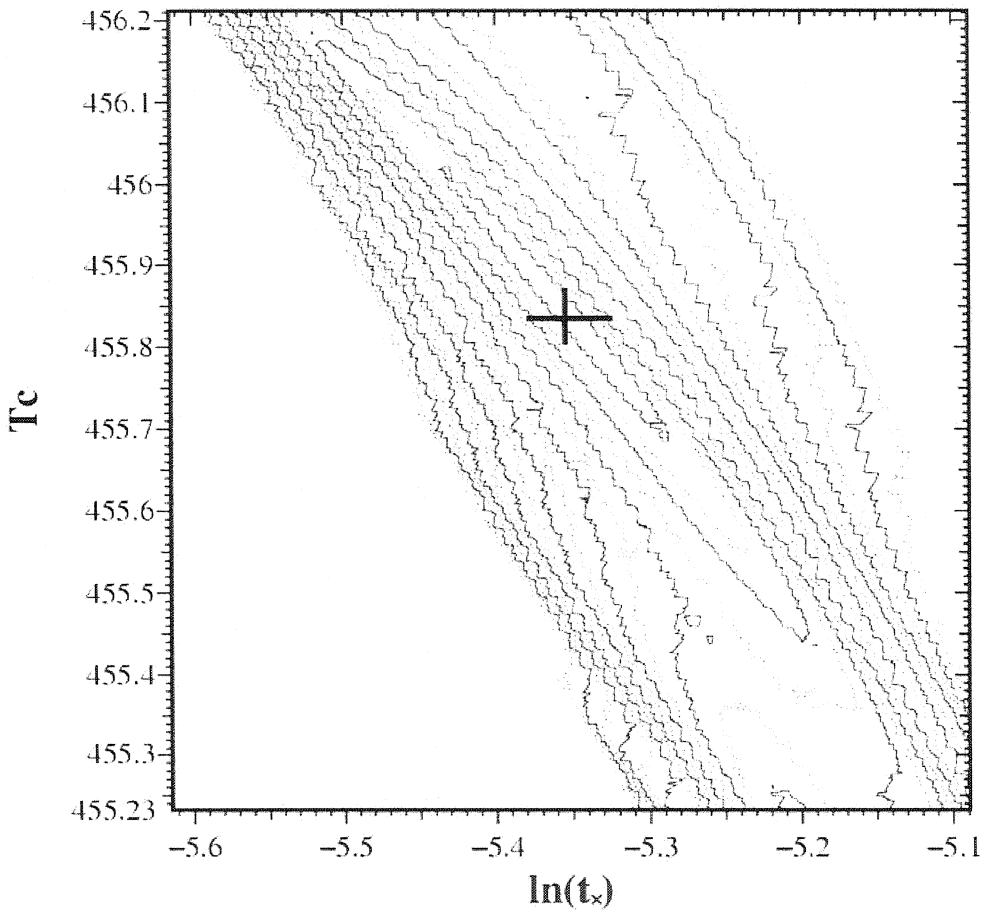

Figure 4.4: Contour plot of s^2 as a function of T_c and $\ln(t_x)$. The global minimum (indicated by the cross) shows the values of T_c=455.84 and $\ln(t_x)$=-5.355 corresponding to the best fit.

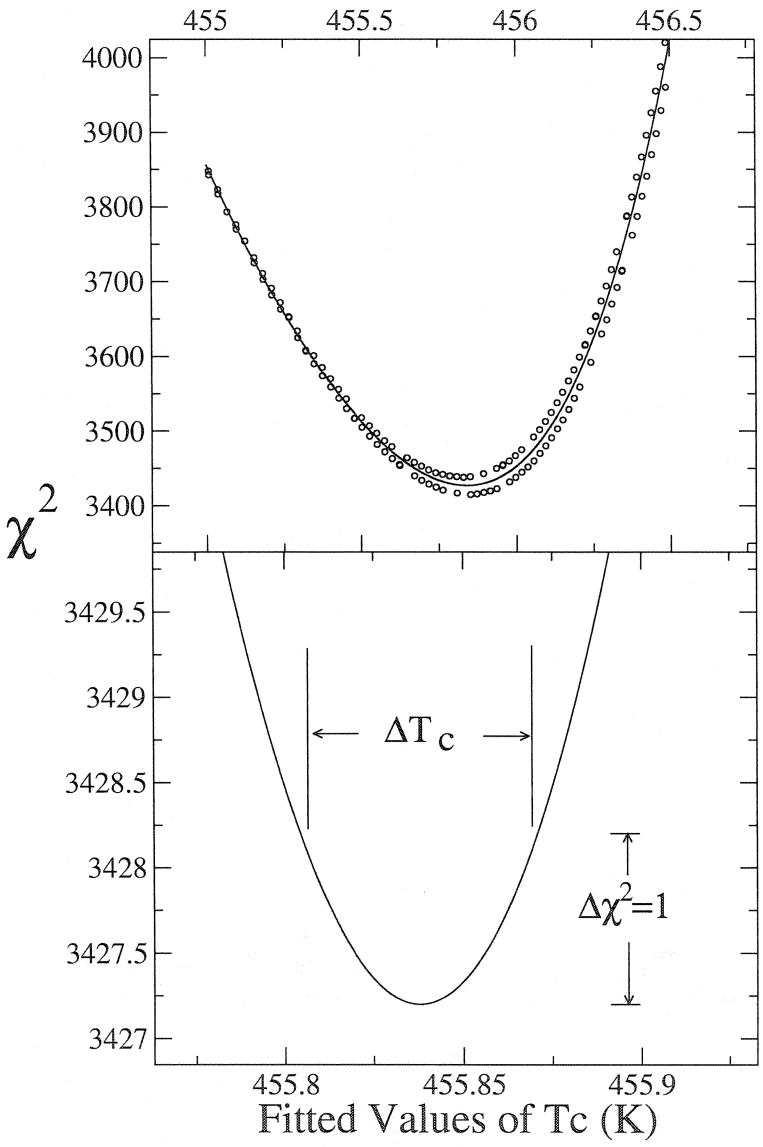

Figure 4.5: Graphs of χ^2 versus value of T_c used in fit. Fig.(a) shows the minimum in χ^2 with a smooth function fit to the points. Fig.(b) shows the fitted curve with an indicated range corresponding to a change in χ^2 of 1.0. The value of T_c with error for this data set is $T_c = 455.84 \pm .03$K.

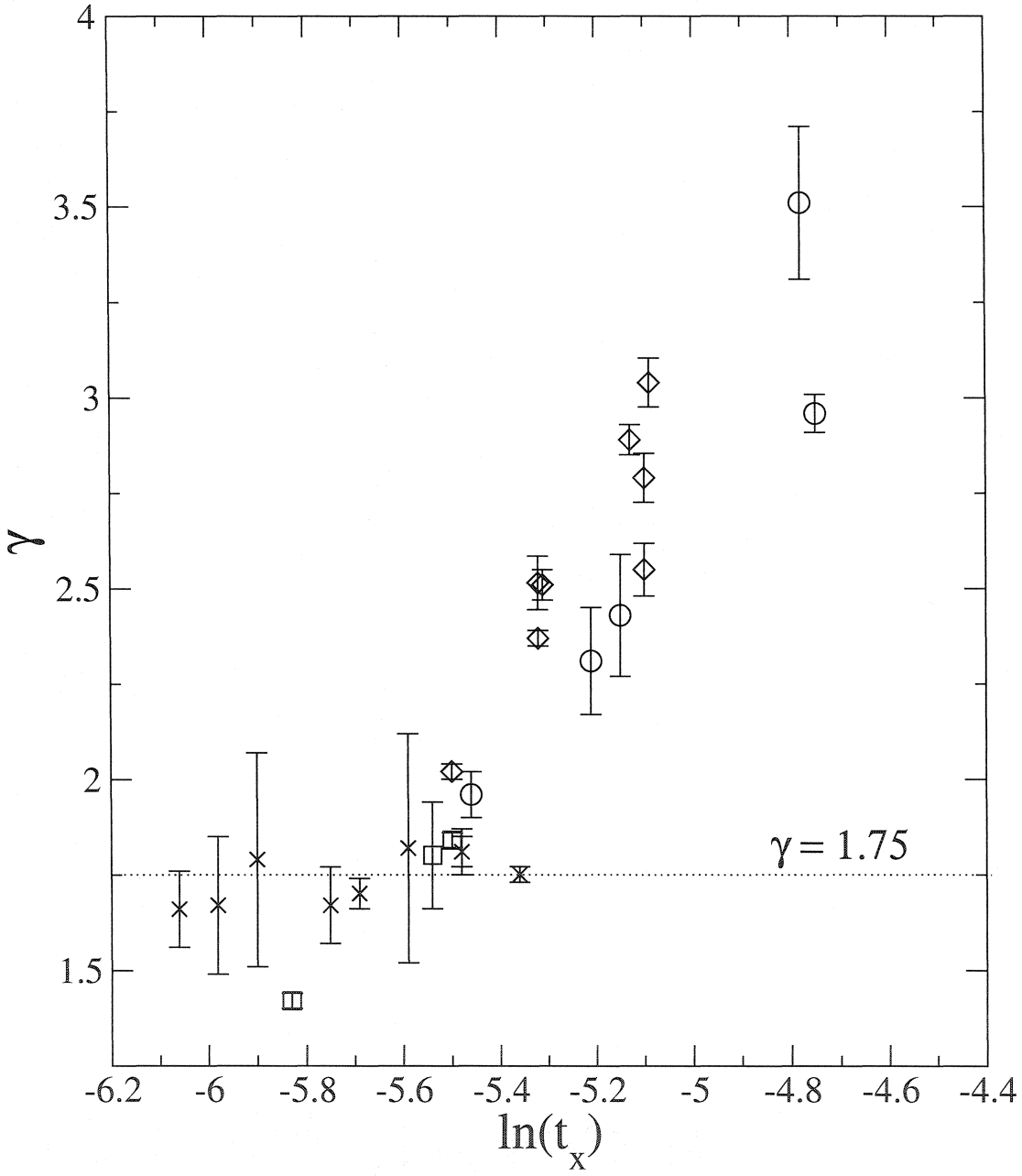

Figure 4.6: Best fit values of γ plotted as a function of reduced temperature cutoff, $\ln(t_x)$. Open circles represent films that are slightly less than 1.5ML, squares are 1.5ML films, diamonds are 1.75ML, and X's are 2.0ML.

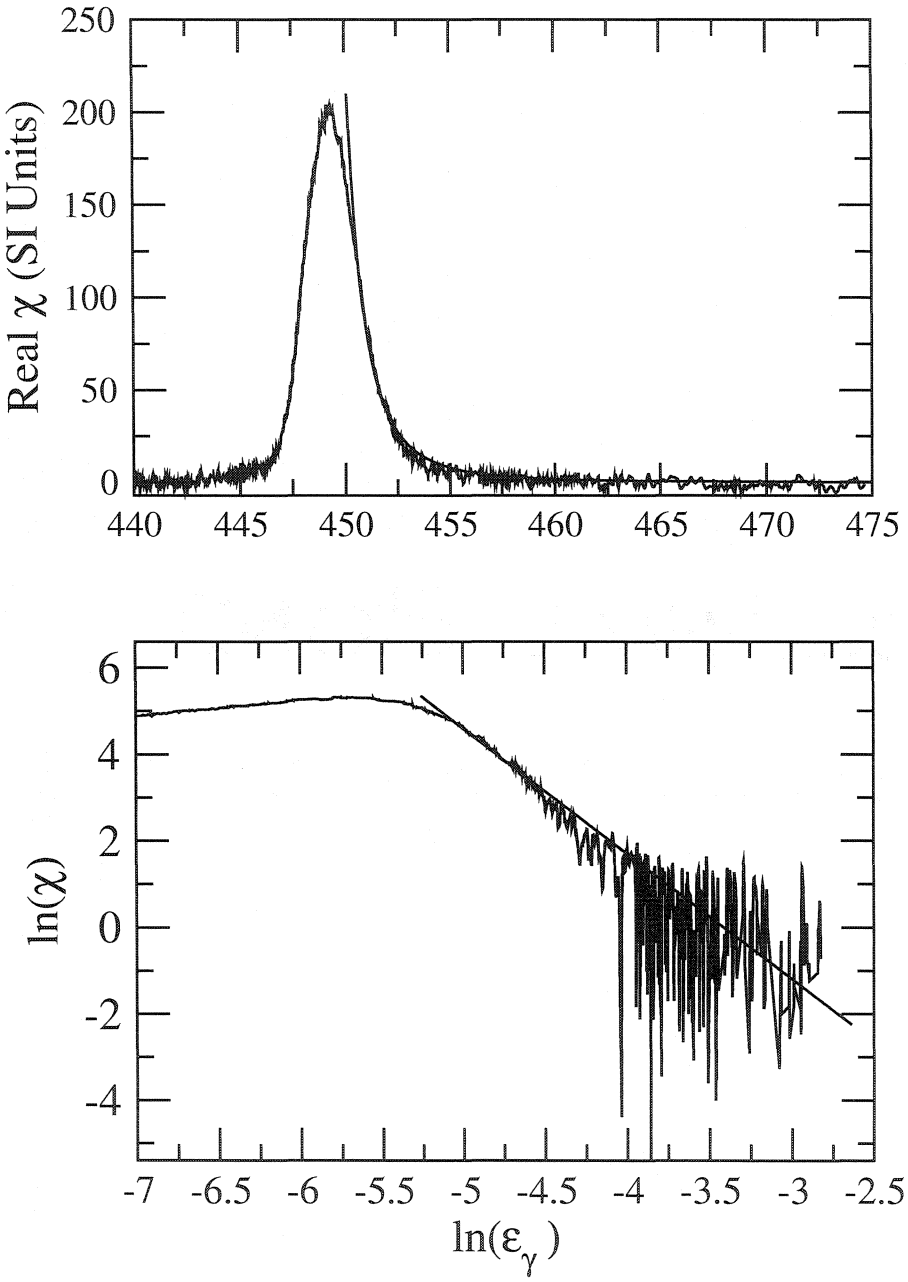

Figure 4.7: Susceptibility measurement and fit for 1.75ML film. Objective fitting algorithm fits a value of γ outside 2d Ising class. Solid line in both graphs represent the fit. Minimum in s^2 occurs at T_c=447.78K and $\ln(t_x)$= -5.13 giving $\gamma = 2.89 \pm .04$ and $\chi_o = 5.3 \pm .5 \times 10^{-5}$.

4.2 Measurement of the Critical Slowing Down Exponent z

The following section contains the complete manuscript of a manuscript that has been submitted to Physical Review Letters. The authors list is M.J. Dunlavy and D. Venus. As with the manuscript included in the previous section, references to and labelling of citations, figures, tables and equations have been modified for the sake of consistency with the complete thesis. All figures for this paper are located at the end of the subsection.

Some material on experiment details, the relaxation model, and some of the analysis are repeated from the previous section as the two projects are closely related. As of this writing, the paper is currently under review.

Measurements of Critical Slowing Down in 2d Ferromagnetic Ultrathin Films

M.J. Dunlavy, D. Venus

Dept. of Physics and Astronomy, McMaster University, 1280 Main St. West, Hamilton Ontario, Canada

Abstract

Critical slowing down has been experimentally measured in the dynamics of the magnetisation of a two dimensional Ising ferromagnetic system. The relaxation time was measured from a bilayer of iron grown atop a W(110) substrate using the complex magnetic ac-susceptibility χ. The observed value of the critical exponent for the slowing down of the relaxation time τ near the Curie transition is $z\nu = 2.09 \pm 0.06$ (95% confidence), in agreement with most contemporary theories and simulations. Further analysis of τ reveals the saturation of the correlation length due to finite size effects (on the order of several hundred lattice spaces) as the temperature is decreased towards T_c.

-

The dynamic scaling hypothesis originated in the late 1960s [64, 65] as an extension of the very successful application of the static scaling hypothesis to the description of critical phase transitions. The dynamic scaling hypothesis implies that as the characteristic correlation length of the system diverges near a transition, fluctuations in the correlated regions take longer to equilibrate and thus the dynamics of the system become slower. The characteristic time τ for a correlated region to change grows as the power z of the correlation length, leading to the phenomenon of critical slowing down.

Dynamic universality classes difficult to realize in the laboratory have presented an experimental challenge in the study of the dynamics of magnetic systems. An important example of this is the 2d Ising model. The dynamical behavior of this model has gained prominence as the study of ultrathin magnetic films matures and it becomes clear that two dimensional ferromagnets can exist, in contradiction to the Mermin-Wagner theorem [22], due to the presence of magnetic anisotropies which transform the universality class to that of the 2d Ising model close to the magnetic phase transition[23]. Consequently, there have been many theoretical studies of critical slowing down for this model (which belongs to Model A in the Hohenberg and Halperin hierarchy of dynamic universality classes [43]). Lacasse *et al* [60] give an excellent survey of this work up to 1993. As simulations and theories became more sophisticated, most current studies place the value of z between 2.1 and 2.25 with many theoretical results clustered near 2.13.

There has been little agreement between these theoretical predictions and experiments. This is partially due to the difficulty in producing magnetic systems that show true two dimensional behaviour. Experimental investigations have been confined to a few studies of layered bulk antiferromagnetic materials which approach the 2d Ising model because of the very small effective exchange between layers. Slivka *et al* find $z = 1.77 \pm 0.05$ for $KFeF_4$, [66] and Keller *et al* find 1.29 ± 0.09 for the same material[67], both using Mössbauer spectroscopy. Hutchings *et al* find $1.69 \pm .05$ for Rb_2CoF_4, [68] using neutron scattering. However, no matter how small interlayer interactions are in bulk compounds, they can lead to difficulties near T_c where the extended correlation length of the fluctuations can give rise to additional modes of dissipation.

This Letter reports measurements of the critical slowing down exponent as-

sociated with the 2d Ising phase transition of an ultrathin ferromagnetic film. These films provide a nearly ideal system for the study of phase transitions in two dimensions. The extreme dimensional ratio between the film thickness (on the order of atomic layers) and the lateral film length allow for the design and fabrication of true two dimensional structures where the critical properties do not vary over the thickness of the film. Several studies exist that use various surface magnetometry techniques such as Kerr effect and spin polarised spectroscopies to measure static critical exponents such as β [15, 10, 9] and γ [69, 70, 71] for the magnetisation and the susceptibility respectively. There is a distinct advantage in using ferromagnetic materials for studies of critical slowing down in that it takes only small fields to create disturbances in the magnetisation near the transition. Studies using antiferromagnets must wait for the excitations to be spontaneously created and stabilised on a time scale that becomes prohibitive near the transition.

Critical slowing occurs in a system that is about to undergo a phase transition. Fluctuations near T_c give rise to excitations (δm) in the value of the order parameter. For small deviations, the relaxation of the order parameter at temperature T will follow an exponential law given by [72]:

$$\delta m(t) \propto exp\left(\frac{-t}{\tau(T)}\right) \tag{4.11}$$

where t is time and τ is the relaxation time. τ is dependent upon the correlation length ξ of the fluctuations in the system. As such, it will diverge at T_c according to a power-law equation given by:

$$\tau(T) = \tau_o \left(\frac{\xi(T)}{\xi_o}\right)^z = \tau_o(\epsilon^{-\nu})^z \tag{4.12}$$

where ν is the critical exponent associated with the diverging correlation length (ν = 1.0 in the 2d Ising universality class [2]), τ_o and ξ_o are amplitudes and ϵ is the

reduced temperature given by $[(T - T_c)/T_c]$ above T_c.[2]

The intrinsic magnetic susceptibility of a ferromagnetic system follows the power-law relationship given by:

$$\chi_{int}(T) = \chi_o \epsilon^{-\gamma} \tag{4.13}$$

where χ_o is the critical amplitude and γ is the critical exponent of the static susceptibility. In an ac-susceptibility measurement in the presence of a small applied oscillatory magnetic field at frequency ω, the dynamic complex susceptibility in the relaxation approximation becomes:

$$\chi_{dyn}(T) = \frac{1 - i\omega\tau(T)}{1 + \omega^2\tau^2(T)}\chi_{int}(T). \tag{4.14}$$

The expression is more complicated if the demagnetisation factor of the system is significant. For 2 ML Fe/W(110), the extreme aspect ratio of the system combined with the fact that the magnetic moment is strongly oriented in the plane of the film combines to give a demagnetisation factor small enough that it can be effectively ignored [71]. With a measurement of the complex susceptibility, the value of τ can be derived from the ratio of the imaginary to the real component of the susceptibility [74] as follows:

$$\frac{\mathrm{Im}(\chi(T))}{\omega \mathrm{Re}(\chi(T))} = \tau(T). \tag{4.15}$$

This method gives an average value of the relaxation time over the whole of the system [75]. It is assumed that the average value will be sufficient for the measurement and that the distribution is narrow for a good quality film.

[2] An alternate formulation of dissipation uses the Landau-Lifshitz [73] damping parameter λ : $\frac{\partial m}{\partial t} = -\lambda H_{eff} = -\lambda(\frac{m}{\chi_{eff}} - H)$. Analysis of λ has the advantage of removing from the slowing down exponent that portion of the temperature dependence which is due to the divergence of the static susceptibility. The relationship between the two formulations is $\tau = \frac{\chi_{eff}}{\lambda}$. We use eq.(4.11) to allow comparison to the majority of theoretical work.

The power law divergences in eq.(4.13) and (4.12) cannot be observed in experimental data very near to T_c. Once a sample is cooled as $T \rightarrow T_c^+$, the correlation length will saturate at some value that is dependent on a relevant length scale like sample or grain size and the measured susceptibility will reach a maximum value based on this length scale. The maximum value of the susceptibility data will also be affected by the measurement frequency, as can be seen from eq.(4.14).

Measurements of the ac magnetic susceptibility were made from iron bilayers that were grown epitaxially and pseudomorphically upon a tungsten single crystal that had been cut and polished to expose the (110) face [76]. Film thickness and quality were monitored using Auger electron spectroscopy (AES) and low energy electron diffraction (LEED). All magnetic properties were measured using the surface magneto-optic Kerr effect (SMOKE) with a focussed HeNe laser with a diameter of 0.7mm. Susceptibility was measured using a standard lock-in technique [17] which determines the real (in-phase) and imaginary (out-of-phase) components simultaneously. A small magnetic field is applied from a set of Helmholtz coils that have been calibrated at the substrate surface using a Hall probe. Temperature is measured using a W/WRe thermocouple inserted into the tungsten substrate and the rate of temperature increase/decrease is on the order of 0.2deg/minute, which is small enough to remove thermal variations across the film. Heating is accomplished by radiative emission from a small tungsten wire filament located beneath the substrate.

The size of the sinusoidal magnetic field used in the measurements is an important parameter. If the field is too large, then the finite field will saturate $\chi_{dyn}(T)$ at a higher temperature than does the correlation length and critical scaling will not be observed. If the field is too small, then the signal-to-noise ratio of $\mathrm{Im}(\chi(T))$ would be too small to allow meaningful analysis for $\tau(T)$. For these samples, a separate study

has shown that the amplitude and half-width of the susceptibility peak is independent of field amplitude for applied fields less than 1.0 Oe [71]. A field of 0.7 Oe was used in the present experiments to maximise the signal-to-noise but minimise finite field effects. It is not clear *a priori* that this field is small enough to allow the asymptotic critical region to be observed. However, since the analysis that follows shows that this choice allows the robust extraction of the 2d Ising exponent γ from χ_{dyn}, it is clear *a posteriori* that the field is small enough.

In the first part of the data analysis, the real susceptibility data is analysed for T_c and γ. The real part has a large signal above T_c so that a statistically significant analysis for T_c can be performed. As well, the fitted value of γ ensures that the film is properly behaving as a two dimensional Ising system.

Figure 4.8 shows a typical measurement of the complex ac-susceptibility for a 2.0±0.1ML Fe/W(110) film, measured in a applied field frequency of 400Hz. As is normal, the peak of the imaginary susceptibility occurs at a temperature lower than the peak of the real due to a combination of dynamical and dissipative effects. A objective statistical fitting method (related in detail in ref. [71] and similar to that performed by Arnold *et al* [77]) simultaneously fits the critical temperature T_c, the critical amplitude χ_o, the critical exponent γ, and the value of the reduced temperature ϵ_γ where power-law scaling no longer holds near T_c. A weighted linear least-squares fit for χ_o and γ was performed on the data from the maximum temperature point to the cutoff ϵ_γ in double-log space for varying values of T_c and ϵ_γ. The variance of the fit is shown in a contour plot inset to figure 4.8. The minimum of the variance gives the best values of T_c and ϵ_γ. The fitted values of the power-law for this data set are as follows: $\gamma = 1.80 \pm 0.06, \chi_o = 5.53 \pm 0.5 \text{x} 10^{-3}$ (SI units), $T_c = 453.03 \pm 0.02K$ and $\ln(\epsilon_\gamma) = -5.71$ (approximately 2.1K above T_c). T_c was found to be just slightly

Table 4.1: Fitted values for dynamic scaling from four separate measurements of the complex susceptibility. Statistical errors are 1 σ.

Film	ω	γ	$z\nu$	τ_o(s)	ξ_{sat} (ξ_o)
1	$2\pi(400)$	1.80±.06	2.09±.03	$2.6\pm0.6 \times 10^{-10}$	730
1	$2\pi(400)$	1.67±.10	2.01±.07	$4.0\pm0.3 \times 10^{-10}$	720
2	$2\pi(150)$	1.75±.02	2.13±.04	$1.7\pm0.3 \times 10^{-9}$	425
2	$2\pi(150)$	1.81±.06	2.04±.06	$2.1\pm0.5 \times 10^{-9}$	475
average		1.76±.02	2.09±.02		

below the peak in the real susceptibility, in agreement with a previous susceptibility measurement on Fe/W(110) monolayers [15]).

Continuing to step two of the analysis for the relaxation time, the ratio of the complex susceptibility is taken as in eq.(4.15). The result is plotted on a double-log graph to determine the linear segment that shows power law scaling. Because the real and imaginary $\chi(T)$ are measured simultaneously, the value of the Curie temperature for τ is precisely the same value as determined by the fit for γ. Fig.(4.9) shows that the data between ln(ϵ) values of -5.26 and the cutoff ln(ϵ_z) of -6.51 form a significant linear segment composed of 137 data points. A weighted least square fit finds a critical exponent product $z\nu$ of $2.09 \pm .03$ with an amplitude $\tau_o = 2.6 \pm 0.6\text{x}10^{-10}$s. The order of magnitude of the amplitude (inverse GHz) is consistent with the value of τ_o expected from FMR measurements. The reduced χ^2 of the fit is 2.69.

Among a number of susceptibility measurements made from 2ML films, four have a large enough number of data points in the range between ϵ_γ and ϵ_z to allow meaningful analysis for $z\nu$. The individual fitting results are listed in table 4.1. The resulting average value for γ is 1.76±0.06 (95% confidence), in agreement with the 2d Ising value of $\frac{7}{4}$. The average for $z\nu$ is $2.09 \pm .06$ (95% confidence). Since it is well known that the 2d Ising value of ν is 1.0, the value for the product of $z\nu$ is in fact the value for z itself. To our knowledge, this is the first measurement of z to confirm

the current theoretical consensus value. We speculate this is due to the fact that this is the first reported measurement made from a ferromagnetic ultrathin film, which is a true realisation of a 2d Ising system.

These measurements of the critical slowing down are difficult because the region of data above T_c that shows dynamical scaling is the 1.8-2.0K range between ϵ_z and ϵ_γ. Far above the transition temperature, the signal-to-noise of the data becomes very low, because $z\nu > \gamma$ and τ disappears very quickly. However, at ϵ_γ the susceptibility stops growing like a power law because of the dynamical factor in eq.(4.14). Using the fitted values of τ_o and $z\nu$ from fig.(4.9), the dynamical factor $(\omega\tau)^2 = 0.01$ at ϵ_γ. This is consistent with numerical modeling which shows that departures from linearity on a log-log plot are clearly evident when $(\omega\tau)^2 \approx 0.05$. Unlike $\mathrm{Re}(\chi)$, the power law behaviour of τ continues because the dynamical factor cancels out in eq.(4.15). Even closer to the transition, finite size and finite field effects cause τ to deviate from power law behaviour. In the small range between ϵ_z and ϵ_γ, the scaling of τ is most prominent because it is the only quantity which shows power law behaviour.

The following simple analysis allows an estimate to be made for the limiting correlation length, ξ_{sat}. We write:

$$\xi = \begin{cases} \xi_o \epsilon^{-\nu} & \epsilon > \epsilon_z \\ \xi_{sat} & \epsilon << \epsilon_z \end{cases} \tag{4.16}$$

An ansatz to interpolate between these two extremes is:

$$\xi = \frac{[\xi_{sat}][(\xi_o \epsilon^{-\nu})]}{[(\xi_{sat})^\kappa + (\xi_o \epsilon^{-\nu})^\kappa]^{\frac{1}{\kappa}}} \tag{4.17}$$

where κ is a mixing exponent the size of which sets the range of reduced temperature over which ξ goes from power-law behaviour to its saturated value. The size of this exponent is related to the distribution of length scales that act to saturate ξ. Eq.(4.17)

is then substituted into eq.(4.12) in place of $\epsilon^{-\nu}$ in order to fit the τ data all the way to T_c. Using the previously fitted value of z and τ_o, the data analysed fits quite well with κ=2.7 and $\frac{\xi_{sat}}{\xi_o}$=730. This fit is shown in figure 4.10. Assuming a value of ξ_o of a single lattice space ($\approx$3Å), the value for ξ_{sat} for the data in fig.(4.8) is about 219nm or 730 lattice spacings. According to a STM survey of the substrate surface, the average step terrace width is 500$\pm$50 lattice spacings. The similarity of these length scales suggests that the correlation length is limited by the atomic steps of the surface.

The authors wish to thank Martin Grant of McGill University for useful discussions. The authors wish to acknowledge the many technical contributions made by Marek Kiela. This work was supported by the National Science and Engineering Research Council of Canada.

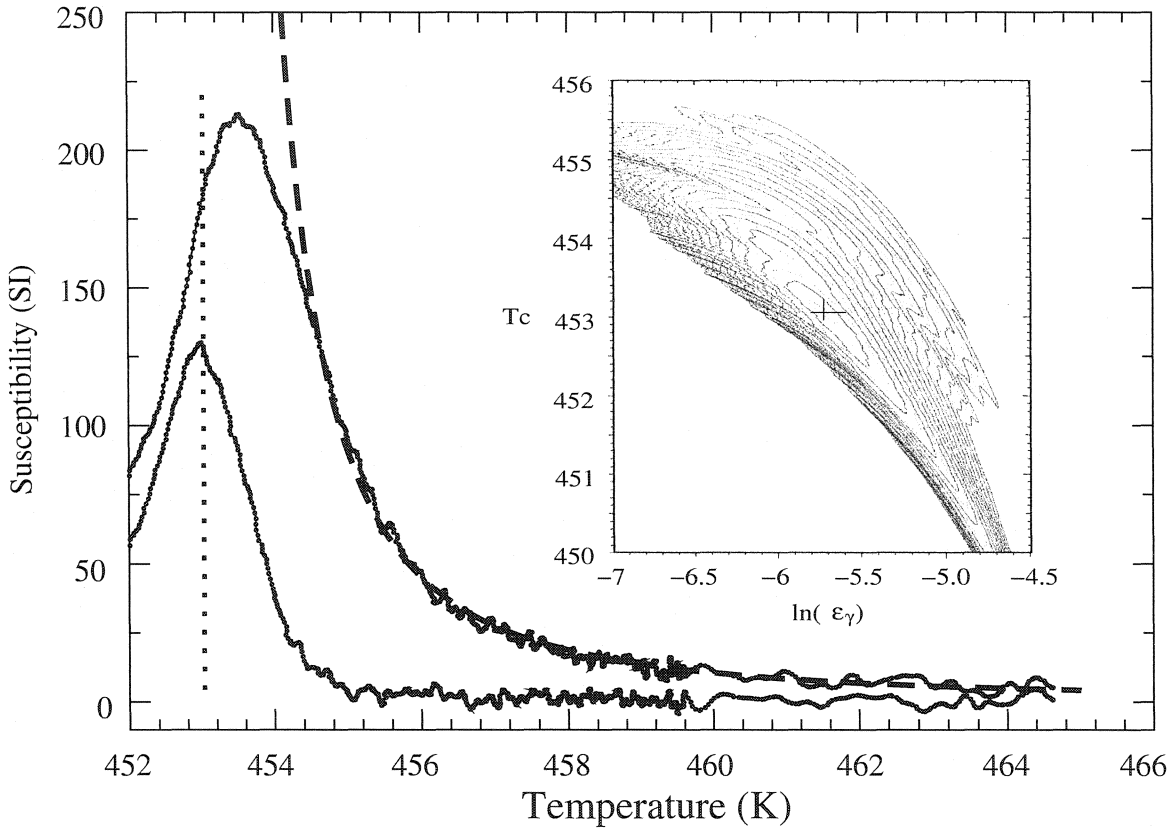

Figure 4.8: Plot of the real and the imaginary components of the complex magnetic susceptibility measured from a 2ML Fe/W(110) film. Dashed atop the real susceptibility shows power-law fit used to extract the value for γ and the dotted line shows the position of T_c=453.03. The inset shows contour plot of the variance of the critical fit as a function of T_c and the cutoff value of $\ln(\epsilon)$. Solid contours are separated by variance levels of 2×10^{-4}.

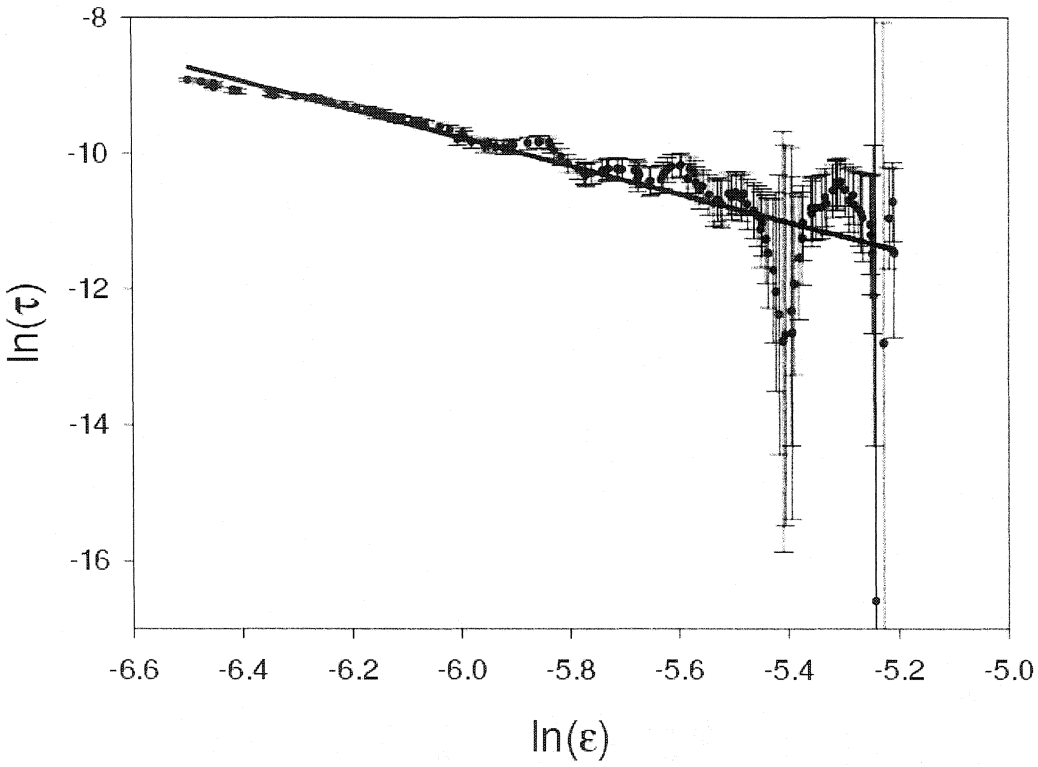

Figure 4.9: Double log graph of the τ plotted against the reduced temperature ϵ. A linear fit is shown over a small temperature range between $\ln(\epsilon)$ values of -6.51 and -5.26.

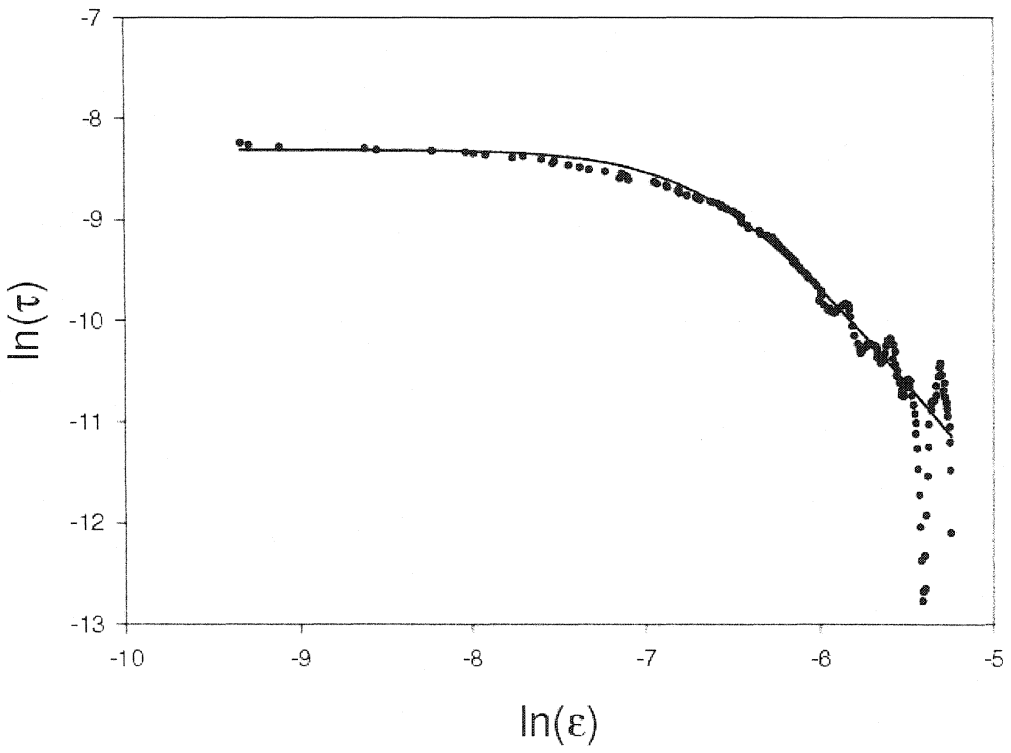

Figure 4.10: Double-log plots of the relaxation time (τ) plotted as a function of reduced temperature. Solid line shows the fit including both power-law scaling effects as well as saturation.

4.2.1 Saturated Effects in the Real Susceptibility

This subsection contains analysis of the real susceptibility that had to be edited from the submitted paper from the previous section for length considerations. However, it is considered part of the complete analysis of the susceptibility data.

Once τ has been completely fit and values for ξ_{sat} and κ have been found, we can turn our attention back to the real susceptibility and model saturation processes there. The saturated τ is insufficient to explain the effect here. $\chi^{'}$ saturates at a temperature slightly higher from T_c than the relaxation time, as shown in figure 4.11. The reason for this is due to the fact that the real susceptibility is affected by dynamical effects from the $(1 + (\omega\tau)^2)$ term in the denominator of equ.(4.14). This term does not affect the relaxation time as it cancels in the taking of the ratio of the complex susceptibility.

To improve the model for the real susceptibility, an ansatz mixing equation similar to equ.(4.17) was used to modify the intrinsic susceptibility to include saturation effects not included in the saturation of τ (such as finite field effects). We find:

$$\chi'_{dyn} = \left(\frac{[\chi_{sat}][\chi_o \epsilon^{-\gamma}]}{[(\chi_{sat})^{\kappa_2} + (\chi_o \epsilon^{-\gamma})^{\kappa_2})]^{\frac{1}{\kappa_2}}} \right) \times \left(\frac{1}{1 + [\omega\tau(T)]^2} \right) \tag{4.18}$$

where χ_{sat} is a constant equal to the maximum value of the static dc-susceptibility (which, as it would be free of dynamic effects, should have a higher value than the ac-susceptibility maximum) and κ_2 is the mixing exponent for the intrinsic susceptibility. All other terms keep their values from previous steps in the fitting process. To model the real data successfully, a mixing exponent $\kappa_2 = 1.75$ is used. Like the fitting for the saturated relaxation time, κ_2 sets the curvature of the "knee" in the double-logarithmic data. The value found is almost half of the mixing exponent κ used for modeling τ, which is perhaps indicative of a wider distribution of effects occurring

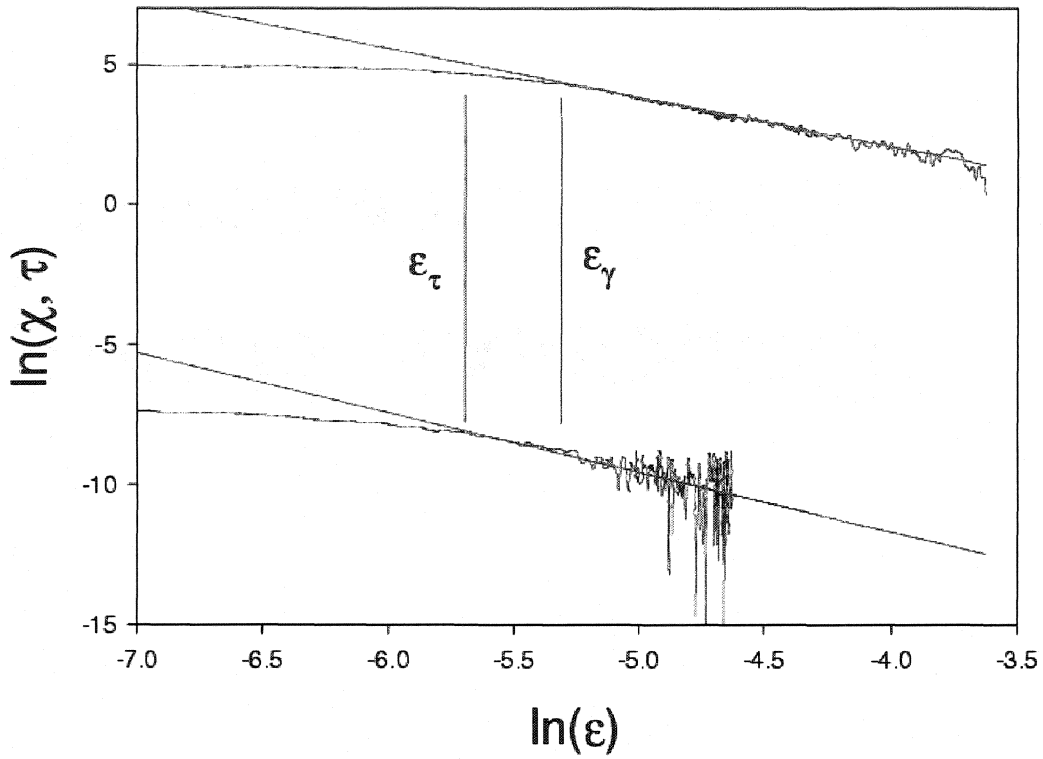

Figure 4.11: Log-log plots of the real susceptibility (top) and the relaxation time (bottom). Vertical lines show where linear power-law behaviour is lost. Note that the relaxation time fits closer to T_c due to the lack of dynamic effects.

than for the finite size effects. Figure 4.12 shows the complete fit (dashed line) for the real susceptibility, giving a value for χ_{sat} of 260, which is about 50SI units higher than the maximum of the ac-susceptibility peak. This is typical for the 400Hz measurements. The 150Hz measurements give a χ_{sat} value 35SI units greater than the ac-susceptibility peak. This is in keeping with the systematics that arise from equ.(4.14), where it can be seen that a higher value of ω will reduce the measured value of the peak more than for lower frequencies. Fitting lower frequency measurements was attempted to try and extend this trend further, but it was found that these were of insufficient signal-to-noise to allow meaningful analysis of the relaxation time.

If the fitting numbers are correct, then it should be possible to fit the imaginary part with no new parameters. Most of the fitting of the complete dynamic susceptibility has involved the use of the real susceptibility with the imaginary part used only in the ratio for the relaxation time. Even though the imaginary part does constitute part of the previous fit, only a small range of it is useful for the critical slowing down analysis (maybe 2 or 3 degrees out of the entire range of data). Figure 4.12 shows the imaginary data compared to the model which consists of the real susceptibility multiplied by $\omega\tau(T)$, as per eq.(4.14). The model is found to fit extremely well except for temperatures within a half-degree of T_c. The divergence of the fit to the data so close to the transition temperature is not surprising given the complexity of a system undergoing a phase transition and the fact that the model being used is based entirely upon linear response theory. It is possible that the data could be fit even closer to T_c with the inclusion of higher order terms in the relaxation model or with the inclusion of a distribution for the effective value for T_c. However, given the complexity of fitting the data to the present model and the already high number of terms that need to be fit, such a model would be too difficult to use with only the present data. As for the imaginary part, it is seen that it fits extremely well for temperatures above T_c, providing further proof for the significance of the relaxation model used to describe the data.

For complete fits for all of the complex susceptibility data sets used in section 4.2, see figure A.2 in appendix A.

4.2.2 Critical Slowing for Films Less than 2ML

The previous sections have dealt with critical slowing down only in 2ML films. As figure 4.6 shows, 2d Ising behaviour is seen in films with a thickness of iron less than that value.

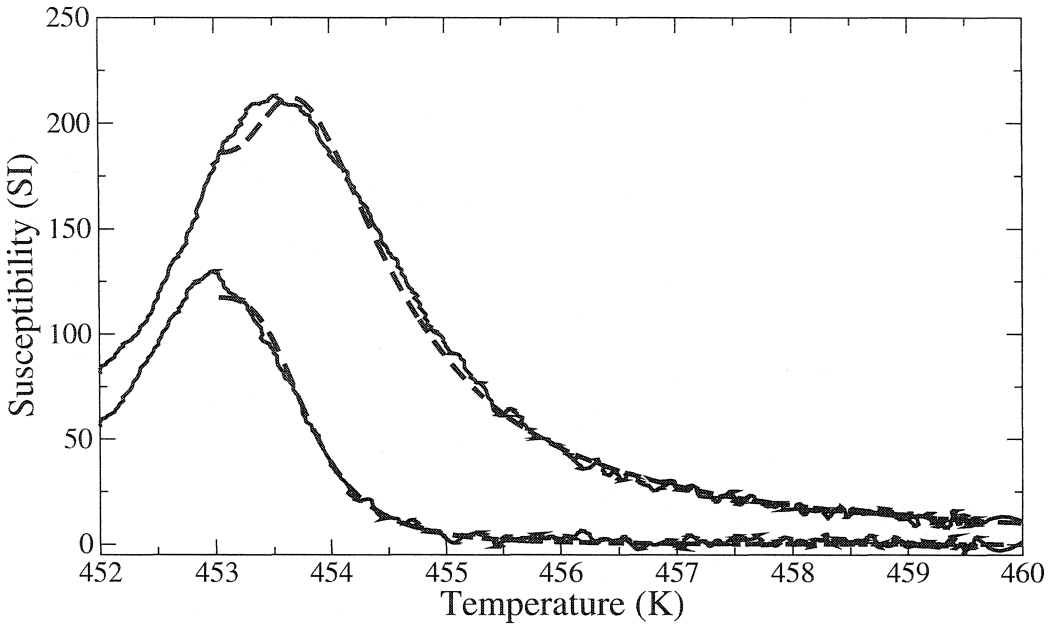

Figure 4.12: Log-log plots of the real susceptibility (top) and the relaxation time (bottom). Vertical lines show where linear power-law behaviour is lost. Note that the relaxation time fits closer to T_c due to the lack of dynamic effects.

Since fitting data for $z\nu$ occurs over such a small range of temperature data, the analysis for the critical slowing down requires much higher quality data that the analysis for the static susceptibility exponent γ. As such, it was not possible to extract a significant value for $z\nu$ for each measurement shown in figure 4.6. However, results exist for some of those films as well as for films where the fitted value for γ does not indicate 2d Ising behaviour.

Fig 4.13 shows a graph of the fit value for $z\nu$ plotted as a function of the fitted value of γ for the same data set. There is clear clustering at $z\nu$ just greater than 2.0 for films that give a value of γ near 1.75. Films with higher values of γ also show (with one exception) higher values for $z\nu$. This is most probably due to the same reason given to explain this behaviour in the γ fits, that of the presence of a wider distribution of transition temperatures in the sample. The same effect there

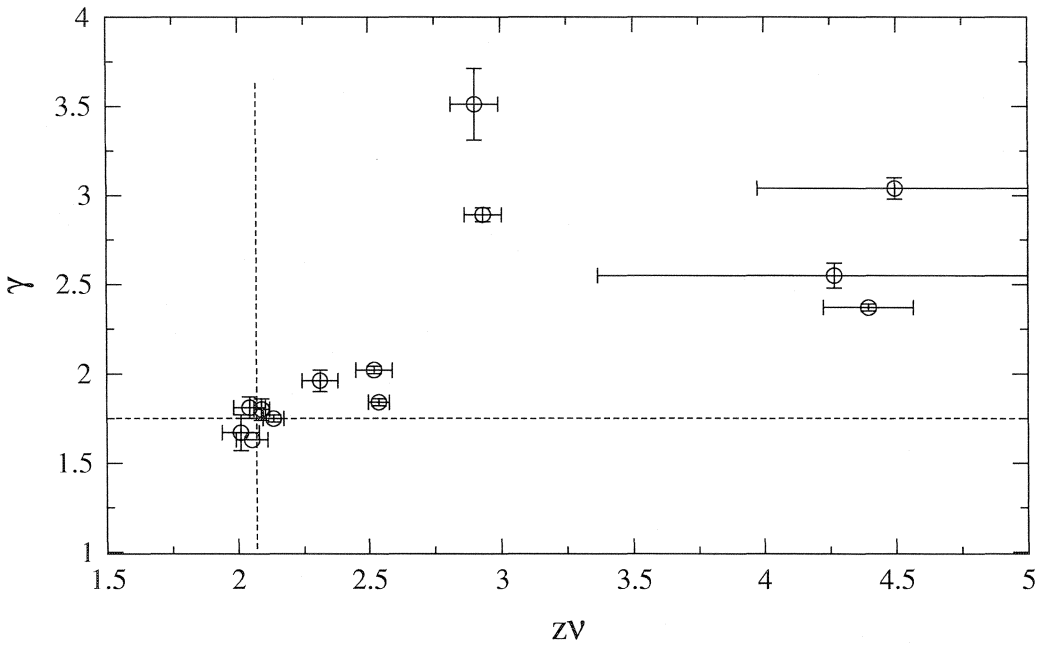

Figure 4.13: Graph showing fitted values for $z\nu$ plotted against the fitted value for γ from the same susceptibility measurement. The horizontal dotted line shows the 2d Ising γ value of 7/4 while the horizontal line shows the average value for $z\nu$ found in section 4.2.

that should lead to higher values of γ will have the same effect here. Indeed, as the value of T_c used to reduce the temperature data for the dynamic exponent fits comes from the static fitting analysis, it is not surprising to see the trend shown in the figure.

4.3 Effects of O_2 Surface Doping

This final section of results will deal with the effects that doping the tungsten surface with oxygen prior to deposition has on the magnetic properites of the film. It will be shown that while small amounts of oxygen do not adversely affect the critical properties of the system, they do have a pronounced effect on the saturation of the magnetic susceptibility. As well, the presence of small amounts of oxygen can give rise to a change in the features of the magnetic susceptibility below T_c, but in a way

that may perhaps be counter-intuitive.

4.3.1 LEED Reconstruction

The presence of oxygen on the W(110) surface will give rise to a 2x2 reconstruction LEED pattern once the oxygen coverage reaches approximately 75% of the surface[47], as can be seen in figure 3.12a. This 2x2 pattern will still be visible for higher coverages of oxygen as some coexistence between the 2x2 phase and a pseudomorphic phase will occur [47]. In the films grown for this thesis, a 2x2 pattern can be seen once the initial iron monolayer has completed even if there is a small amount of oxygen present on the surface prior to deposition. This differs from any previous study of the Fe/W(110) system, which is pseudomorphic for thicknesses up to 3ML[76].

It is known from published studies that iron film growth on the W(110) surface proceeds via *step-edge growth* [78], which means that since iron prefers deposition sites at step edges, further growth tends to proceed outward from these sites. If there is oxygen on the surface prior to deposition, it is assumed that the iron, growing from the step edge, will proceed to "sweep" the oxygen atoms forward into regions of high oxygen concentration (see schematic representation of this in figure 4.14). This will give rise to concentrated islands of oxygen whereas before the oxygen would have been randomly dispersed across the surface.

Given the method of flashing used to clean the tungsten surface prior to deposition, the amount of oxygen at the surface before deposition is typically very small. To test for the presence of oxygen, the surface was flashed several times and then the Auger spectrum for oxygen was measured. Oxygen only has Auger features at a relatively high energy 520eV[79], which means that the signal will be very small. Figure 4.15 shows that Auger peak for oxygen after one flashing cycle, the peak after several more flashes, and finally the peak after the iron deposition.

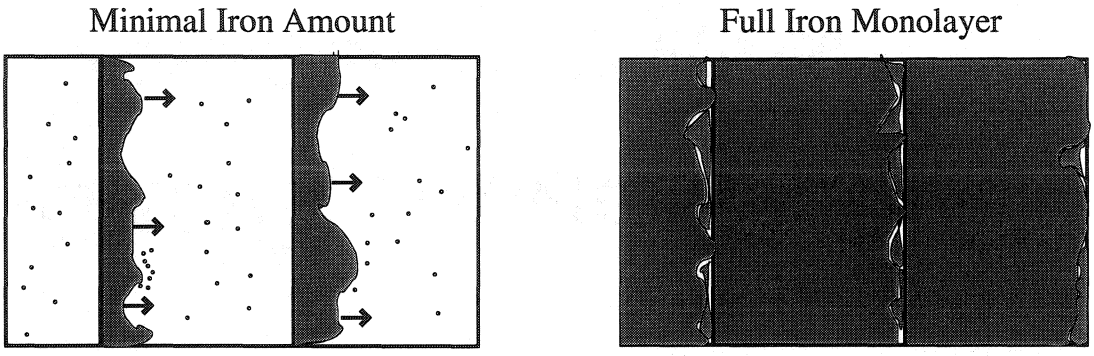

Figure 4.14: Diagram showing how step flow growth can "sweep up" oxygen atoms into small concentrated areas located near step edges. Red areas represent iron, blue areas represent oxygen. Left figure shows small iron amount, right figure shows completed monolayer.

An analysis of this data shows that while the oxygen signal was reduced after the multiple flashing cycles, there is still strong evidence that some oxygen is still present. The size of the oxygen signal after the deposition of 1.2 ML of iron is about 65% as big as the signal before Fe deposition. The amount of attenuation of the oxygen signal is in keeping with the attenuation of the tungsten Auger signal after it is covered by one iron monolayer (usually 60%). This is strong evidence for the fact that the oxygen remains on the surface of the tungsten and is not mixing with or "floating" to the top of the iron.

Figure 4.16 shows the LEED pattern captured at several stages on the deposition of the 1.2ML iron film. To the right of each pattern in the figure, there is an intensity profile for the horizontal distance between the two top primary diffraction spots. The first pair shows the clean surface (the right intensity peak is artificially reduced due to a small occlusion of the spot due to the presence of Helmholtz coils on the sample holder and because of a slight misalignment of the crystal which affects the averaging of the intensity) and a strong 1x1 pattern and narrow, intense

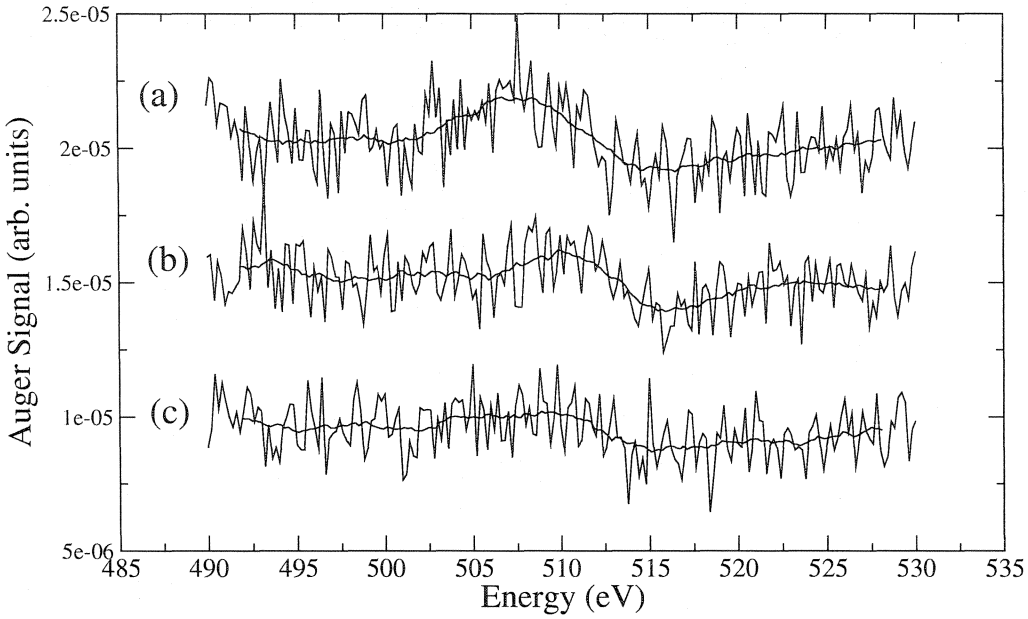

Figure 4.15: Three Auger spectra taken (a) before flashing the substrate (b) after flashing and prior to iron deposition (c) after iron deposition. Solid line represents 15 point running average of the data. Auger spectrum taken after deposition is evidence towards no oxygen leaving the tungsten surface.

diffraction spots. This, along with the Auger spectrum, indicates very low levels of contamination.

The second pair shows the results after 0.5ML of iron has been deposited. The 1x1 pattern remains, as would be expected for the pseudomorphically growing iron film. The LEED spots are now much dimmer and have a larger half-width, which is expected as the iron is at an insufficient coverage to percolate into a regular diffraction grating for the electrons.

The third pair shows the results after another 0.3ML of iron has been deposited for a total of 0.8ML. The image is still primarily 1x1, although there is evidence of the beginning of an extra 2x2 spot starting to emerge. The fact that the iron coverage is now above the percolation limit (typically between two-thirds to three-quarters of a monolayer) means that the diffraction spots profiles are much

narrower again.

The fourth pair shows the results from 1.2ML. A strong 2x2 pattern has emerged, in strict contrast to the 1x1 pseudomorphic pattern one expects from Fe/W(110) films. The primary spots are again diminished in size, due to the extra second layer islands atop the now complete first monolayer. The only possible source for the extra reconstruction spots is the oxygen atoms. While it is possible the iron atoms are forming oxides with the oxygen atoms, the most likely cause for the reconstruction is that the oxygen atoms are gathering together, most probably near step edges due to the step-edge growth nature of iron. The argument against oxide formation is that once the iron is flashed off the surface, the oxygen atoms remain behind.The dense islands of oxygen would then take the 2x2 pattern that has been observed for dense oxygen coverage. Figure 4.17 shows the configuration of atoms that will produce a 2x2 pattern. A LEED experiment was performed to test whether step edge density is a factor in the appearance of the 2x2 pattern. The density of steps on the surface was measured using surface tunneling microscopy in two places: in the center of the crystal and near the edge. The edge of the crystal should have a greater density of steps due to the mechanical polishing process.

Figure 4.18 shows STM images taken from the edge of the crystal and the middle of the single crystal region where all film growth is centered and measured. The scans were performed in atmosphere and the area of both scans is 1μmx1μm. The light bands seen in the images are the atomic step edges of the surface. Several scans were taken from both areas of the substrate (some scans over smaller areas) and the average step width was measured to be 150.1 ± 15nm for the center area and 87.5 ± 18nm at the edge. This is a difference of about a factor of two. The distance between the two areas is approximately 3mm.

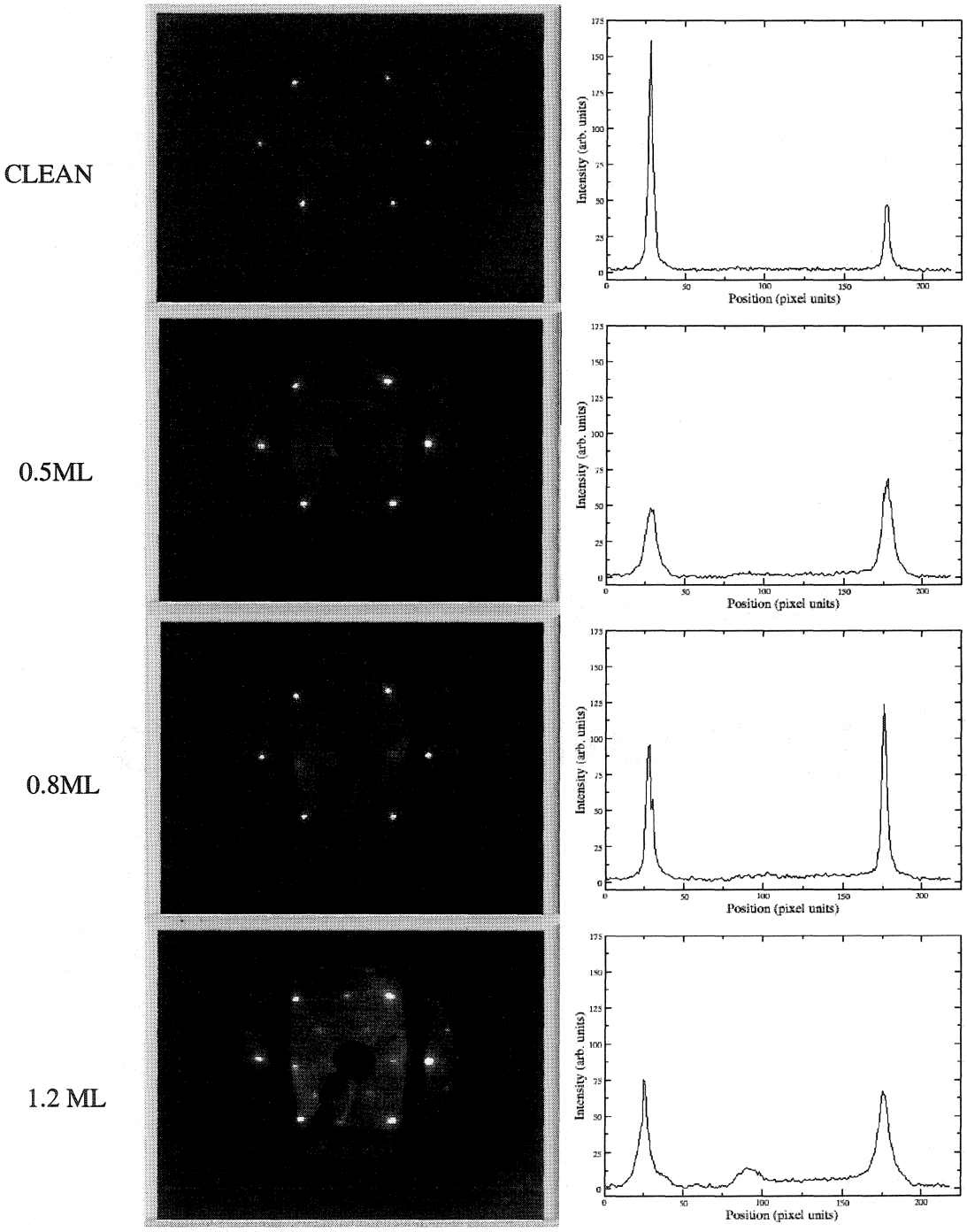

Figure 4.16: Four LEED pictures taken for clean W(110) and then for each additional iron deposition. LEED patterns show 1x1 pseudomorphic behaviour until the completion of the first monolayer, after which a 2x2 pattern is clearly observed.

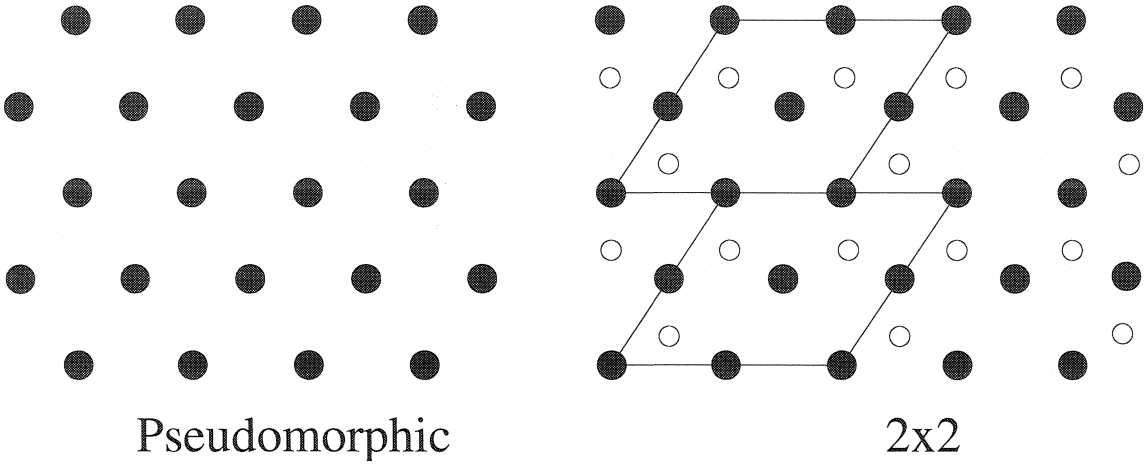

Figure 4.17: Diagram of atoms that give rise to pseudomorphic (left) and 2x2 (right) LEED patterns. Black dots represent tungsten atoms, white circles represent oxygen (size not to scale). Parallelogram represents new unit cell.

An iron film was grown over the two areas and the LEED pattern was observed. The film thickness was 1.5ML. The width of the electron beam used for LEED experiments is slightly less than 1mm. This width is important as the resulting diffraction pattern will blend in effects that happen on a length scale smaller than that. The substrate had been flashed only once prior to deposition, ridding the surface of all contaminants except for the stable oxygen atoms. This was confirmed by examining an Auger spectrum that showed a small feature that gave evidence of the oxygen present.

LEED images were recorded for positions along the center z-axis of the film in 1mm increments (starting at z=27.5mm which corresponds to the crystal edge and proceeding to z=30.5mm corresponding to the crystal center). Figure 4.19 shows the LEED profiles between the lower two primary diffraction spots. At z=27.5mm, there is only the slightest evidence of an extra 2x2 spot. If the scan at z=27.5 is normalised for the primary spots to the scan at z=30.5, the 2x2 spot appears to be of equal size and width (see inset of figure 4.19). This would indicate that the step-edge density,

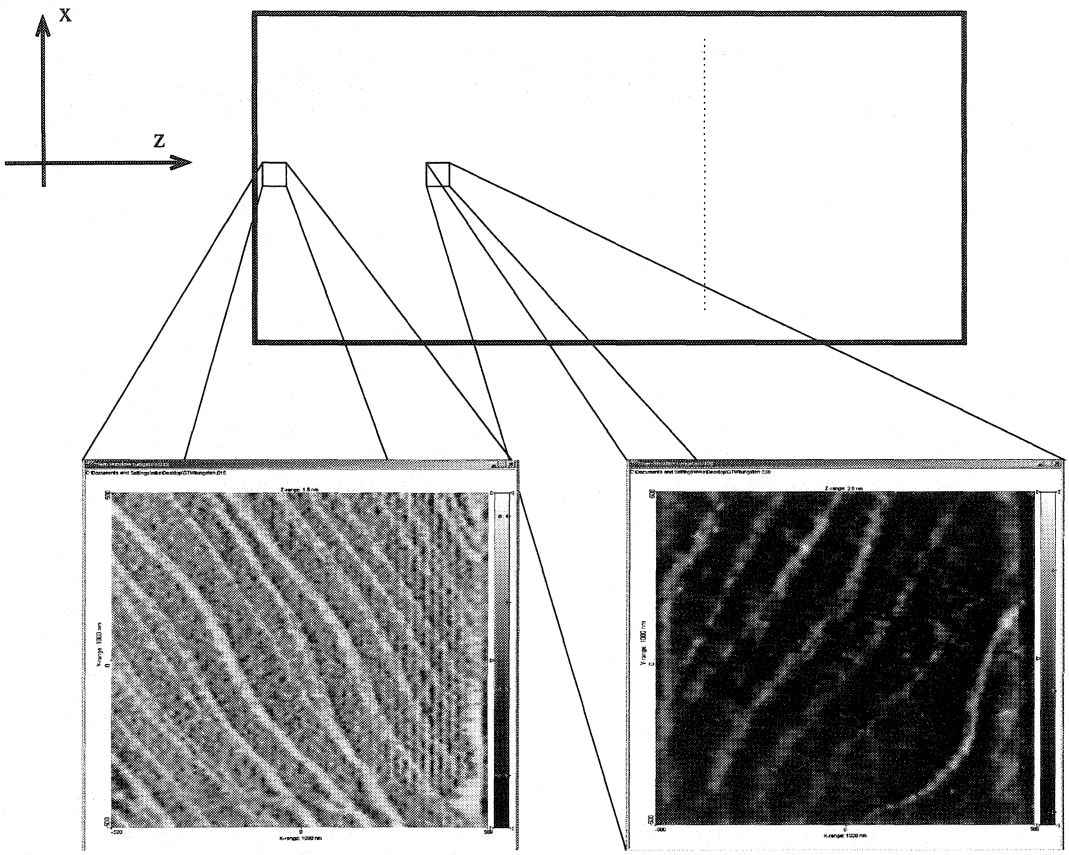

Figure 4.18: STM images taken from the edge of the substrate and the middle of the single-crystal area. Dotted line shows relative position of the grain boundary. Area of STM scans in both cases was $1\mu m^2$.

at least to this scale, does not affect the reconstruction.

The implication for the model is that the step edge density has no obvious effect on the oxygen reconstruction, at least for these small levels of ovygen doping.

4.3.2 Effects of O_2 Doping on Magnetic Measurements

There is some evidence that oxygen is concentrated at step edges in the magnetic susceptibility measurements. These measurements also show what appears to be a feature that is dependent not on the presence but rather on the *absence* of oxygen.

A pure iron film will show a susceptibility peak at the Curie transition, as

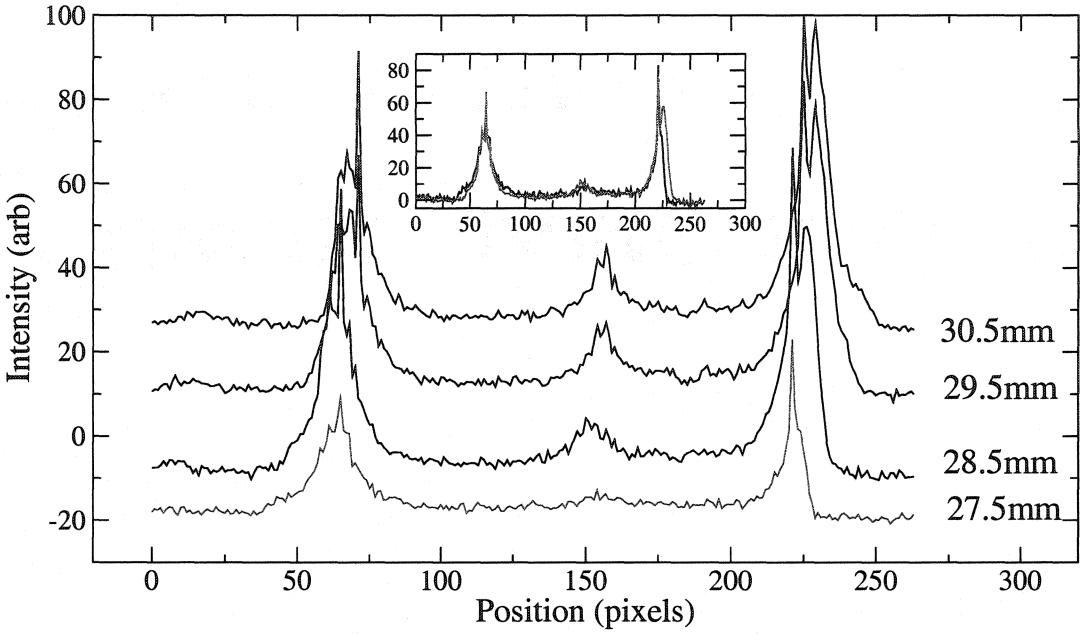

Figure 4.19: LEED profiles between the two principle LEED spots shown as a function of position on the surface. Profile in red was taken as close to crystal edge as possible while the topmost profile is from crystal center where most measurements are made. Inset shows profiles from z=30.5 (black) and z=27.5 (red) renormalised to the primary peaks.

evidenced by the successful critical analysis for temperatures above the peak (as seen in sec. 4.1), the loss of magnetic hysteresis, and the fact that the peaks coincide with critical temperatures reported in the literature (see reference [55] for an interesting study of T_c vs iron thickness for this system). The critical exponent measured seems not to be affected by the presence of oxygen. The data represented in figure 4.6 is a mixture of films that have or do not have small amounts of oxygen present on the surface. At temperatures less than the peak, the story changes. It is found that for temperatures less than T_c, the susceptibility shows a "bench" or sometimes a secondary peak.

Figure 4.20 shows the real magnetic susceptibility measured from a 2ML pure iron film, in fact the same film for which measurements of the critical slowing down

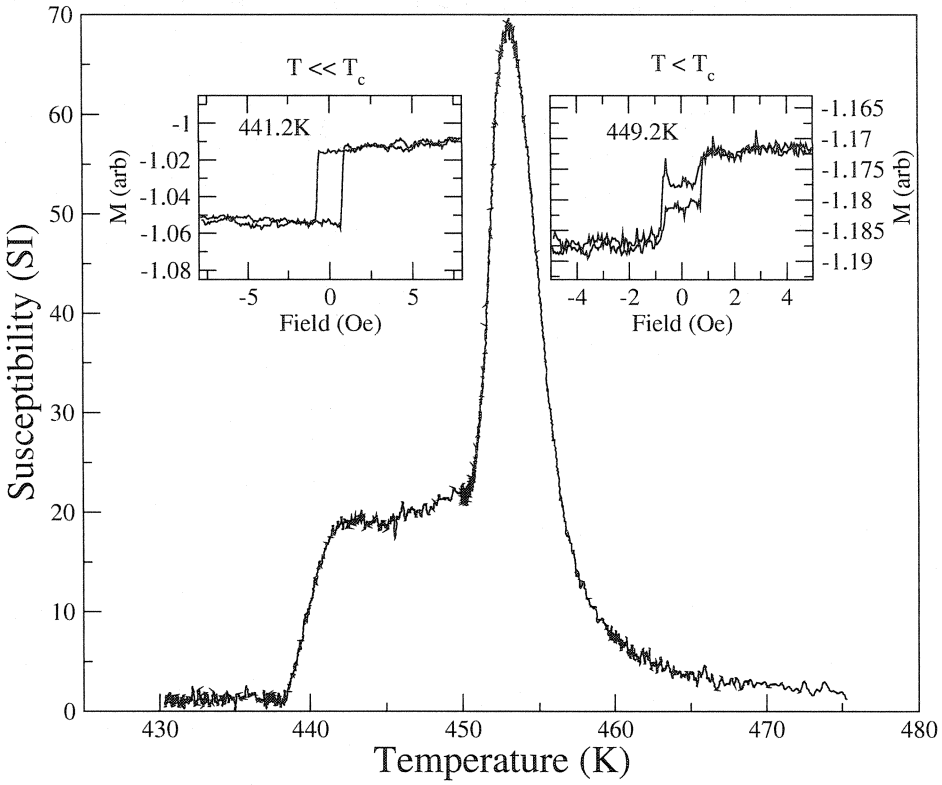

Figure 4.20: Real magnetic susceptibility measured from a pure 2ML iron film. Unexpected bench feature on the low temperature is assumed to be related to domain processes. Inset graphs show hysteresis loops measured from the same film. Precise temperture relationship between loops and susceptibility is not assured as the time taken between measurements was sufficient for changes in the temperature of certain features.

were taken. The transition temperature for this data is approximately 452K. Just below 440K, the susceptibility begins to rise to about 20SI units and stays more or less constant up to about 445K, where it slowly increases until 450K where the major peak occurs. The major peak is due to the Curie transition as the peak coincides with the predicted value of T_c for this film. The insets to the figure show two hysteresis loops taken before the susceptibility measurements. The time between loop and χ measurements, as well as the repeated thermal cycling that occurs in all measurements, makes comparing temperatures between the loops and the susceptibility

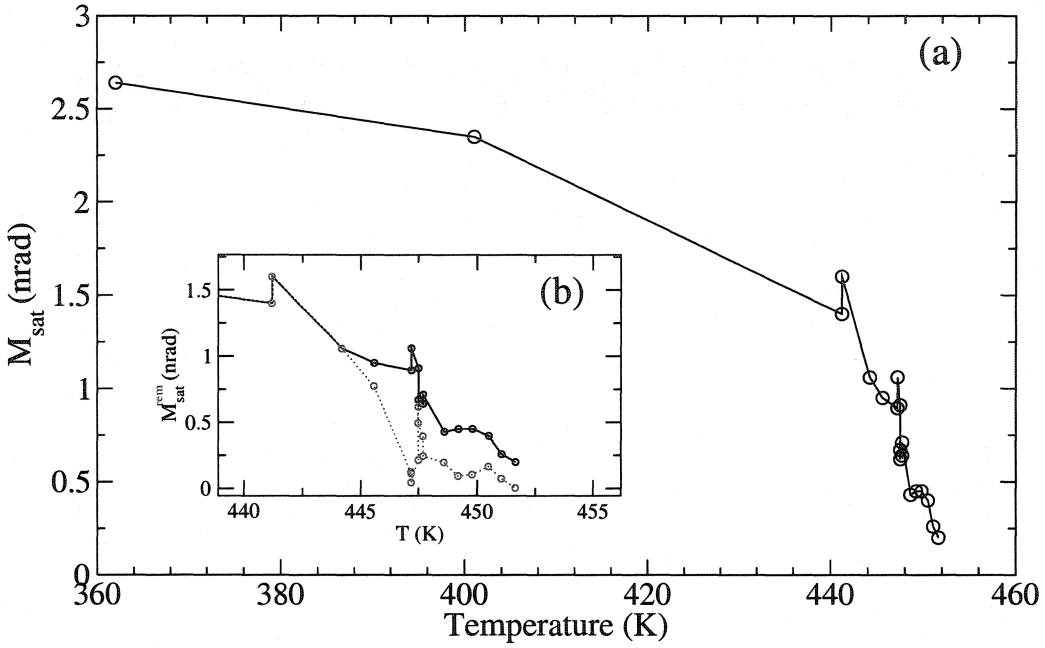

Figure 4.21: Figure (a) shows the saturated magnetisation (m_{sat}) measured from hysteresis loops as a function of temperature. (b) shows m_{sat} (black) plotted close to T_c with the remenent magnetistion m_{rem} (blue).

difficult to do precisely. The loop measured at 441.2K appears to be a standard narrow rectangle shape one expects from a ferromagnet near the transition. The loop measured at 449.2K however shows much different behaviour. There appears to be an inner loop with a small hysteresis. The inner loop has a coercive field just under 1Oe, which is smaller than the applied field of the susceptibility measurement, which was about 2.1Oe in this data. The high field is why the susceptibility maximum is less than expected, a trend shown in figure 4.2. The form of the hysteresis loop is surprisingly stable over a range of 10K, indicating that something besides typical ferromagnetic hysteresis is at work. The bench also appears in the imaginary part of the susceptibility, is very reproducible and shows no obvious hysteresis on small temperature cycling around the temperature where it first appears.

Some type of extra feature (like a bench or a small, secondary peak) appears

whenever the substrate has been rigourously cleaned of oxygen and the resulting LEED pattern of the final film was pseudomorphic. Also, it has been found that these features always appear just below the Curie transition, indicating that their origin is likely tied to the weakening magnetic interactions. The loop measured at 449.2K in figure 4.20 shows a two-step moment reversal with magnetic remenence less than the value of the saturated moment (see figure 4.21), as if some significant portion of the sample has its net magnetic moment nulled at zero field. In these loops, it requires a field of about 0.5Oe to see a response in the magnetisation. The field required to see this will be referred to as H_α.

The possiblity that some part of the film has its moment aligned in a direction away from $[1\bar{1}0]$ was checked by measuring χ along orthogonal to the assumed easy axis, [001] (in-plane) and [110] (perpendicular). It was found that these measurements always showed zero signal, indicating that no moment existed along those directions.

This two-step state is the reason why the secondary feature is seen in the susceptibility data. For a susceptibility measured in a field larger than H_α, the magnetisation will have the ability to trace the major loop and thus see a greater magnetic response than one would in a more typical ferromagnetic material where the coercive field is usually much higher, especially at temperatures so far below T_c. In these films at some temperature T^*, the remenent magnetisation (m_r) becomes less than the saturated magnetisation (m_s).

It is hypothesized that the reason behind this phenomenon is due to the system breaking up into Ising domains near the step edges. In the middle region of the film away from steps, the magnetisation is in large domains (if not in a single domain). Near the steps, local anisotropy effects may cause the system to break up into smaller domains. Complicated and interesting anisotropy effects have been seen

at step-edges in the Fe/W(110) system [57, 80]. Domain walls are easily moved at high temperatures as long as they are not pinned by some local inhomogeneity. It has been found in Fe/W(110) films just larger than one monolayer that domain walls near step edges are pinned at the regions where there are small second layer islands[81]. It has also been suggested that similar pinning will occur to a lesser degree for two mononlayer films with small third layer growth islands [81]. It is probable that, since the film grows from the step-edge out, that there are more third layer islands, and therefore more pinning centers, at the step edge. The pinning of the walls is slight enough that only small fields on the order of what is observed for H_α is required to break it. This hypothesis continues by saying that the presence of a small amount of oxygen at the step may ameliorate any thickness perturbation. It may also be possible that if there is oxygen at the step edge before the iron is deposited, it will lessen the step anisotropy contributions and therefore prevent the creation of the domains.

4.3.3 Effects of O_2 Doping on ξ_{sat}

The effect of oxygen surface doping on the analysis for ξ_{sat} can be seen in table 4.1. While not stated in the submitted paper, the measurements made at 150Hz were made on an oxygen doped film and the 400Hz measurements were made from a pure iron film. The presence of small amounts of oxygen was found to have no effect on the film's critical properties, as seen by the fact that both films used in the critical slowing down analysis exhibit the same critical exponents. The difference arises in the values of ξ_{sat}.

The pure iron film measurements show a larger value of the saturated correlation length, supporting that idea that the oxygen presents a barrier to the spin fluctuations at the critical point. The value of about 750 lattice spaces (approximately 225nm) is the same order of magnitude as the step edge spacing as noted in section

4.2. However, the oxygen-doped films show a ξ_{sat} of about 450 lattice spaces (app. 135nm) which is almost exactly in agreement with the average step edge distance of the crystal. This gives some further circumstantial evidence towards the oxygen gathering at step edges on the surface.

The limited distance due to the oxygen means that ξ is artificially curtailed as it diverges at T_c. As such, the power law scaling of the relaxation time should not extend as close to the Curie temperature as it would for a pure film. An examination of the power law cutoff for the two films shows that the average value of ϵ_z for the pure iron film is about -6.5 and is about -5.8 for the oxygen-doped films.

The mixing exponent for τ, κ, for all four measurements is 2.7±0.1, which indicates that the crossover from power-law scaling and saturation for both types of film occurs in a similar fashion. This may mean that step edges still play a role in the saturation of the correlation length in the pure films, but the effectiveness of ther barrier is lessened and may be the case that more than one step edge is required to dampen the fluctuation.

4.3.4 Effects of O_2 Doping on χ_{sat}

As stated earlier, χ_{sat} can be thought of as the amplitude of the dc-susceptibility. The susceptibility is related via the correlation function to the correlation length of the critical spin fluctuations and as such, given the limiting effect oxygen has on the diverging correlation length, it should come as no surprise that the oxygen doped films also show a smaller value for χ_{sat}.

The relationship between the two saturated quantities χ_{Sat} and ξ_{sat} is difficult to establish numerically, but the trend that this simple model shows does work in the proper way. An increase in the saturated correlation length is directly related to an increase in the saturated value of the real susceptibility. Both measurements made

from the 150Hz film shows a value of χ_{sat} of 195SI, but with two different values for the mixing exponent κ_2. One measurement has κ_2 equal to 1.75 while the other set at 2.0. The reason behind the change is unclear, especially since the mixing exponent used for modeling the correlation length was almost the same for both measurements. The 400Hz measurements show χ_{sat} equal to 260SI with a mixing exponent of 1.75, the same as for one of the 150Hz measurements.

Chapter 5

Conclusion

This thesis has dealt with experimental investigations into phase transitions in ferromagnetic ultrathin films. The two dimensional Ising behaviour of iron bilayers grown atop a W(110) single crystal substrate has been shown using measurements of the complex magnetic susceptibility. A thourough analysis of the real component of the susceptibility shows that the critical exponent of the susceptibility agrees with the theoretical value for the 2d Ising class for certain thicknesses of iron. The analysis algorithm used to find γ also simultaneously found the Curie Temperature T_c, the critical amplitude χ_o, and the range of data that obeyed critical power-law behaviour.

The results show that the susceptibility exhibits a γ value within error of the 2d Ising value of $\frac{7}{4}$ will fit closer to T_c than films that show higher values of γ. It was found that films with a thickness of 2.0ML and 1.5ML will most probably show a power-law behaviour closer to the transition that films with a thickness between those two limits. Susceptibility measurements that show the reduced temperature cutoff of power-law behaviour less than $4.75\text{x}10^{-3}$ gives an average γ value of $1.75\pm.02$.

Further analysis of the complex susceptibility allows the extraction of information on the process of critical slowing down at the phase transition. Measurements of this effect are very difficult and as such, there has been very little experimental

work in the literature on it. Using a linear relaxation model for the susceptibility data, it has been shown that it is possible for data with a high quality signal-to-noise ratio to extract a value for the critical exponent product $z\nu$, where z is the critical slowing down exponent. One fact that makes this part of the analysis possible is the extraction of T_c from the real susceptibility data. The critical exponent z was found to agree with the theoretically predicted value, the first experimental confirmation of this result.

For bilayer films, using two measurements of the complex susceptibility measured from two different films, the critical exponent product of $z\nu$ was found to be $2.09\pm.06$. Since the analysis of γ shows the films to be in the 2d Ising class, the value of ν should be exactly 1.0. Therefore, it is stated that the value quoted for $z\nu$ is in fact equivalent to the value for z. Besides the bilayer films, it was found that any iron film that showed γ near 1.75 also showed a value for z in keeping with the average bilayer value.

Making measurements of the critical exponent at phase transitions is often complicated by saturation effects which spoil the power law divergence near T_c. A simple model has been proposed here to extract the saturated correlation length from the relaxation time data. The results agree with the order of magnitude that is expected for this quantity and also agrees with the size that could be predicted based on the atomic step width that was measured using scanning tunnel microscopy.

The final result of this thesis examines the effect of oxygen doping of the surface on iron film deposition and magnetic properties. The presence of oxygen was found not to affect the critical properties, but it will have an effect on how far the correlation length diverges before being saturated. The oxygen, thought to gather at substrate step edges, was found to restrict the saturated correlation length to a

smaller value (about half) of the length found for pure iron films.

The full list of parameters that have been fit from the complex susceptibility data, including the two diverging quantities χ and τ and the saturated correlation length ξ_{sat} allow the relaxation model to successfully describe the data from the maximum temperature down to T_c, below which the relaxation becomes more complicated with the inclusion of hysteresis effects. The successfully modeled data confirms the significance of the fitting analysis.

Appendix A

Additional Figures and Data

This appendix contains graphs and data which show mostly fits for more sets of data than are shown in the main body of the text. The figures include:

Fig.(A.1) shows the complete τ fits including saturation effects for all four measurements used in sec.(4.2).

Fig.(A.2) shows the complete complex susceptibility fits including saturation effects for all four measurements used in sec.(4.2).

Table (A.1) shows the major fitting parameters from the data plotted in fig.4.13 and fig. 4.6

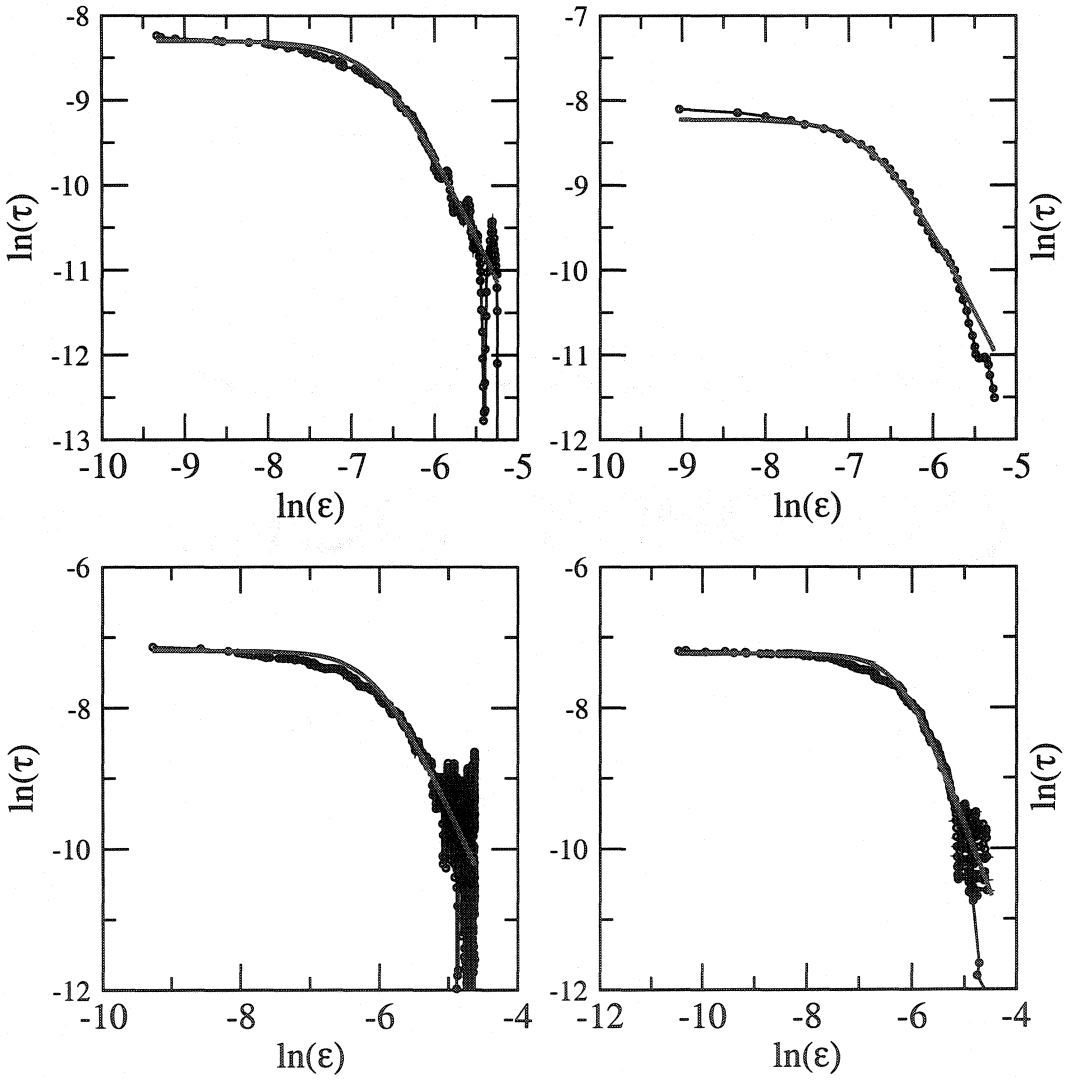

Figure A.1: The complete τ fits for the four susceptibility measurements used in the paper on critical slowing down.

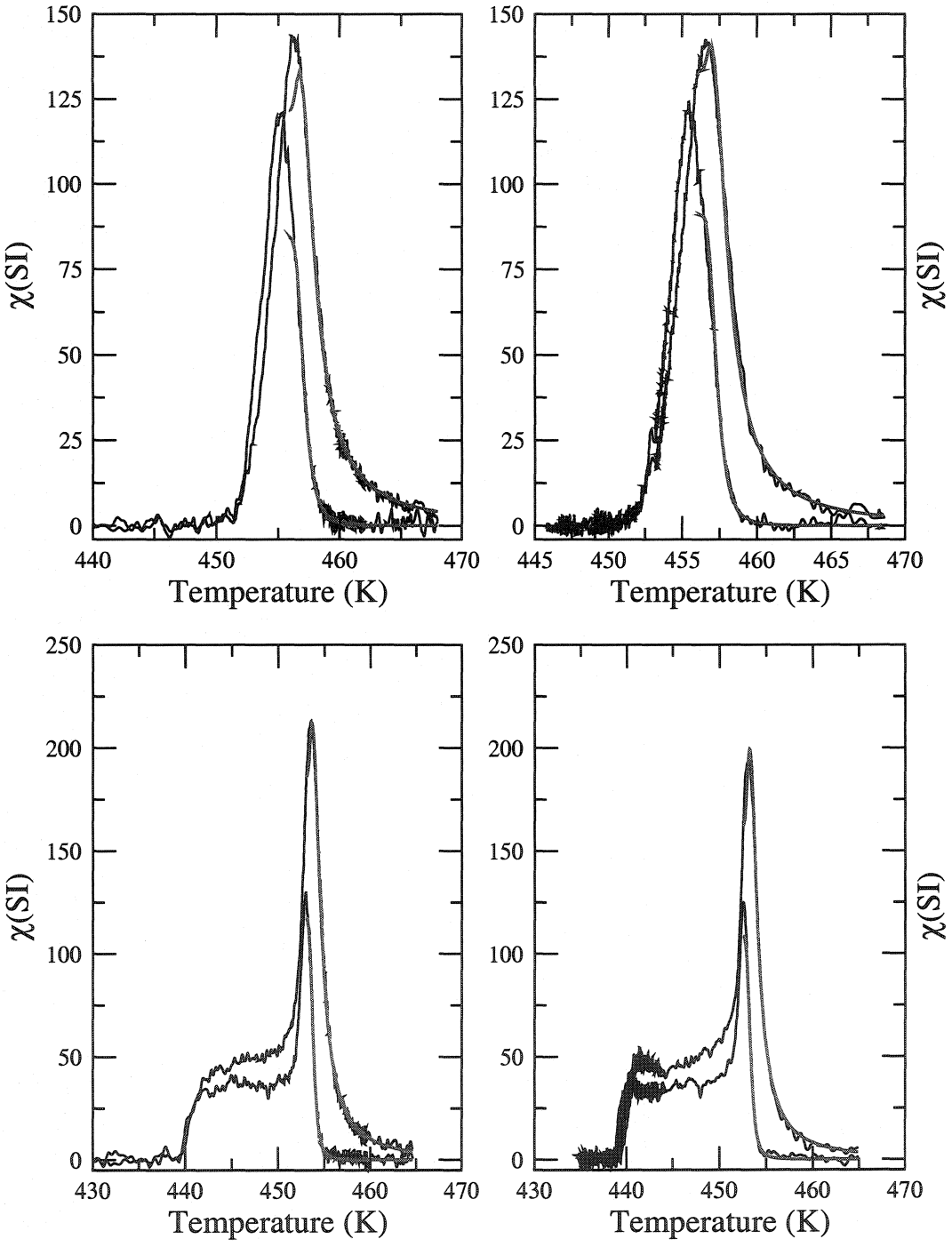

Figure A.2: The complete fits for the four complex susceptibility measurements used in the paper on critical slowing down. Red lines are the fits, black the data. Fits only significant for temperatures above T_c

Table A.1: Fit results for the data shown in fig.4.13

#ML	f(Hz)	γ	χ_o(SI)	$z\nu$	τ_o(s)	T_c(K)
2.0	150	1.75±.02	$7.3\pm.3 \times 10^{-3}$	2.13±.04	$1.7\pm0.3 \times 10^{-9}$	455.84
2.0	150	1.81±.06	$4.2\pm.5 \times 10^{-3}$	2.04±.06	$2.1\pm0.5 \times 10^{-9}$	456.25
2.0	400	1.67±.10	$6.5\pm1.5 \times 10^{-3}$	2.01±.07	$4.0\pm0.3 \times 10^{-10}$	452.49
2.0	400	1.80±.06	$6.2\pm.6 \times 10^{-3}$	2.09±.03	$2.6\pm0.6 \times 10^{-10}$	453.03
1.75	400	2.02±.02	$2.2\pm.1 \times 10^{-3}$	2.52±.07	$2.2\pm0.5 \times 10^{-11}$	435.00
1.75	400	2.37±.02	$5.2\pm.4 \times 10^{-4}$	4.40±.17	$1.97\pm1.1 \times 10^{-15}$	434.40
1.75	400	3.06±.06	$3.6\pm.6 \times 10^{-5}$	4.50±.52	$9.67\pm1.3 \times 10^{-15}$	446.26
1.75	400	2.89±.04	$5.3\pm.6 \times 10^{-5}$	2.94±.07	$1.85\pm0.8 \times 10^{-11}$	447.78
1.75	45	2.55±.07	$2.9\pm.5 \times 10^{-4}$	4.26±.9	$1.67\pm1.0 \times 10^{-13}$	441.83
1.5	150	1.84±.02	$4.3\pm.3 \times 10^{-3}$	2.54±.04	$9.8\pm0.6 \times 10^{-11}$	417.70
1.5	150	1.63±.14	$2.2\pm.8 \times 10^{-3}$	2.05±.06	$7.5\pm0.4 \times 10^{-10}$	415.75
1.4	330	1.96±.06	$1.4\pm.2 \times 10^{-3}$	2.31±.07	$8.0\pm0.6 \times 10^{-11}$	400.67
1.4	150	3.51±.20	$3.1\pm1.3 \times 10^{-6}$	2.90±.09	$2.42\pm0.4 \times 10^{-10}$	397.49

Table A.2: Fit results for the data shown in fig.4.6 that are not included in fig. 4.13

#ML	f(Hz)	γ	χ_o(SI)	T_c(K)
2.0	150	1.66±.10	$4.08\pm2.15 \times 10^{-3}$	456.20
2.0	150	1.67±.18	$3.92\pm2.15 \times 10^{-3}$	455.34
2.0	150	1.81±.06	$4.25\pm0.63 \times 10^{-3}$	456.25
2.0	150	1.79±.28	$1.69\pm1.35 \times 10^{-3}$	457.10
1.75	400	2.52±.07	$2.77\pm0.48 \times 10^{-4}$	447.75
1.75	150	2.51±.04	$2.41\pm0.28 \times 10^{-4}$	446.46
1.75	400	2.79±.06	$7.56\pm1.2 \times 10^{-5}$	434.47
1.5	150	1.42±.02	$2.02\pm0.10 \times 10^{-2}$	416.20
1.4	150	2.31±.14	$3.45\pm1.24 \times 10^{-4}$	402.10
1.4	150	2.43±.16	$1.84\pm.75 \times 10^{-4}$	395.86

Bibliography

[1] KITTEL, C.: *Introduction to Solid State Physics (7th ed.).* John Wiley and Sons Inc., 1996.

[2] COLLINS, M.F.: *Magnetic Critical Scattering.* Oxford University Press, 1989.

[3] RAU, C., G. XING M. ROBERT. *J. Vacuum Sci. Tech. A*, 6:579, 1988.

[4] BALLENTINE, C. A., R. L. FINK, J. ARAYA-POCHET J. L. ERSKINE. *Applied Phys. A*, 49:459–466, 1989.

[5] DURR, W., M. TABORELLI, O. PAUL, R. GERMAR, W. GUDAT, D. PESCIA M. LANDOLT. *Phys. Rev. Lett.*, 62:206, 1989.

[6] SCHNEIDER, C. M., P. BRESSLER, P. SCHUSTER, J. KIRSCHNER, J. J. DE MIGUEL R. MIRANDA. *Phys. Rev. Lett.*, 646:1059, 1990.

[7] LI, Y., M. FARLE K. BABERSCHKE. *Phys. Rev. B*, 41:9596, 1990.

[8] QIU, Z. Q., J. PEARSON S. D. BADER. *Phys. Rev. Lett.*, 67:1646, 1991.

[9] BACK, C. H., CH. WÜRSCH, A. VATERLAUS, U. RAMSPERGER, U. MALER D. PESCIA. *Nature*, 378:597, 1995.

[10] LI, Y. K. BABERSCHKE. *Phys. Rev. Lett*, 68:1208, 1992.

[11] Huang, F., M. T. Kief, G. J. Mankey R. F. Willis. *Phys. Rev. B*, 49:3962, 1994.

[12] Kohlhepp, J., H. J. Elmers, S. Cordes U. Gradmann. *Phys. Rev. B*, 45:12287, 1992.

[13] Farle, M. K. Baberschke. *Phys. Rev. Lett.*, 58:511, 1987.

[14] Stetter, U., M. Farle, K. Baberschke W. G. Clark. *Phys. Rev. B*, 45:503, 1992.

[15] Elmers, H. J., J. Hauschild U. Gradmann. *Phys. Rev. B*, 54:15224, 1996.

[16] Elmers, H. J., J. Hauschild, G. H. Liu U. Gradmann. *J. Appl. Phys.*, 79:4984, 1996.

[17] Arnold, C. S., M. J. Dunlavy D. Venus. *Rev. Sci. Inst.*, 68:4212, 1997.

[18] Rudt, C., P. Poulopoulos, J. Lindner, A. Scherz, H. Wende, K. Baberschke, P. Blomquist R. Wappling. *Phys. Rev. B.*, 65:220404(R), 2002.

[19] Stoner, E. C. *Proc. Roy. Soc*, 169A:339, 1939.

[20] Neel, L. *J. Physique et le Radium*, 15:225, 1954.

[21] Chikazumi, S.: *Physics of Magnetism.* John Wiley & Sons, 1964.

[22] Mermin, N. D. H. Wagner. *Phys. Rev. Lett.*, 17:1133, 1966.

[23] Bander, M. D. L. Mills. *Phys. Rev. B*, 38:12015, 1988.

[24] Erickson, R. P. D. L. Mills. *Phys. Rev. B*, 43:11527, 1991.

[25] SAMUELSON, E. J. *Phys. Rev. Lett.*, 31:936, 1973.

[26] HEINRICH, B. J. A. C. BLAND (ED): *Ultrathin Magnetic Structures vol. I.* Spinger-Verlag, 1994.

[27] HEINRICH, B. J. F. COCHRAN. *Adv. Phys.*, 42:523, 1993.

[28] GAY, J. G. R. RICHTER. *Phys. Rev. Lett.*, 56:2728, 1986.

[29] PESCIA, D. V. L. POKROVSKY. *Phys. Rev. Lett.*, 65:2599, 1990.

[30] KASHUBA, A. B. V. L. POKROVSKY. *Phys. Rev. B*, 48:10335, 1993.

[31] WULFHEKEL, W., F. ZAVALICHE, R. HERTEL, S. BODEA, G. STEIERL, G. LIU, J. KIRSCHNER H. P. OEPEN. *Phys. Rev. B*, 68:144416, 2003.

[32] LINDNER, J., K. LENZ, E. KOSUBEK, K. BBAERSCHKE, D. SPODDIG, R. MERCKENSTOCK, J. PELZL, Z. FRAIT D. L. MILLS. *Phys. Rev. B*, 68:060102(R), 2003.

[33] GAO, C. M. J. O'SHEA. *JMMM*, 127:181–189, 1993.

[34] YAO, Y., H. C. MIRELES, J. LIU, Q. NIU J. L. ERSKINE. *Phys. Rev. B*, 67:174409, 2003.

[35] KLAUI, M., C. A. F VAZ, J. A. C. BLAND, W. WERNDORFER, G. FAINI, E. CAMBRIL L. J. HEYDERMAN. *App. Physics Letters*, 83:105, 2003.

[36] GOLDENFELD, N.: *Lectures on Phase Transitions and the Renormalization Group.* Addison-Wesley Publishing Co., 1992.

[37] HARRISON, W. A.: *Solid State Theory.* Dover Publications Inc., 1979.

[38] KADANOFF, L. P. *Physics*, 2:263, 1966.

[39] WILSON, K. G. *Phys. Rev. B*, 4:3184, 1971.

[40] RUSHBROOKE, G. S. *J. Chem. Phys*, 39:842, 1963.

[41] STANLEY, H. E.: *Introduction to Phase Transitions ans Critical Phenomena.* Oxford University Press, 1971.

[42] ONSAGER, L. *Phys. Rev.*, 65:117, 1944.

[43] HOHENBERG, P. C. B. I. HALPERIN. *Rev. Mod. Phys.*, 49:435, 1977.

[44] HOVE, L. VAN. *Phys. Rev*, 93:1374, 1954.

[45] ZANGWILL, A.: *Physics at Surfaces.* Cambridge University Press, 1988.

[46] KAVELAARS, J.J., private conversation.

[47] JOHNSON, K. E., R. J. WILSON S. CHIANG. *Phys. Rev. Lett.*, 71:1055, 1993.

[48] KOLACZKIEWICZ, J. E. BAUER. *Surface Science*, 144:495, 1984.

[49] HEINRICH, B. J. A. C. BLAND (ED): *Ultrathin Magnetic Structures vol. II.* Spinger-Verlag, 1994.

[50] ARNOLD, C. S. D. VENUS. *Rev. Sci. Inst.*, 66:3280, 1995.

[51] BOVENSIEPEN, U., C. RUDT, P. POULOPOULOS K. BABERSCHKE. *JMMM*, 231:65–73, 2001.

[52] GARREAU, G., M. FARLE, E. BEAUREPAIRE K. BABERSCHKE. *Phys. Rev. B*, 55:330, 1997.

[53] Aspelmeier, A., M. Tischer, M. Farle, M. Russo, K. Baberschke D. Arvanitis. *JMMM*, 146:256–266, 1995.

[54] Gradmann, U. G. Waller. *Surf. Sci.*, 116:539, 1982.

[55] Elmers, H. J., J. Hauschild, H. Fritzsche, G. Liu, U. Gradmann U. Kohler. *Phys. Rev. Lett.*, 75:2031, 1995.

[56] Hauschild, J., U. Gradmann H. J. Elmers. *Applied Phys. Lett.*, 72:3211, 1998.

[57] Elmers, H. J., J. Hauschild U. Gradmann. *Phys. Rev. B*, 59:3688, 1999.

[58] Pietzsch, O., A. Kubetzka, M. Bode R. Wisendanger. *Phys. Rev. Lett.*, 84:5212, 2000.

[59] Bevington, P. D.K. Robinson: *Data Reduction and Error Analysis for the Physical Sciences.* McGraw-Hill Inc., 1992.

[60] Lacasse, M. D., J. Vinals M. Grant. *Phys. Rev. B*, 47:5646, 1993.

[61] Wang, J. *Phys. Rev. B*, 47:869, 1993.

[62] Lumsden, M. D., B. D. Gaulin H. Dabrowski. *Phys. Rev. B*, 57:14097, 1998.

[63] Binder, K. D. P. Landau. *Phys. Rev. B*, 13:1140, 1976.

[64] Halperin, B. I. P. C. Hohenberg. *Phys. Rev. Lett.,*, 19:700, 1967.

[65] Halperin, B. I. P. C. Hohenberg. *Phys. Rev.*, 177:952, 1969.

[66] Slivka, J., H. Keller, W. Kundig B. M. Wanklyn. *Phys. Rev. B*, 30:3649, 1984.

[67] KELLER, H. I. M. SAVIC. *Phys. Rev. B*, 28:2638, 1983.

[68] HUTCHINGS, M. T., H. IKEDA E. JANKE. *Phys. Rev. Lett.*, 49:386, 1982.

[69] BOVENSIEPEN, U. ET AL. *JMMM*, 231:65–73, 2001.

[70] RUDT, C. ET AL. *Phys. Rev. B.*, 65:220404(R), 2002.

[71] DUNLAVY, M. J. D. VENUS. *Submitted to Phys. Rev. B, Cond-Mat/0308294*, 2003.

[72] MORI, M. Y. TSUDA. *Phys. Rev. B*, 37:5444, 1988.

[73] LANDAU, L. E. LIFTSHITZ. *Phys. Z. Sojetunion*, 8:153, 1935.

[74] OGIELSKI, A. T. *Phys. Rev. B*, 32:7384, 1985.

[75] BONTEMPS, N., J. RAJCHENBACH, R. V. CHAMBERLIN R. ORBACH. *Phys. Rev. B*, 30:6514, 1984.

[76] GRADMANN, U., M. PRZYBYLSKI, H. J. ELMERS G. LIU. *Applied Phys. A*, 49:563–571, 1989.

[77] ARNOLD, C. S. D. P. PAPPAS. *Phys. Rev. Lett*, 85:5202, 2000.

[78] ELMERS, H. J., J. HAUSCHILD, , H. HOCHE, U. GRADMANN, D. HEUER U. KOHLER. *Phys. Rev. Lett.*, 73:898, 1994.

[79] ET.AL., K. D. CHILDS: *Handbook of Auger Electron Spectroscopy (3rd ed.)*. Physical Electronics Inc., 1995.

[80] HAUSCHILD, J., H. J. ELMERS U. GRADMANN. *Phys. Rev. B*, 57:R677, 1998.

[81] Sander, D., R. Skomski, C. Schmidthals, A. Enders J. Kirschner. *Phys. Rev. Lett.*, 77:2566, 1996.